Comput Mech (2016) 58:549–585
DOI 10.1007/s00466-016-1306-y

Cohesive surface model for fracture based on a two-scale formulation: computational implementation aspects

S. Toro[1,2], P.J. Sánchez[1,2], J.M. Podestá[1], P.J. Blanco[3,4], A.E. Huespe[1,5], R.A. Feijóo[3,4]

[1]CIMEC-UNL-CONICET, Güemes 3450, CP 3000 Santa Fe, Argentina

[2]GIMNI-UTN-FRSF, Lavaise 610, CP 3000 Santa Fe, Argentina

[3]LNCC/MCTI, Av. Getúlio Vargas 333, Petrópolis, RJ, CEP: 25651-075, Brasil

[4]INCT-MACC, Instituto Nacional de Ciência e Tecnologia em Medicina Assistida por Computação Científica, Brasil

[5]Centre Internacional de Metodes Numerics en Enyinyeria (CIMNE),Campus Nord UPC, Edifici C-1, J. Girona 1-3, 08034 Barcelona, Spain

Keywords: multi-scale cohesive models, computational homogenization, heterogeneous material failure, Embedded Finite Elements (EFEM).

Abstract

The paper describes the computational aspects and numerical implementation of a two-scale cohesive surface methodology developed for analyzing fracture in heterogeneous materials with complex microstructures. This approach can be categorized as a semi-concurrent model using the Representative Volume Element (RVE) concept.

A variational multi-scale formulation of the methodology has been previously presented by the authors. Subsequently, the formulation has been generalized and improved in two aspects: *i)* cohesive surfaces have been introduced at both scales of analysis, they are modeled with a strong discontinuity kinematics (new equations describing the insertion of the macro-scale strains, into the micro-scale and the posterior homogenization procedure have been considered); *ii)* the computational procedure and numerical implementation have been adapted for this formulation. The first point has been presented elsewhere, and it is summarized here. Instead, the main objective of this paper is to address a rather detailed presentation of the second point.

Finite element techniques for modeling cohesive surfaces at both scales of analysis (FE^2 approach) are described: *i)* finite elements with embedded strong discontinuities (EFEM) are used for the macro-scale simulation, and *ii)* continuum-type finite elements with high aspect ratios, mimicking cohesive surfaces, are adopted for simulating the failure mechanisms at the micro-scale.

The methodology is validated through numerical simulation of a quasi-brittle concrete fracture problem. The proposed multi-scale model is capable of unveiling the mechanisms that lead from the material degradation phenomenon at the meso-structural level to the activation and propagation of cohesive surfaces at the structural scale.

Comput Mech (2016) 58:549–585
DOI 10.1007/s00466-016-1306-y

1 Introduction

1.1 Literature review

Cohesive Surface Models (CSM) have proven to be a useful conceptual tool for analyzing material fracture. This approach consists in introducing a surface with two interfaces into the continuum. A relative displacement, or displacement jump, is modeled between both interfaces, while cohesive tractions on the same interfaces react by opposing to their opening. As the interfaces are opened, the cohesive forces decrease, tending to zero, which finally yields a new traction-free crack into the continuum. So, the generation of a new traction-free crack demands energy from the mechanical system.

CSM are appropriate to describe the nonlinear dissipative effects observed at small length scales, specifically into the fracture process zone of a propagating crack. The modeling of these effects requires an adequate characterization of the traction-displacement jump law governing the cohesive surface evolution. Implicitly, this characterization also involves the amount of energy demanded to the mechanical system to generate a new traction-free crack into the solid. So, the selection of the traction-displacement jump law turns out to be the foremost issue for modeling cohesive surfaces.

CSM have been firstly introduced in fracture mechanics by Dugdale [1] and Barenblatt [2]. In computational mechanics, they were introduced by Needleman and co-workers (Needleman [3], Xu and Needleman [4], see also references cited in Needleman [5]). After them, CSM have gained a wide acceptance for several reasons. First, its numerical implementation is simple and efficient. But, mainly, CSM has become popular due to the wide range of problems and applications for which they provide useful solutions. Typical examples of CSM applied to dynamics fracture simulations are shown in Falk et al. [6], Xu and Needleman [7] and Pandolfi et al. [8]. In ductile fracture analysis, CSM have been utilized by Hutchinson and Evans [9], Tvergaard [10], Siegmund and Brocks [11], Huespe et al. [12], Huespe et al. [13]. Furthermore, and from the pioneering works of Hillerborg [14], Bažant [15] and Elices et al. [16], CSM models have been widely applied to the field of quasi-brittle materials for modeling concrete fracture problems.

According to the aim of the present work, some features, assumptions and limitations of classical CSM, mainly those related to the traction-separation law description, are summarized and remarked:

i) Usually, for modeling quasi-brittle fracture, the constitutive law relating tractions to displacement jumps across the cohesive surface is proposed independently of the continuum constitutive relation characterizing the bulk material (exceptions to this approach have been proposed in [17], [18] and references cited therein). Two key parameters govern the response of the cohesive forces: the fracture energy and the peak stress. In practical applications, they are estimated from experiments. However, both parameters depend on phenomena occurring at smaller length scales. Typically, a composite could display noticeable differences of the overall fracture energy by changing its micro-structure topology. Topology changes could happen during the loading process, due to material degradation itself. In this case, the experimental determination of parameters governing the traction-separation law, is not free of controversy. So, an alternative approach for assessing the overall fracture energy consists in modeling the material degradation processes at small length scales,

Comput Mech (2016) 58:549–585
DOI 10.1007/s00466-016-1306-y

where the fracture energy of every compound can be accurately characterized, simultaneously with the crack propagation problem at the structural level. Then, by using a specific homogenization technique, the overall fracture energy can be estimated in an unified framework of analysis.

ii) Ductile fracture analysis using CSM has also been widely addressed in the literature. However, in this case, and contrarily to the quasi-brittle fracture approaches, the parameters determining the traction-separation law depend more markedly on the loading path. Typically, separation work in ductile fracture, as well as the peak stress, is enormously influenced by the stress triaxiality (see Tvergaard and Hutchinson [19]). A viable technique to deal with these complex phenomena is the use of multi-scale models, adopting cohesive forces on the interfaces and determining the traction-separation law through a micro-structural analysis. Several works have followed this approach, such as Siegmund and Brocks [11]. However, most of them consider a multi-scale technique where the transference of information between scales flows only in one direction, from the smaller length scale to the larger one (hierarchical model). This kind of hierarchical approach may be questionable when the cohesive forces depend strongly on macro-scale variables that change during the structural loading history.

Within the class of multi-scale procedures for modeling ductile fracture, it is suitable to mention the works of Xia and Shih [20] and Vernerey et al. [21]. In both cases, even when the fracture process zone at the macro-scale is not approached through CSM, the effects induced by the micro-structure during the failure process are taken into account. In the work of Xia and Shih, the micro-structure is explicitly embedded into the macro-model, while, in the work of Vernerey et al., the micro-structure degradation mechanisms are modeled by increasing the kinematical descriptors at the macro-scale using the micromorphic theory framework. Both approaches result highly motivating techniques for developing the model described in this paper.

Determining the overall constitutive relation of micro-structured materials undergoing fracture, via multi-scale procedures, involves meaningful theoretical challenges. In a previous work of the authors, see Sánchez et al. [22], it has been shown that once the macro-scale material response loses the strong ellipticity condition, the conventional homogenization procedure (volume average), evaluated with the use of an RVE, becomes an ill-posed problem, see also Gitman et al. [23] and Nguyen et al. [24]. Contrarily to what happens during the macro-scale stable pre-critical regime, multi-scale problems involving strain localization demand the use of general and original formulations based on non-conventional homogenization paradigms. In last years, this problem has been the motive of intense study. Several authors have contributed with new ideas and theoretical or numerical models. To cite only a few of them, we reference the following works: Belytschko et al. [25], Belytschko and Song [26], Geers et al. [27], Bosco et al. [28], Nguyen et al. [29], Verhoosel et al. [30] Oliver et al. [31], Kulkarni et al. [32] and references cited therein.

1.2 CSM from a novel RVE-based multi-scale framework

Blanco and co-workers [33] have presented a variationally consistent RVE-based unified theory established on the following axioms: (i) kinematic admissibility, (ii) mathematical duality and

Comput Mech (2016) 58:549–585
DOI 10.1007/s00466-016-1306-y

(iii) virtual power principle. They have coined the name Method of Multi-scale Virtual Power (MMVP) for identifying this theory. In the MMVP, the physics between the involved length scales are linked by postulating the so-called Principle of Multi-scale Virtual Power (PMVP), which is a generalization of the Hill-Mandel statement of macro-homogeneity [34, 35]. By using the MMVP, the homogenization formulas for stress-like quantities, the establishment of the precise boundary conditions imposed to the RVE mechanical model and the micro-scale equilibrium problem, are unambiguously derived as consequences of the variational formulation, in contrast with alternative approaches where they are a-priori assumed.

The general framework proposed in [33] encompasses a wide spectrum of multi-scale modeling scenarios, ranging from conventional constitutive-inspired multi-scale theories (see [36, 37, 38, 39]) to more sophisticated and novel approaches, as for example: multi-scale techniques linking high order macro-scale description with standard (first order) micro-scale kinematics [40], thermo-mechanical models (see [41]), multi-scale formulations accounting for inertia and body forces effects (see [42]), etc.

The MMVP can additionally be used as the underlying theory to derive multi-scale models for material failure based on CSM, where the traction-separation law characterizing the macro-scale cohesive interface is obtained by homogenization of micro-scale degradation mechanisms. For example, in Sánchez et al. [22] and Toro et al. [43], a semi-concurrent two-scale approach for material failure analysis has been proposed. The failure phenomena at the micro-scale are represented by the existence of strain localization bands, modeled with a smeared crack technique.

Also, based on the MMVP concept, Toro et al. [44] have subsequently generalized and improved the methodology proposed in [22] and [43] by introducing cohesive surfaces at both scales of analysis. New equations for transferring information between scales (scale-bridging equations) have been developed and presented. As a further development of the two-scale formulation described in Toro et al. [44], a detailed finite element implementation is described in this article to shed light on the following issues: (i) numerical treatment given to CSM at macro and micro scales, including EFEM finite element technique and crack path tracking algorithm, (ii) detailed procedure to evaluate the homogenization formulae for the macro-scale stresses and cohesive tractions, (iii) implementation of the kinematical restrictions on the RVE model, (iv) implementation of the equilibrium problems at both scales of analysis. The computational tool obtained with this procedure results efficient for simulating a wide range of failure phenomena in heterogeneous materials. This subject represents the main contribution of the present work.

The remaining of the paper is structured as follows: in Section 2, we give a brief theoretical description of the methodology formulated in Toro et al. [44]. The main contribution of the present paper is introduced in Section 3, where a detailed description of the finite element models used at both scales, macro and micro, is shown. An embedded strong discontinuity finite element technique (EFEM) is proposed to simulate the cohesive surfaces at the macro-scale. Furthermore, a detailed description of the fracture model at micro-scale is also presented in the same Section. The numerical assessment of the model is presented in Section 4. Sensitivity analysis of the macro-scale response with respect to: *i)* mesoscopic cell size and *ii)* finite element mesh size of a given specific cell, are shown and discussed. Finally, a structural fracture problem is modeled with an heterogeneous quasi-brittle material. Last Section of the paper is devoted to discuss some conclusions.

Comput Mech (2016) 58:549–585
DOI 10.1007/s00466-016-1306-y

2 Description of the multi-scale mechanical formulation

According with the objectives pursued in this contribution, a brief overview of the multi-scale mechanical formulation is shown in this Section, which provides the necessary background for describing the computational implementation in the remaining part of the paper. The full model formulation has been described in Toro et al. [44]. Thus, the readers are addressed to that work for obtaining further details of the formulation, as well as to [33] for consulting specific aspects of the MMVP theory.

Notation used in this work. Objects intervening in the model are identified as follows (see Figure 1):

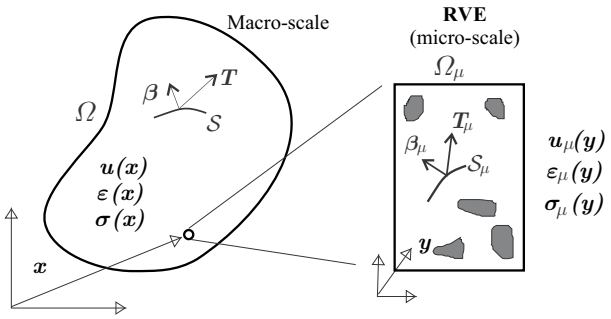

Figure 1: Notation adopted in this work at the macro and micro-scale levels.

i) The domain of the body at the macro-scale is denoted Ω. Points in this domain are identified with $\boldsymbol{x}$. Macro-scale fields, in Ω, are: displacements $\boldsymbol{u}(\boldsymbol{x})$, strains $\boldsymbol{\varepsilon}(\boldsymbol{x})$, stresses $\boldsymbol{\sigma}(\boldsymbol{x})$, and considering the macro-scale cohesive surface $\mathcal{S}$, displacement jump and traction across the interfaces are denoted $\boldsymbol{\beta}$ and $\boldsymbol{T}$, respectively.

ii) Each point $\boldsymbol{x}$ at the macro-scale is linked to an RVE whose domain is denoted Ω_μ. Points in Ω_μ are identified with $\boldsymbol{y}$. Micro-scale fields are distinguished with subscript $(\cdot)_\mu$, and are understood as different objects to those defined at the macro-scale in the previous item, i.e. micro-scale displacements, $\boldsymbol{u}_\mu$, micro-scale strains, $\boldsymbol{\varepsilon}_\mu$, micro-scale stresses, $\boldsymbol{\sigma}_\mu$, displacement jumps across micro-scale cracks $\boldsymbol{\beta}_\mu$, tractions across micro-scale cohesive cracks $\boldsymbol{T}_\mu$, and so on. All micro-scale fields depend on $\boldsymbol{y}$ and $\boldsymbol{x}$.

iii) Each micro-scale kinematic field has a fluctuating component denoted with a tilde: $\tilde{(\cdot)}_\mu$.

iv) The kinematics at both scales are presented in incremental form. Then, infinitesimal increment of variables are identified with the symbol $d(\cdot)$. Kinematically admissible virtual actions are denoted with the symbol $\hat{(\cdot)}$.

The structural loading history changes according to a monotonous increase of the pseudo-time coordinate t. Then, this pseudo-time is adopted as the parameter indicating the sequence of events taking place in the mechanical problem.

Comput Mech (2016) 58:549–585
DOI 10.1007/s00466-016-1306-y

2.1 Macro-scale model with cohesive surfaces

Let us consider the domain Ω of a body displaying an evolving cohesive surface denoted $\mathcal{S}$ whose orthogonal unit vector is $\boldsymbol{n}$, as shown in Figure 2-a. The surface $\mathcal{S}$ shows a relative displacement between both interfaces, also called displacement jump vector, denoted $\boldsymbol{\beta}$, and cohesive tractions $\boldsymbol{T}$ acting on them.

The cohesive surface $\mathcal{S}$ is nucleated at the macro-scale when the material instability condition is detected at a certain pseudo-time instant ($t = t_N$). The criterion defining t_N is presented in sub-Section 3.1.1.

The surface $\mathcal{S}$ divides Ω in two disjoint sets: Ω_+ and Ω_-. On the boundary Γ of Ω, there are imposed tractions $\boldsymbol{t}^e$, on Γ_t, and displacements $\boldsymbol{u}_D$, on Γ_D, being: $\Gamma = \Gamma_t \cup \Gamma_D$, see Figure 2-a. We also consider an arbitrarily small domain $\Omega^\varphi \subset \Omega$ and $\mathcal{S} \subset \Omega^\varphi$. Then, Ω^φ is also divided by $\mathcal{S}$ in two disjoint sets: Ω^φ_+ and Ω^φ_-.

Following to Simo et al. [45], the displacement increment $d\boldsymbol{u}$ at the macro-scale is described by:

$$d\boldsymbol{u} = d\bar{\boldsymbol{u}} + \mathscr{M}\, d\boldsymbol{\beta}, \tag{1}$$

where $d\bar{\boldsymbol{u}}$ represents the increments of the continuous displacement components in Ω. The increment of the displacement jump across $\mathcal{S}$ is $d\boldsymbol{\beta}$ and $\mathscr{M}$ is the unit jump function (with compact support) defined as follows:

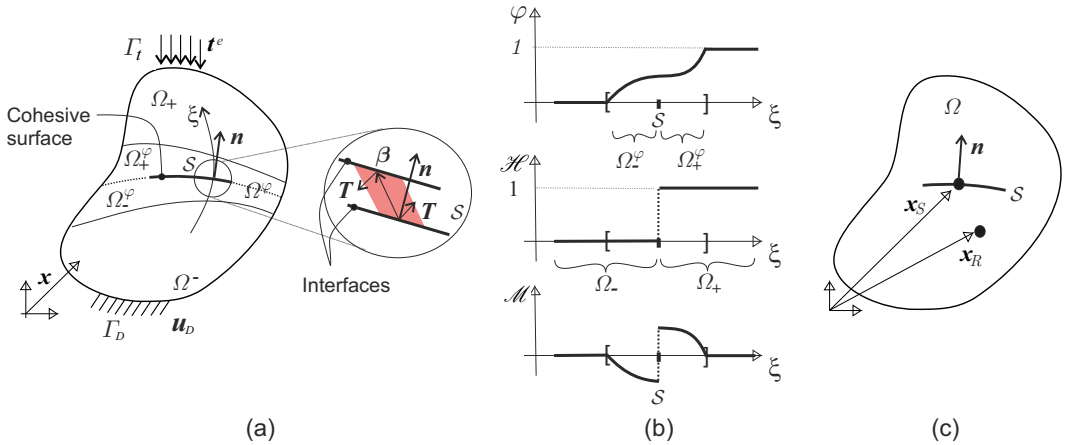

Figure 2: Macro-scale model: (a) cohesive surface at the macro-scale and its mechanical representation; (b) Continuous function φ, Heaviside step function $\mathscr{H}$ and unit jump function $\mathscr{M}$; (c) regular and singular points at the macro-scale.

$$\mathscr{M} := \mathscr{H} - \varphi, \tag{2}$$

$$\mathscr{H} = \begin{cases} 0 & \forall\, \boldsymbol{x} \in \Omega_- \\ 1 & \forall\, \boldsymbol{x} \in \Omega_+ \end{cases}, \quad \varphi = \begin{cases} 0 & \forall\, \boldsymbol{x} \in \Omega_- \backslash \Omega^\varphi_- \\ 1 & \forall\, \boldsymbol{x} \in \Omega_+ \backslash \Omega^\varphi_+ \end{cases}, \tag{3}$$

with $\mathscr{H}$ being the Heaviside step function shifted to $\mathcal{S}$, and φ satisfies (3), but otherwise it is an arbitrary sufficiently smooth function, see Figure 2-b.

Comput Mech (2016) 58:549–585
DOI 10.1007/s00466-016-1306-y

According to equation (1), and following a previous work of the authors [44], it is assumed the existence of a generalized strain increment $d\boldsymbol{\varepsilon}$ in Ω. This strain increment is derived by applying a generalized gradient to the displacement field in equation (1) (see for example [45]). Operating in this way, $d\boldsymbol{\varepsilon}$ is given as follows:

$$d\boldsymbol{\varepsilon} = \underbrace{\nabla_x^s d\bar{\boldsymbol{u}}}_{d\boldsymbol{\varepsilon}_{\bar{u}}} + \underbrace{\mathscr{M}\nabla_x^s d\boldsymbol{\beta} - \nabla_x^s \varphi \otimes^s d\boldsymbol{\beta}}_{d\boldsymbol{\varepsilon}_{\beta}} + \delta_S(d\boldsymbol{\beta} \otimes^s \boldsymbol{n}) = d\boldsymbol{\varepsilon}_{\bar{u}} + d\boldsymbol{\varepsilon}_{\beta} + \delta_S(d\boldsymbol{\beta} \otimes^s \boldsymbol{n}), \tag{4}$$

where it is assumed that $d\boldsymbol{\beta}$ has compact support in Ω^{φ}, the symbol $\otimes^s$ represents the symmetric tensor product, and the Dirac delta function shifted to $\mathcal{S}$ is denoted δ_S (δ_S has units of length^{-1}).

Remark: the last term in (4) introduces a strain singularity in $\mathcal{S}$. Therefore, it is distinguished between: *a)* regular points, denoted $\boldsymbol{x}_R$ ($\boldsymbol{x}_R \in \Omega \backslash \mathcal{S}$), from now on called the bulk material and where strains can be conventionally defined, and *b)* singular points denoted $\boldsymbol{x}_S$ ($\boldsymbol{x}_S \in \mathcal{S}$), as shown in Figure 2-c.

The regular terms in (4) are identified with the strain increment $d\boldsymbol{\varepsilon}_R$ in the bulk material:

$$d\boldsymbol{\varepsilon}_R = d\boldsymbol{\varepsilon}_{\bar{u}}(d\bar{\boldsymbol{u}}) + d\boldsymbol{\varepsilon}_{\beta}(d\boldsymbol{\beta}) \qquad , \qquad \forall\, \boldsymbol{x}_R \in \Omega \backslash \mathcal{S}. \tag{5}$$

The partition of the strain increment $d\boldsymbol{\varepsilon}_R$ in two terms, $d\boldsymbol{\varepsilon}_{\bar{u}}$ and $d\boldsymbol{\varepsilon}_{\beta}$ as shown in equations (4) and (5), evidences the fact that $d\boldsymbol{\varepsilon}_{\bar{u}}$ only depends on $d\bar{\boldsymbol{u}}$, while $d\boldsymbol{\varepsilon}_{\beta}$ only depends on $d\boldsymbol{\beta}$. Note that $d\boldsymbol{\varepsilon}_R$ in the present kinematical description, even though it is defined in regular points, depends on $d\boldsymbol{\beta}$ due to the compact support of the function $\mathscr{M}$, see (2).

From (4), we also identify the singular strain increment quantity $d\boldsymbol{\varepsilon}_S$ in $\mathcal{S}$ as follows:

$$d\boldsymbol{\varepsilon}_S = d\boldsymbol{\varepsilon}_{\bar{u}} + d\boldsymbol{\varepsilon}_{\beta} + \delta_S(d\boldsymbol{\beta} \otimes^s \boldsymbol{n}) \qquad , \qquad \forall\, \boldsymbol{x}_S \in \mathcal{S}. \tag{6}$$

This generalized strain is implicitly represented by the triad of kinematical descriptors $\{d\boldsymbol{\varepsilon}_{\bar{u}}, d\boldsymbol{\varepsilon}_{\beta}, d\boldsymbol{\beta}\}$. From now on, we describe $d\boldsymbol{\varepsilon}_S$ by this implicit representation.

The balance momentum equation in Ω can be written in a variational format as follows: find $(\bar{\boldsymbol{u}}, \boldsymbol{\beta}) \in \mathscr{U}$ such that:

$$\int_{\Omega\backslash\mathcal{S}} \boldsymbol{\sigma} \cdot \hat{\boldsymbol{\varepsilon}}_R \, d\Omega + \int_{\mathcal{S}} \boldsymbol{T} \cdot \hat{\boldsymbol{\beta}} \, d\mathcal{S} \; - \int_{\Gamma_t} \boldsymbol{t}^e \cdot \hat{\bar{\boldsymbol{u}}} \, d\Gamma = 0 \quad ; \quad \forall\, (\hat{\bar{\boldsymbol{u}}}, \hat{\boldsymbol{\beta}}) \in \mathscr{V}, \tag{7}$$

where $\mathscr{U}$ is the set of kinematically admissible descriptors and $\mathscr{V}$ the space of kinematically admissible virtual actions given as follows:

$$\begin{aligned} \mathscr{U} &:= \left\{ (\bar{\boldsymbol{u}}, \boldsymbol{\beta}) \; ; \; \bar{\boldsymbol{u}} \in \boldsymbol{H}^1(\Omega) \; , \; \boldsymbol{\beta} \in \boldsymbol{H}^1(\Omega^{\varphi}) \text{ and } \bar{\boldsymbol{u}}|_{\Gamma_D} = \boldsymbol{u}_D \right\}, \\ \mathscr{V} &:= \left\{ (\hat{\bar{\boldsymbol{u}}}, \hat{\boldsymbol{\beta}}) \; ; \; \hat{\bar{\boldsymbol{u}}} \in \boldsymbol{H}^1(\Omega) \; , \; \hat{\boldsymbol{\beta}} \in \boldsymbol{H}^1(\Omega^{\varphi}) \text{ and } \hat{\bar{\boldsymbol{u}}}|_{\Gamma_D} = \boldsymbol{0} \right\}. \end{aligned} \tag{8}$$

Comput Mech (2016) 58:549–585
DOI 10.1007/s00466-016-1306-y

2.1.1 Multi-scale evaluation of stresses and tractions

In equation (7), stresses $\boldsymbol{\sigma}$ at regular points, $\boldsymbol{x}_R$, and tractions $\boldsymbol{T}$ at singular points, $\boldsymbol{x}_S$, are evaluated using specific non-standard homogenization procedures gathering information from the micro-scale. These homogenization procedures are rationally justified within the framework of the MMVP theory ([33] and [44]). Each of them is typified as follows:

i) MMRp (Multi-scale constitutive Model at Regular points): this homogenization procedure defines the overall bulk material response, $\boldsymbol{\sigma}$, at $\boldsymbol{x}_R$;

ii) MMSp (Multi-scale constitutive Model at Singular points): this homogenization procedure defines the overall traction-separation response, $\boldsymbol{T}$,at $\boldsymbol{x}_S$.

Figure 3 sketches the big picture of the homogenization procedure in Ω, identifying the MMRp and MMSp procedures and the macro-scale points where each of them is utilized. Every macro-scale point has its own RVE. Incremental strains and generalized incremental strains are inserted from the macro-scale to the micro-scale, while stresses and tractions are obtained from the micro-scale, by applying homogenization techniques. The process of inserting strains and retrieving generalized stresses is governed by a set of scale bridging equations which are defined and described in detail in sub-Section 2.3.

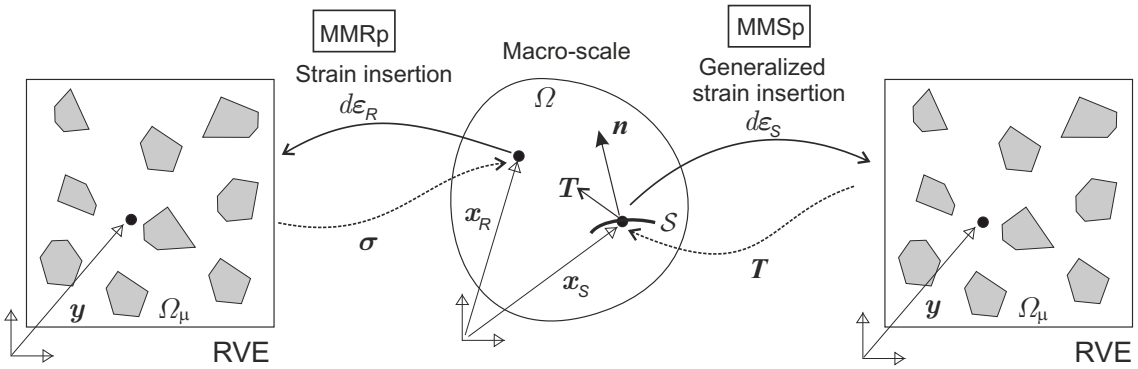

Figure 3: Multi-scale model for fracture: (a) the MMRp homogenization procedure evaluates the overall material response, $\boldsymbol{\sigma}$, at regular points $\boldsymbol{x}_R$; (b) the MMSp homogenization procedure evaluates the overall material response, $\boldsymbol{T}$, on the cohesive surface, at points $\boldsymbol{x}_S$.

2.2 Micro-scale model with cohesive surfaces

The kinematical description at the RVE is similar to that utilized at the macro-scale. So, the failure mechanism is described by means of cohesive surfaces which are nucleated as the structural loading increases.

Let us consider the RVE domain Ω_μ displaying n_c cohesive surfaces nucleated at the micro-scale during the loading process. The i-th cohesive surface is denoted $\mathcal{S}_\mu^i$, and its normal vector is $\boldsymbol{n}_\mu^i$, see Figure 4-a. The cohesive surface $\mathcal{S}_\mu^i$ divides Ω_μ in two disjoint domains, $\Omega_{\mu_+}^i$ and $\Omega_{\mu_-}^i$, with $\boldsymbol{n}_\mu^i$ pointing toward Ω_{μ_+}.

Comput Mech (2016) 58:549–585
DOI 10.1007/s00466-016-1306-y

A micro-scale cohesive crack $\mathcal{S}_\mu^i$ nucleates when the material bifurcation condition is satisfied at a given point of the micro-scale, and previously to reaching the critical condition at the macro-scale for crack nucleation at pseudo-time t_{N_μ}.

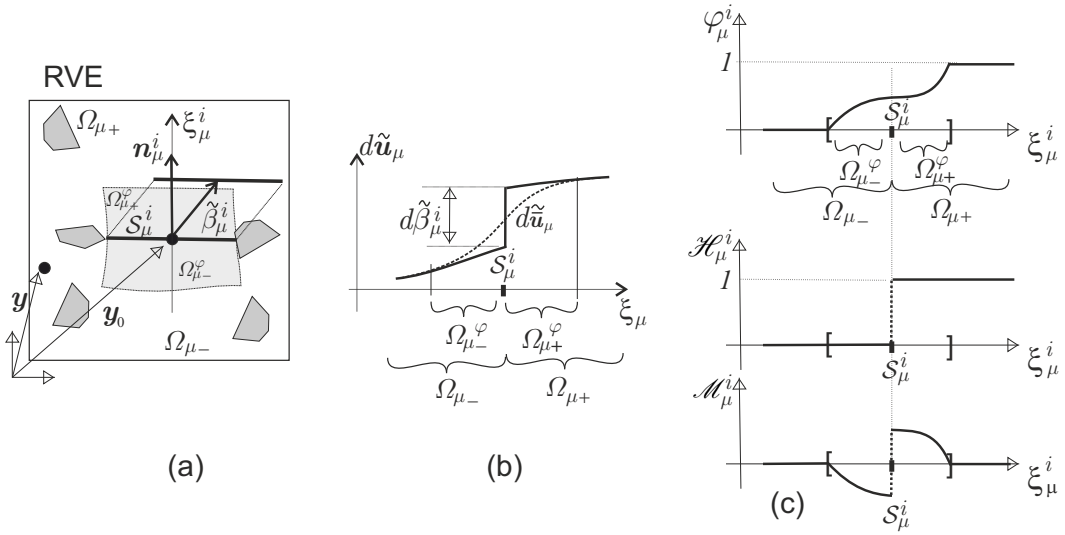

Figure 4: Kinematics at the micro-scale accounting for material failure. (a) cohesive surface $\mathcal{S}_\mu^i$; (b) micro-scale displacement fluctuation increment field, $d\tilde{\boldsymbol{u}}_\mu$ displaying a strong discontinuity across $\mathcal{S}_\mu^i$; (c) continuous function φ_μ^i, Heaviside function $\mathscr{H}_\mu^i$ and unit jump function $\mathscr{M}_\mu^i$.

The micro-scale strain increment $d\boldsymbol{\varepsilon}_\mu$ in Ω_μ is:

$$d\boldsymbol{\varepsilon}_\mu = \mathcal{I}(d\boldsymbol{\varepsilon}) + d\tilde{\boldsymbol{\varepsilon}}_\mu, \tag{9}$$

where the first term corresponds to the macro-scale strain increment, $d\boldsymbol{\varepsilon}$, injected from $\boldsymbol{x}$ into Ω_μ, through the insertion operator $\mathcal{I}(\cdot)$. The insertion operator $\mathcal{I}(\cdot)$ distributes its argument into the RVE domain. Both, $\mathcal{I}$ as well as its argument, changes according with the homogenization procedure. The operator $\mathcal{I}$ is defined in next sub-Section 2.3 where it is labeled $\mathcal{I}_R$ or $\mathcal{I}_S$ according to the MMRs or MMSp procedure, respectively.

The last term on the right hand side of (9) is the micro-scale strain fluctuation increment defined as:

$$d\tilde{\boldsymbol{\varepsilon}}_\mu = \nabla_y^s d\tilde{\boldsymbol{u}}_\mu, \tag{10}$$

where $d\tilde{\boldsymbol{u}}_\mu$ is the micro-scale displacement fluctuation increment, whose description is discussed in the following.

2.2.1 Treatment given to the micro-scale displacement fluctuation increment field

Similar to the strong discontinuity kinematics adopted at the macro-scale, described by equation (1), the micro-scale displacement fluctuation increment, $d\tilde{\boldsymbol{u}}_\mu$, is written as the addition of two terms, see Figure 4-b:

Comput Mech (2016) 58:549–585
DOI 10.1007/s00466-016-1306-y

$$d\tilde{\boldsymbol{u}}_\mu = d\tilde{\tilde{\boldsymbol{u}}}_\mu + \sum_{i=1}^{n_c} \mathscr{M}_\mu^i \, d\tilde{\boldsymbol{\beta}}_\mu^i \,, \tag{11}$$

where $\tilde{\tilde{\boldsymbol{u}}}_\mu$ is the continuous component of the micro-scale displacement fluctuation, $\tilde{\boldsymbol{\beta}}_\mu^i$ is the displacement jump fluctuation across the interfaces of the i-th cohesive surface $\mathcal{S}_\mu^i$ and $\mathscr{M}_\mu^i$ is the unit jump function. Both, $\tilde{\boldsymbol{\beta}}_\mu^i$ and $\mathscr{M}_\mu^i$, are related to $\mathcal{S}_\mu^i$. In (11), we assume that the field $d\tilde{\boldsymbol{u}}_\mu$ results from the addition of all the contributions of the n_c cohesive surfaces which have nucleated during the loading history. The function $\mathscr{M}_\mu^i$ is defined as follows, see Figure 4-c:

$$\mathscr{M}_\mu^i := \mathscr{H}_\mu^i - \varphi_\mu^i \,, \tag{12}$$

$$\mathscr{H}_\mu^i = \begin{cases} 0 & \forall\, \boldsymbol{y} \in \Omega_{\mu-}^i \\ 1 & \forall\, \boldsymbol{y} \in \Omega_{\mu+}^i \end{cases} \quad , \quad \varphi_\mu^i = \begin{cases} 0 & \forall\, \boldsymbol{y} \in \Omega_{\mu-}^i \backslash \Omega_\mu^{i\varphi}{}_- \\ 1 & \forall\, \boldsymbol{y} \in \Omega_{\mu+}^i \backslash \Omega_\mu^{i\varphi}{}_+ \end{cases} , \tag{13}$$

where the Heaviside step function $\mathscr{H}_\mu^i$ and the smooth function φ_μ^i are also related to the same i-th cohesive crack. In this case, $\Omega_\mu^{i\varphi}$ is a small domain around $\mathcal{S}_\mu^i$ (with: $\mathcal{S}_\mu^i \subset \Omega_\mu^{i\varphi} \subset \Omega_\mu$), while $\Omega_\mu^{i\varphi}{}_+$ and $\Omega_\mu^{i\varphi}{}_-$ are subdomains of $\Omega_\mu^{i\varphi}$ partitioned by $\mathcal{S}_\mu^i$, as shown in Figure 4-a.

According with (11), the micro-scale strain fluctuation increment, $d\tilde{\boldsymbol{\varepsilon}}_\mu$, is given by:

$$d\tilde{\boldsymbol{\varepsilon}}_\mu = d\tilde{\boldsymbol{\varepsilon}}_{\mu R} + \sum_{i=1}^{n_c} \delta_{\mathcal{S}_\mu^i} (d\tilde{\boldsymbol{\beta}}_\mu^i \otimes^s \boldsymbol{n}_\mu^i) \qquad , \qquad \forall \boldsymbol{y} \in \Omega_\mu \,, \tag{14}$$

where the first (regular) term on the right hand side is:

$$d\tilde{\boldsymbol{\varepsilon}}_{\mu R} = \nabla_y^s d\tilde{\tilde{\boldsymbol{u}}}_\mu + \sum_{i=1}^{n_c} \left(\mathscr{M}_\mu^i \nabla_y^s d\tilde{\boldsymbol{\beta}}_\mu^i - \nabla_y^s \varphi_\mu^i \otimes^s d\tilde{\boldsymbol{\beta}}_\mu^i \right) , \tag{15}$$

and the second (singular) term is defined by the Dirac delta function $\delta_{\mathcal{S}_\mu^i}$ shifted to $\mathcal{S}_\mu^i$.

2.3 Scale-bridging equations

In the present sub-Section, the scale bridging equations of the multi-scale model presented in [44] are summarized. The readers are addressed to that reference to find the full description of the concepts supporting these equations.

The scale bridging equations are established from the following two axioms and the consequences derived from them, see further details in [33]:

H1) Kinematical admissibility requirements connecting the kinematics at macro and micro-scales. This hypothesis imposes the following constraints on the micro-scale strains:

$$\int_{\Omega_\mu^*} d\boldsymbol{\varepsilon}_\mu \, d\Omega_\mu = \int_{\Omega_\mu^*} \mathcal{I}(d\boldsymbol{\varepsilon}) \, d\Omega_\mu \,. \tag{16}$$

The insertion operator $\mathcal{I}$, its arguments and the micro-scale domain Ω_μ^* where identity (16) is imposed, depend on the homogenization procedure, MMRp or MMSp (see equations (18), (29) and (30) in the following paragraphs).

Comput Mech (2016) 58:549–585
DOI 10.1007/s00466-016-1306-y

From equation (9), condition (16) enforces a null average of the micro-scale strain fluctuation, $d\tilde{\boldsymbol{\varepsilon}}_\mu$, in Ω^*_μ. This kinematical admissibility requirement is conventional in semi-concurrent multi-scale models using a RVE (where $\Omega^*_\mu \equiv \Omega_\mu$, and $\mathcal{I}(d\boldsymbol{\varepsilon})$ is the identity operator). However, it has been generalized in [44] in order to develop a consistent homogenization model for the singular points $\boldsymbol{x}_S$.

H2) Identity, in a variational sense, of internal virtual power densities between both scales. This hypothesis is the Principle of Multi-scale Virtual Power, according with [33], and is a generalized version of the Hill-Mandel Principle. Hypothesis (H2) has been specified in [44] to include the presence of strong discontinuities at both scales of analysis.

As mentioned above, at the macro-scale level, the multi-scale model distinguishes between regular points, $\boldsymbol{x}_R$, and singular points, $\boldsymbol{x}_S$. Different strain insertion procedures are defined in those points (MMRp and MMSp). Then, hypotheses H1 and H2 should be specified in each case.

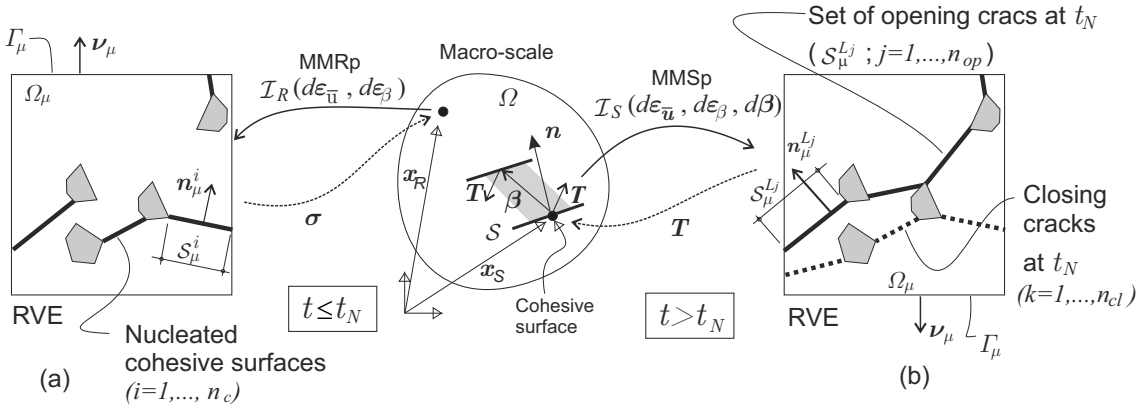

Figure 5: Overview of the multi-scale model for fracture: (a) the MMRp homogenization procedure uses the insertion operator $\mathcal{I}_R$ which is defined in Box 1; (b) the MMSp homogenization procedure uses the insertion operator $\mathcal{I}_S$ which is defined in Box 2.

As a realistic assumption for modeling multi-scale material failure problems, it is considered that during the macro-scale pre-bifurcation regime at a given point $\boldsymbol{x}_R$, there have been nucleated n_c micro-scale cohesive cracks in Ω_μ. These micro-cracks are denoted $\mathcal{S}^i_\mu$ (with $i = 1, ..., n_c$). The number n_c changes in the loading history because new cohesive cracks may sequentially nucleate during $t < t_N$.

However, when bifurcation at the macro-scale is detected, at $t = t_N$, from the n_c nucleated micro-scale cohesive cracks in Ω_μ, n_{op} cracks are opening and n_{cl} are closing or remain inactive ($n_c = n_{cl} + n_{op}$). $\mathcal{S}^{L_j}_\mu$ (with $j = 1, ..., n_{op}$) denotes the j-th opening crack, and $\mathcal{S}^L_\mu$ is the set of all the opening cracks ($\mathcal{S}^L_\mu = \cup_{i=1}^{n_{op}} \mathcal{S}^i_\mu$). There are not new surfaces which can nucleate or re-open during the subsequent loading history. So, the failure mode is defined by the set of the n_{op} opening surfaces at $t = t_N$, and after that, it does not change anymore.

In order to apply the scale transition equations of the MMSp homogenization procedure, the domain $\mathcal{S}^L_\mu$ has to be precisely detected at $t = t_N$. The algorithm to define $\mathcal{S}^L_\mu$ is described in the numerical implementation Section.

Comput Mech (2016) 58:549–585
DOI 10.1007/s00466-016-1306-y

Taking into account the previous concepts, it is defined a tortuosity factor θ, as follows:

$$\theta(\boldsymbol{x}_S) = \frac{|\mathcal{S}_\mu^L|}{\Big\| \Big(\sum_{j=1}^{n_{op}} \int_{\mathcal{S}_\mu^{L_j}} \boldsymbol{n}_\mu^{L_j} \, d\mathcal{S}_\mu \Big) \Big\|} \quad , \quad |\mathcal{S}_\mu^L| = \sum_{j=1}^{n_{op}} |\mathcal{S}_\mu^{L_j}| \ , \tag{17}$$

where $|\mathcal{S}_\mu^{L_j}|$ is the measure of the cohesive surface $\mathcal{S}_\mu^{L_j}$.

The parameter $\theta \in [1, \infty)$ is interpreted as a geometrical factor measuring the tortuosity of the micro-scale crack path of the failure mechanism at the RVE, at $t = t_N$. It is introduced to guarantee the kinematical consistency associated with the cracks opening at both scales of analysis: the opening of the macro-crack $\mathcal{S}$ and the openings, in several directions, of the multiple cracks simulated at the micro scale level. Note that $\theta = 1$ if all the micro-scale cracks are parallel, and it is larger than 1 if the micro-scale cracks follow a zig-zag path. A sensitivity analysis of the macro-scale behavior with respect to θ has been presented in a previous work of the authors, see Toro et al. [44]. In such contribution, a rigorous kinematical justification for including the θ-factor in the multi-scale model has also been discussed.

The tortuosity parameter θ scales all terms involving the macro-scale displacement jump $\boldsymbol{\beta}$ intervening in the scale transition procedure (see [44] for a purely kinematical justification of (17)).

The scale bridging equations governing the multi-scale problem are summarized in Boxes 1 and 2. However, before discussing these equations, in Figure 6 we sketch, by means of three blocks, the sequence of macro-scale kinematical, constitutive and variational equilibrium equations that govern a mechanical problem within the framework of the present multi-scale approach. These three blocks are contained into a larger box identified as "Macro-scale Mechanical Problem", that represents the iterative strategy (for example the Newton-Raphson scheme), for solving the mechanical problem. This Figure also describes the information flow across the three blocks and the corresponding equations which characterize each block. Specifically, the block representing the macro-scale constitutive model is divided in two sub-blocks according if the constitutive model refers to a regular ($\boldsymbol{x}_R$) or a singular ($\boldsymbol{x}_\mathcal{S}$) point, and therefore to the MMRp or MMSp homogenization procedure. The RVE problems of both homogenization procedures are sketched in detail in Figure 7, which follows a similar organization used in Figure 6.

The equations summarized in Boxes 1 and 2 are related to the sub-block "Macro-Scale Constitutive Models" in Figure 6. They are explained in the next two items:

i) **MMRp homogenization procedure to obtain $\boldsymbol{\sigma}$ in $\boldsymbol{x}_R$** (see Box 1).

The regular macro-scale strain increment, $d\boldsymbol{\varepsilon}_R$, is the data input of the multi-scale constitutive relation described in Box 1. According to equation (5), $d\boldsymbol{\varepsilon}_R$ is given by the addition of two components: $d\boldsymbol{\varepsilon}_{\bar{u}}$ and $d\boldsymbol{\varepsilon}_\beta$.

The first block of equations (20)–(26) in Box 1, defines the micro-scale kinematics in Ω_μ and the functional spaces involved in the variational formulation of the micro-scale problem.

The strain increment $d\boldsymbol{\varepsilon}_\mu$, at the RVE, is given by equations (20)–(22) and is a particularization of (9). The strain increment $d\boldsymbol{\varepsilon}_\mu$ results from the addition of two terms: the macro-scale strain increment $d\boldsymbol{\varepsilon}_R$, inserted from the macro-scale into the RVE through the

Comput Mech (2016) 58:549–585
DOI 10.1007/s00466-016-1306-y

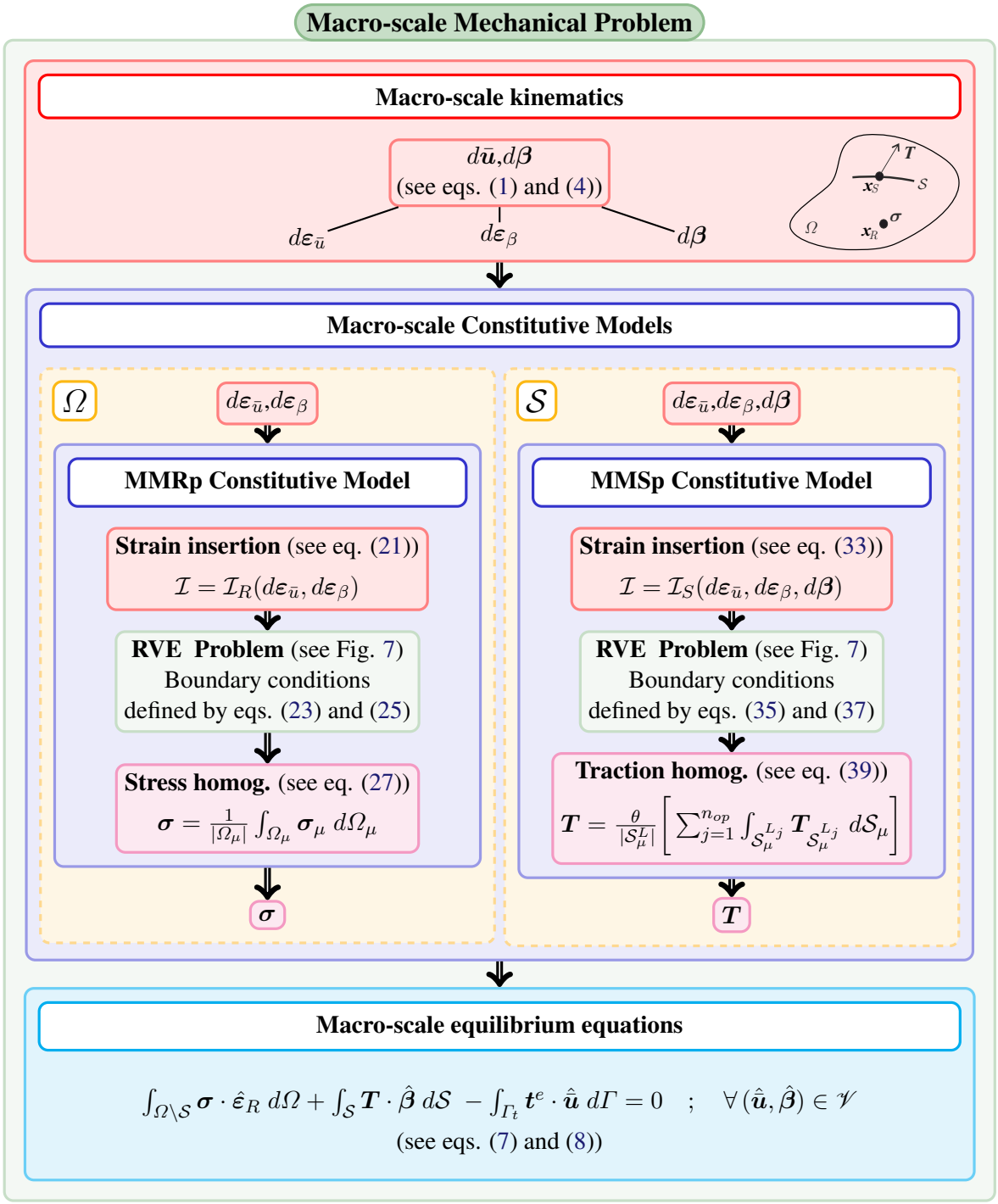

Figure 6: Data flow of the mechanical problem involving both scales of analysis: macro and micro.

Comput Mech (2016) 58:549–585
DOI 10.1007/s00466-016-1306-y

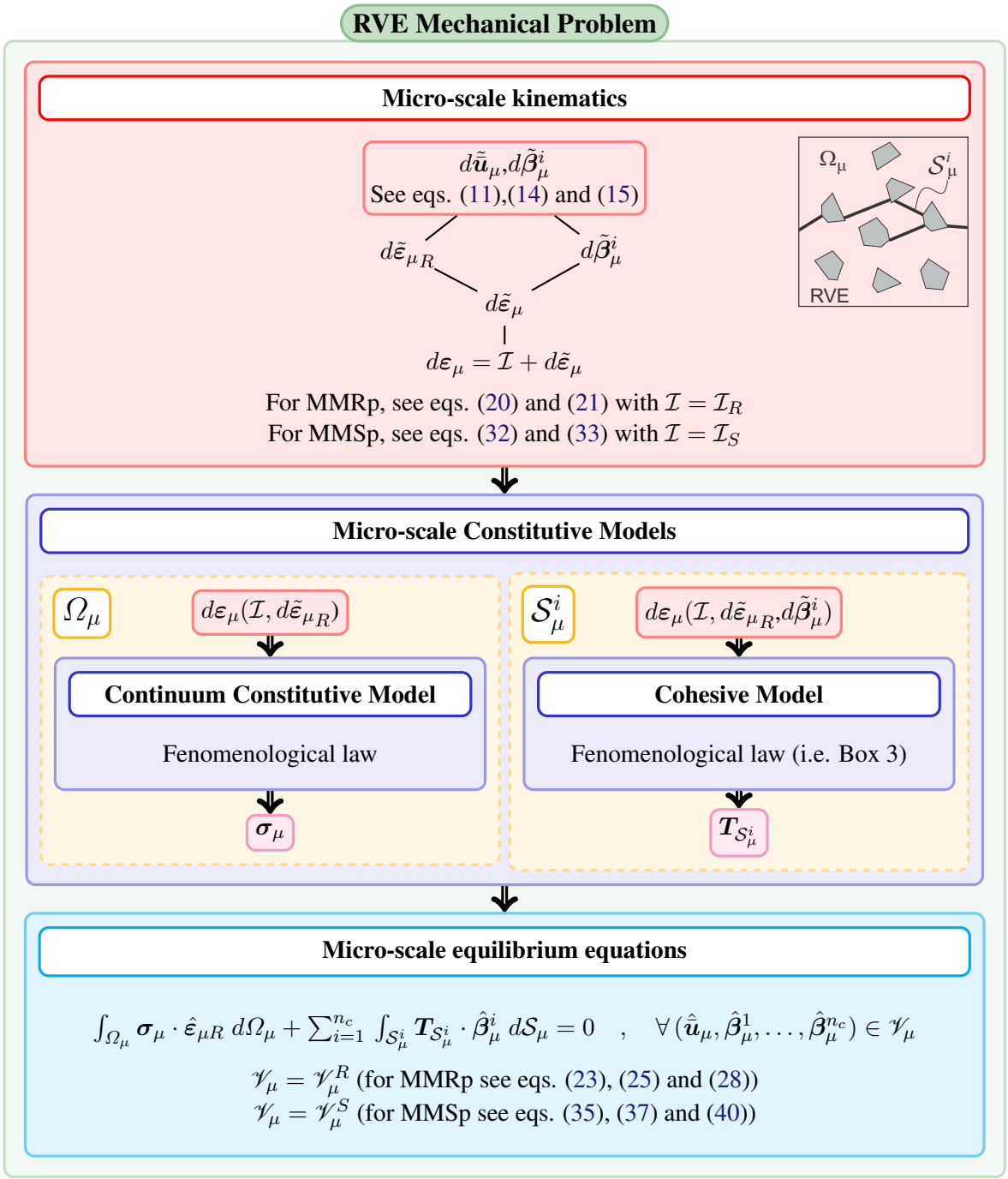

Figure 7: Data flow of the RVE problem for both homogenization procedures: MMRp and MMSp.

Comput Mech (2016) 58:549–585
DOI 10.1007/s00466-016-1306-y

operator $\mathcal{I}_R(\cdot)$, plus the strain fluctuation increments $d\tilde{\boldsymbol{\varepsilon}}_\mu$. According with the definition of the operator $\mathcal{I}_R(\cdot)$, in equation (21), both terms $d\boldsymbol{\varepsilon}_{\bar{u}}$ and $d\boldsymbol{\varepsilon}_\beta$ are uniformly distributed into Ω_μ. However, note that $d\boldsymbol{\varepsilon}_\beta$ is scaled by the tortuosity factor θ.

The Kinematical admissibility requirement (16), hypothesis H1, is particularized as follows:

$$\int_{\Omega_\mu} d\boldsymbol{\varepsilon}_\mu \, d\Omega_\mu = \int_{\Omega_\mu} \mathcal{I}_R(d\boldsymbol{\varepsilon}_{\bar{u}}, d\boldsymbol{\varepsilon}_\beta) \, d\Omega_\mu \ , \tag{18}$$

see [44] for additional details. Then, expression (23) of block 1 defines the space of kinematically admissible displacement fluctuations $\tilde{\mathscr{U}}_\mu^R$. As mentioned above, the kinematical descriptors fully defining the displacement fluctuations at the micro-scale are: $d\tilde{\boldsymbol{u}}_\mu$ and $d\tilde{\boldsymbol{\beta}}_\mu^i$ ($i = 1, ..., n_c$). They are assumed to be independent descriptors. Geometrical entities in expression (23), i.e. the boundary Γ_μ of Ω_μ and its unit normal vector $\boldsymbol{\nu}_\mu$, are depicted in Figure 5. The integral restriction on the boundary Γ_μ imposed to the displacement fluctuation increment fields in $\tilde{\mathscr{U}}_\mu^R$, as expressed in (23), is equivalent to restriction (18).

Expression (24) defines the virtual actions at the macro-scale. Note that in the MMRp model we consider that $\hat{\boldsymbol{\varepsilon}}_{\bar{u}}$ is an arbitrary tensor while $\hat{\boldsymbol{\beta}} \equiv \boldsymbol{0}$. The corresponding space of virtual displacement actions at the micro-scale is $\mathscr{V}_\mu^R$, and the micro-scale virtual strain actions are defined in expression (26).

Any subspace of $\tilde{\mathscr{U}}_\mu^R$ and $\mathscr{V}_\mu^R$, is also kinematically admissible and defines alternative (more constrained) sub-models of the MMRp procedure.

The specific definition of the virtual actions is the basis to postulate the Principle of Multi-scale Virtual Power (H2), which is expressed as follows:

$$\begin{aligned} \boldsymbol{\sigma} \cdot \hat{\boldsymbol{\varepsilon}}_{\bar{u}} = \frac{1}{|\Omega_\mu|} \int_{\Omega_\mu} \boldsymbol{\sigma}_\mu \cdot \hat{\boldsymbol{\varepsilon}}_\mu(\hat{\boldsymbol{\varepsilon}}_{\bar{u}}, \hat{\tilde{\boldsymbol{u}}}_\mu, \hat{\boldsymbol{\beta}}_\mu^1, ..., \hat{\boldsymbol{\beta}}_\mu^{n_c}) \, d\Omega_\mu \quad , \\ \forall \, \hat{\boldsymbol{\varepsilon}}_{\bar{u}} \ \text{ and } \ \forall \, (\hat{\tilde{\boldsymbol{u}}}, \hat{\boldsymbol{\beta}}_\mu^1, ..., \hat{\boldsymbol{\beta}}_\mu^{n_c}) \in \mathscr{V}_\mu^R. \end{aligned} \tag{19}$$

The left hand side of this equation is the macro-scale internal virtual power density and the right hand side is the average internal virtual power in Ω_μ. Equation (19) emphasizes the dependence of the micro-scale strain variations $\hat{\boldsymbol{\varepsilon}}_\mu$ with: $\hat{\boldsymbol{\varepsilon}}_{\bar{u}}, \hat{\tilde{\boldsymbol{u}}}_\mu, \hat{\boldsymbol{\beta}}_\mu^1, ..., \hat{\boldsymbol{\beta}}_\mu^{n_c}$. This dependence is explicitly shown in equations (26).

After replacing (24) and (26) into (19), the Principle of Multi-scale Virtual Power (H2) implies two natural consequences in the sense of the associated Euler-Lagrange equations. They are derived by considering independent variations of $\hat{\boldsymbol{\varepsilon}}_{\bar{u}}$ and $(\hat{\tilde{\boldsymbol{u}}}, \hat{\boldsymbol{\beta}}_\mu^1, ..., \hat{\boldsymbol{\beta}}_\mu^{n_c})$. Both consequences are presented in blocks 2.a and 2.b of Box 1, and are explained as follows:

(2.a) Equation (27) is derived from (19) by allowing arbitrary variations $\hat{\boldsymbol{\varepsilon}}_{\bar{u}}$ and holding $(\hat{\tilde{\boldsymbol{u}}}, \hat{\boldsymbol{\beta}}_\mu^1, ..., \hat{\boldsymbol{\beta}}_\mu^{n_c})$ fixed to zero. This equation defines the homogenization procedure determining the macro-scale stresses $\boldsymbol{\sigma}$, as the volumetric averaging of the micro-scale stress field $\boldsymbol{\sigma}_\mu$. The micro-scale stress $\boldsymbol{\sigma}_\mu$ is determined from the micro-scale equilibrium problem given by expression (28).

Comput Mech (2016) 58:549–585
DOI 10.1007/s00466-016-1306-y

(2.b) Expression (28) is derived from (19) by introducing arbitrary variations of $(\hat{\tilde{\boldsymbol{u}}}, \hat{\boldsymbol{\beta}}^1_\mu, ..., \hat{\boldsymbol{\beta}}^{n_c}_\mu)$ and holding $\hat{\boldsymbol{\varepsilon}}_{\bar{u}}$ fixed to zero. This equation is the variational equilibrium equation in Ω_μ.

The constitutive relation of every constituent of the heterogeneous material and the traction-separation law of every cohesive surface in Ω_μ must be specified to solve the micro-scale equilibrium problem (28), and so, to determine $\boldsymbol{\sigma}_\mu$ and $\boldsymbol{T}_{\mathcal{S}^i_\mu}$.

Box 1: Multi-scale constitutive Model at Regular points (MMRp)

Given the strain history: $\boldsymbol{\varepsilon}_R^{(t-dt)}$ and $\{d\boldsymbol{\varepsilon}_{\bar{u}},\ d\boldsymbol{\varepsilon}_\beta\}$, find $\boldsymbol{\sigma}$ satisfying :

1- ***Kinematics:***

$$d\boldsymbol{\varepsilon}_\mu = \mathcal{I}_R(d\boldsymbol{\varepsilon}_{\bar{u}}, d\boldsymbol{\varepsilon}_\beta) + d\tilde{\boldsymbol{\varepsilon}}_\mu \quad , \quad \forall\, \boldsymbol{y} \in \Omega_\mu \tag{20}$$

$$\mathcal{I}_R(d\boldsymbol{\varepsilon}_{\bar{u}}, d\boldsymbol{\varepsilon}_{\boldsymbol{\beta}}) = d\boldsymbol{\varepsilon}_{\bar{u}} + \theta d\boldsymbol{\varepsilon}_\beta \tag{21}$$

$$d\tilde{\boldsymbol{\varepsilon}}_\mu = \nabla^s_y d\tilde{\tilde{\boldsymbol{u}}}_\mu + \sum_{i=1}^{n_c} \left(\mathscr{M}^i_\mu \nabla^s_y d\tilde{\boldsymbol{\beta}}^i_\mu - \nabla_y \varphi^i_\mu \otimes^s d\tilde{\boldsymbol{\beta}}^i_\mu + \delta_{\mathcal{S}^i_\mu} (d\tilde{\boldsymbol{\beta}}^i_\mu \otimes^s \boldsymbol{n}^i_\mu) \right) \tag{22}$$

Kinematically admissible space of incremental displacement fluctuations, $d\tilde{\boldsymbol{u}}_\mu$***:***

$$\tilde{\mathscr{U}}^R_\mu = \left\{ (d\tilde{\boldsymbol{u}}_\mu, d\tilde{\boldsymbol{\beta}}^1_\mu, \ldots, d\tilde{\boldsymbol{\beta}}^{n_c}_\mu) \text{ suff. regular, such that: } \int_{\Gamma_\mu} d\tilde{\tilde{\boldsymbol{u}}}_\mu \otimes^s \boldsymbol{\nu}_\mu \, d\Gamma_\mu = \boldsymbol{0} \right\} \tag{23}$$

Virtual kinematically admissible actions:

Virtual actions at the macro-scale:

$$\hat{\boldsymbol{\beta}} = \boldsymbol{0} \quad , \quad \hat{\boldsymbol{\varepsilon}}_{\bar{u}} \text{ arbitrary} \tag{24}$$

Virtual actions at the micro-scale:

$$(\hat{\tilde{\boldsymbol{u}}}_\mu, \hat{\boldsymbol{\beta}}^1_\mu, \ldots, \hat{\boldsymbol{\beta}}^{n_c}_\mu) \in \mathscr{V}^R_\mu \quad , \quad \text{with:} \quad \mathscr{V}^R_\mu \equiv \tilde{\mathscr{U}}^R_\mu \tag{25}$$

$$\hat{\boldsymbol{\varepsilon}}_\mu = \mathcal{I}_R(\hat{\boldsymbol{\varepsilon}}_{\bar{u}}, \boldsymbol{0}) + \nabla^s_y \hat{\tilde{\boldsymbol{u}}}_\mu + \sum_{i=1}^{n_c} \left(\mathscr{M}^i_\mu \nabla^s_y \hat{\boldsymbol{\beta}}^i_\mu - \nabla_y \varphi^i_\mu \otimes^s \hat{\boldsymbol{\beta}}^i_\mu + \delta_{\mathcal{S}^i_\mu} (\hat{\boldsymbol{\beta}}^i_\mu \otimes^s \boldsymbol{n}^i_\mu) \right) \tag{26}$$

2- ***Consequences derived from the Principle of Multi-scale Virtual Power***

2.a ***Stress Homogenization:***

$$\boldsymbol{\sigma} = \frac{1}{|\Omega_\mu|} \int_{\Omega_\mu} \boldsymbol{\sigma}_\mu \, d\Omega_\mu \tag{27}$$

2.b ***Micro-scale Equilibrium problem:***

Given the strain history $\boldsymbol{\varepsilon}_R^{(t-dt)}$ and $\{d\boldsymbol{\varepsilon}_R\}$, find $(d\tilde{\tilde{\boldsymbol{u}}}_\mu, d\tilde{\boldsymbol{\beta}}^1_\mu, \ldots, d\tilde{\boldsymbol{\beta}}^{n_c}_\mu) \in \tilde{\mathscr{U}}^R_\mu$ such that:

$$\int_{\Omega_\mu} \boldsymbol{\sigma}_\mu \cdot \hat{\boldsymbol{\varepsilon}}_{\mu R} \, d\Omega_\mu + \sum_{i=1}^{n_c} \int_{\mathcal{S}^i_\mu} \boldsymbol{T}_{\mathcal{S}^i_\mu} \cdot \hat{\boldsymbol{\beta}}^i_\mu \, d\mathcal{S}_\mu = 0 \quad , \quad \forall\, (\hat{\tilde{\boldsymbol{u}}}_\mu, \hat{\boldsymbol{\beta}}^1_\mu, \ldots, \hat{\boldsymbol{\beta}}^{n_c}_\mu) \in \mathscr{V}^R_\mu \tag{28}$$

ii) **MMSp homogenization procedure to obtain $\boldsymbol{T}$ in $\boldsymbol{x}_S$** (see Box 2).

Comput Mech (2016) 58:549–585
DOI 10.1007/s00466-016-1306-y

The macro-scale strain increment $d\boldsymbol{\varepsilon}_S$, in $\mathcal{S}$, is the data input of the constitutive model in Box 2. This generalized strain increment is defined in equation (6) and can be represented by the triad $\{d\boldsymbol{\varepsilon}_{\bar{u}}, d\boldsymbol{\varepsilon}_{\beta}, d\boldsymbol{\beta}\}$. Note that the displacement jump $\boldsymbol{\beta}$ (a vector term) is used in Box 2 instead of the singular tensor term described in the right hand side of equation (6).

The first block of equations (32)–(38) in Box 2, defines the micro-scale kinematics in Ω_μ. Following the same notation as above, the micro-scale strain increment is identified as $d\boldsymbol{\varepsilon}_\mu$. Also, the micro-scale strain increment fluctuation is denoted $d\tilde{\boldsymbol{\varepsilon}}_\mu$, and is defined in equation (34).

The insertion operator $\mathcal{I}_S(\cdot)$, defined in equation (33), distributes the macro-scale strain increments given by $\{d\boldsymbol{\varepsilon}_{\bar{u}}, d\boldsymbol{\varepsilon}_{\beta}, d\boldsymbol{\beta}\}$ into Ω_μ. Similar to the previous case, the increment of the macro-scale regular strain, $d\boldsymbol{\varepsilon}_{\bar{u}} + \theta d\boldsymbol{\varepsilon}_{\boldsymbol{\beta}}$, is uniformly distributed in Ω_μ. However, $\theta d\boldsymbol{\beta}$ is only distributed into the micro-scale strain localization domain $\mathcal{S}_\mu^L$ corresponding to the n_{op} opening cohesive surfaces. Therefore, in this case, the generalized strain descriptors $\{d\boldsymbol{\varepsilon}_{\bar{u}}, d\boldsymbol{\varepsilon}_{\beta}, d\boldsymbol{\beta}\}$, are not uniformly distributed into Ω_μ. Again, in this case, the parameter θ scales all the terms where the macro-scale displacement jump $\boldsymbol{\beta}$ is present.

In correspondence with (14) and (15), equation (34) defines the micro-scale strain increment fluctuation. Note, in this expression, that all the micro-scale nucleated cohesive surfaces contribute to $d\tilde{\boldsymbol{\varepsilon}}_\mu$.

The Kinematical admissibility requirement (16), hypothesis H1, is imposed through two equations:

$$\int_{\Omega_\mu} d\boldsymbol{\varepsilon}_\mu \, d\Omega_\mu = \int_{\Omega_\mu} \mathcal{I}_S(d\boldsymbol{\varepsilon}_{\bar{u}}, d\boldsymbol{\varepsilon}_{\beta}, \boldsymbol{0}) \, d\Omega_\mu \tag{29}$$

$$\int_{\mathcal{S}_\mu^L} d\boldsymbol{\varepsilon}_\mu \, d\Omega_\mu = \int_{\mathcal{S}_\mu^L} \mathcal{I}_S(\boldsymbol{0}, \boldsymbol{0}, d\boldsymbol{\beta}) \, d\mathcal{S}_\mu \tag{30}$$

see [44] for additional details. The kinematically admissible displacement fluctuation space $\tilde{\mathscr{U}}_\mu^S$ in Ω_μ, and the corresponding virtual action space $\mathscr{V}_\mu^S$, are defined in expressions (35) and (37), respectively. The first constraint in (35) defines fields $d\tilde{\boldsymbol{u}}$ satisfying (29) on Ω_μ. The second one defines fields $d\tilde{\boldsymbol{\beta}}$ satisfying (30) on $\mathcal{S}_\mu^L$.

The macro-scale admissible virtual actions are given in expression (36). In this case, note that the macro-scale vector $\hat{\boldsymbol{\beta}}$ can be arbitrarily defined, while the macro-scale regular strain variation $\hat{\boldsymbol{\varepsilon}}_R$ is assumed to be zero.

A specific Principle of Multi-scale Virtual Power (H2), valid for points $\boldsymbol{x}_S$ at the macro-scale, is postulated as follows:

$$\begin{aligned} \boldsymbol{T} \cdot \hat{\boldsymbol{\beta}} = \frac{1}{|\mathcal{S}_\mu^L|} \int_{\Omega_\mu} \boldsymbol{\sigma}_\mu \cdot \hat{\boldsymbol{\varepsilon}}_\mu(\hat{\boldsymbol{\beta}}, \hat{\tilde{\boldsymbol{u}}}_\mu, \hat{\boldsymbol{\beta}}_\mu^1, ..., \hat{\boldsymbol{\beta}}_\mu^{n_c}) \, d\Omega_\mu \quad , \\ \forall \, \hat{\boldsymbol{\beta}} \quad \text{and} \quad \forall \, (\hat{\tilde{\boldsymbol{u}}}_\mu, \hat{\boldsymbol{\beta}}_\mu^1, ..., \hat{\boldsymbol{\beta}}_\mu^{n_c}) \in \mathscr{V}_\mu^S . \end{aligned} \tag{31}$$

Two equations are naturally derived from the Variational Principle (31):

Comput Mech (2016) 58:549–585
DOI 10.1007/s00466-016-1306-y

ii.1) The first one is obtained by allowing arbitrary variations in $\hat{\boldsymbol{\beta}}$ and holding fixed $(\hat{\tilde{\boldsymbol{u}}}_\mu, \hat{\boldsymbol{\beta}}_\mu^1, ..., \hat{\boldsymbol{\beta}}_\mu^{n_c})$ to zero, resulting the expression (39) in Box 2. This expression provides the homogenization rule for the macro-scale traction $\boldsymbol{T}$ as the averaging of the micro-scale tractions $\boldsymbol{T}_{\mathcal{S}_\mu^{L_j}}$ in all the opening cohesive cracks in Ω_μ. Note the presence of the parameter θ scaling the average traction in $\mathcal{S}_\mu^L$.

ii.2) Alternatively, by imposing arbitrary variation of $(\hat{\tilde{\boldsymbol{u}}}_\mu, \hat{\boldsymbol{\beta}}_\mu^1, ..., \hat{\boldsymbol{\beta}}_\mu^{n_c})$, and holding fixed $\hat{\boldsymbol{\beta}}$ to zero, the micro-scale equilibrium equation (40) is derived. This equation is similar, though with different kinematical constraints, to (28) in Box 1.

Box 2: Multi-scale constitutive Model at Singular points (MMSp)

Given the strain and displacement jump histories $\boldsymbol{\varepsilon}_R^{(t-dt)}$, $\boldsymbol{\beta}^{(t-dt)}$ and $\{d\boldsymbol{\varepsilon}_{\bar{u}}, d\boldsymbol{\varepsilon}_\beta, d\boldsymbol{\beta}\}$; find: $\boldsymbol{T}$ satisfying:

1- ***Kinematics:***

$$d\boldsymbol{\varepsilon}_\mu = \mathcal{I}_S(d\boldsymbol{\varepsilon}_{\bar{u}}, d\boldsymbol{\varepsilon}_\beta, d\boldsymbol{\beta}) + d\tilde{\boldsymbol{\varepsilon}}_\mu \quad , \quad \forall\, \boldsymbol{y} \in \Omega_\mu \tag{32}$$

$$\mathcal{I}_S(d\boldsymbol{\varepsilon}_{\bar{u}}, d\boldsymbol{\varepsilon}_\beta, d\boldsymbol{\beta}) = d\boldsymbol{\varepsilon}_{\bar{u}} + \theta d\boldsymbol{\varepsilon}_{\boldsymbol{\beta}} + \sum_{j=1}^{n_{op}} \delta_{\mathcal{S}_\mu^{L_j}} (\theta d\boldsymbol{\beta} \otimes^s \boldsymbol{n}_\mu^{L_j}) \quad ; \quad \forall\, \boldsymbol{y} \in \Omega_\mu \tag{33}$$

$$d\tilde{\boldsymbol{\varepsilon}}_\mu = \nabla_y^s d\tilde{\tilde{\boldsymbol{u}}}_\mu + \sum_{i=1}^{n_c} \left(\mathscr{M}_\mu^i \nabla_y^s d\tilde{\boldsymbol{\beta}}_\mu^i - \nabla_y \varphi_\mu^i \otimes^s d\tilde{\boldsymbol{\beta}}_\mu^i + \delta_{\mathcal{S}_\mu^i} (d\tilde{\boldsymbol{\beta}}_\mu^i \otimes^s \boldsymbol{n}_\mu^i) \right) \tag{34}$$

Kinematically admissible space of incremental displacement fluctuations, $d\tilde{\boldsymbol{u}}_\mu$***:***

$$\tilde{\mathscr{U}}_\mu^S = \Big\{ (d\tilde{\tilde{\boldsymbol{u}}}_\mu, d\tilde{\boldsymbol{\beta}}_\mu^1, \ldots, d\tilde{\boldsymbol{\beta}}_\mu^{n_c}) \text{ suff. regular, such that:} \\ \int_{\Gamma_\mu} d\tilde{\tilde{\boldsymbol{u}}}_\mu \otimes^s \boldsymbol{\nu}_\mu \, d\Gamma_\mu = \boldsymbol{0} \quad \text{and} \quad \sum_{j=1}^{n_{op}} \int_{\mathcal{S}_\mu^{L_j}} d\tilde{\boldsymbol{\beta}}_\mu^{L_j} \otimes^s \boldsymbol{n}_\mu^{L_j} \, d\mathcal{S}_\mu = \boldsymbol{0} \Big\} \tag{35}$$

Virtual kinematically admissible actions:

Virtual actions at the macro-scale:

$$\hat{\boldsymbol{\beta}} \text{ arbitrary} \quad , \quad \hat{\boldsymbol{\varepsilon}}_R \equiv \boldsymbol{0} \tag{36}$$

Virtual actions at the micro-scale:

$$(\hat{\tilde{\boldsymbol{u}}}_\mu, \hat{\boldsymbol{\beta}}_\mu^1, \ldots, \hat{\boldsymbol{\beta}}_\mu^{n_c}) \in \mathscr{V}_\mu^S \quad , \text{with:} \quad \mathscr{V}_\mu^S = \tilde{\mathscr{U}}_\mu^S \tag{37}$$

$$\hat{\boldsymbol{\varepsilon}}_\mu = \mathcal{I}_S(\boldsymbol{0}, \boldsymbol{0}, \hat{\boldsymbol{\beta}}) + \nabla_y^s \hat{\tilde{\boldsymbol{u}}}_\mu + \sum_{i=1}^{n_c} \left(\mathscr{M}_\mu^i \nabla_y^s \hat{\boldsymbol{\beta}}_\mu^i - \nabla_y^s \varphi_\mu^i \otimes^s \hat{\boldsymbol{\beta}}_\mu^i + \delta_{\mathcal{S}_\mu^i} (\hat{\boldsymbol{\beta}}_\mu^i \otimes^s \boldsymbol{n}_\mu^i) \right) \tag{38}$$

2- ***Consequences derived from the Principle of Multi-scale Virtual Power***

2.a ***Traction Homogenization:***

$$\boldsymbol{T} = \frac{\theta}{|\mathcal{S}_\mu^L|} \left[\sum_{j=1}^{n_{op}} \int_{\mathcal{S}_\mu^{L_j}} \boldsymbol{T}_{\mathcal{S}_\mu^{L_j}} \, d\mathcal{S}_\mu \right] \tag{39}$$

2.b ***Micro-scale Equilibrium problem:***

Given the histories $\boldsymbol{\varepsilon}_R^{(t-dt)}, \boldsymbol{\beta}^{(t-dt)}$ and $\{d\boldsymbol{\varepsilon}_R, d\boldsymbol{\beta}\}$, find $(d\tilde{\tilde{\boldsymbol{u}}}_\mu, d\tilde{\boldsymbol{\beta}}_\mu^1, \ldots, d\tilde{\boldsymbol{\beta}}_\mu^{n_c}) \in \tilde{\mathscr{U}}_\mu^S$ such that:

$$\int_{\Omega_\mu} \boldsymbol{\sigma}_\mu \cdot \hat{\boldsymbol{\varepsilon}}_{\mu R} \, d\Omega_\mu + \sum_{i=1}^{n_c} \int_{\mathcal{S}_\mu^i} \boldsymbol{T}_{\mathcal{S}_\mu^i} \cdot \hat{\boldsymbol{\beta}}_\mu^i \, d\mathcal{S}_\mu = 0 \quad , \quad \forall\, (\hat{\tilde{\boldsymbol{u}}}_\mu, \hat{\boldsymbol{\beta}}_\mu^1, \ldots, \hat{\boldsymbol{\beta}}_\mu^{n_c}) \in \mathscr{V}_\mu^S \tag{40}$$

Comput Mech (2016) 58:549–585
DOI 10.1007/s00466-016-1306-y

Remark: note that both insertion operators $\mathcal{I}(\cdot)$, in equations (20) and (32) define the information which is transferred from the macro to micro-scale, and the way in which the macro-scale kinematics is distributed in Ω_μ.

3 Numerical implementation

The numerical implementation of the multi-scale model, at the macro and micro-scale, are based on finite element methodologies. Although, in both scales it is assumed the existence of cohesive surfaces, and therefore, the modeling of strong discontinuities is required, different procedures are used in each case.

The macro-scale model is based on a new finite element technique with embedded strong discontinuities (EFEM) and automatic crack path detection, recently introduced in the literature by Oliver et al. [46]. In that work, the novel EFEM technique has been utilized for mono-scale failure analysis. Its generalization to multi-scale analysis is here shown. In sub-Section 3.1 a brief summary of the EFEM technique is presented. An important issue for using this element is the crack path detection. Also, following to Oliver et al. [46], this task is performed by using the *"crack path field"* technique, whose description is postponed until sub-Section 3.3.

The present macro-scale model could easily be implemented using alternative finite element techniques dealing with strong discontinuities, such as XFEM, or tracking strategy for evaluating the crack path. It is noted that selection of the most convenient finite element technique, must be primarily decided according with the computational cost involved for evaluating the macro-scale integral terms, in equation (7). Specifically, we are referring to the number of quadrature points required by different techniques.

Alternatively, a standard finite element technique which uses stretched elements with very high aspect ratios, placed between all the edges of the conventional ones and mimicking cohesive surfaces, is adopted for modeling the micro-scale failure. This procedure is briefly summarized in Section 3.2. A discussion about the adequate choice of the RVE boundary conditions and their numerical implementation is also addressed in the same Section.

The finite element technique adopted for modeling the macro-scale is well adapted to handle strong discontinuities intersecting the mesh in arbitrary directions. However, considering that it requires important computational efforts, typically we refer to the evaluation of the crack path tracking algorithm, we prefer an approach computationally less demanding for solving the micro-scale, at the expense of giving up the ability to capture accurately the micro-scale crack path when it intersects the finite element mesh in arbitrary directions.

3.1 Macro-scale finite element model: EFEM technique

The finite element model is briefly described in sub-Section 3.1.1, while the corresponding macro-scale discrete equilibrium equations are presented in sub-Section 3.1.2.

Comput Mech (2016) 58:549–585
DOI 10.1007/s00466-016-1306-y

3.1.1 Finite element with strain enrichment: Constant Strain Mode (CSM) and Discontinuous Displacement Mode (DDM)

Let us consider the mixed bilinear quadrilateral finite element technology with embedded strong discontinuities reported in Oliver et al. [46]. A finite element mesh covers the domain Ω^h of the body (in $\mathbb{R}^2$) and Ω^e denotes the domain of a specific finite element e.

During the structural loading process, the bilinear quadrilateral finite element e can switch between three different formulations, denoted as states: 0, 1 and 2. The sets of elements with identical state define specific body subdomains, such as sketched in Figure 8-b. Elements in states 1 and 2 define the subdomains Ω^h_{CSM} and Ω^h_{DDM}, respectively. A strong discontinuity surface $\mathcal{S}^h$ crosses the domain Ω^h_{DDM}. The remaining subdomain $\Omega^h_0 = \Omega^h \backslash (\Omega^h_{CSM} \cup \Omega^h_{DDM})$ is defined by elements in state 0.

Finite element formulations and the switching from one state to other are defined according with the following rules (see Figure 8-a):

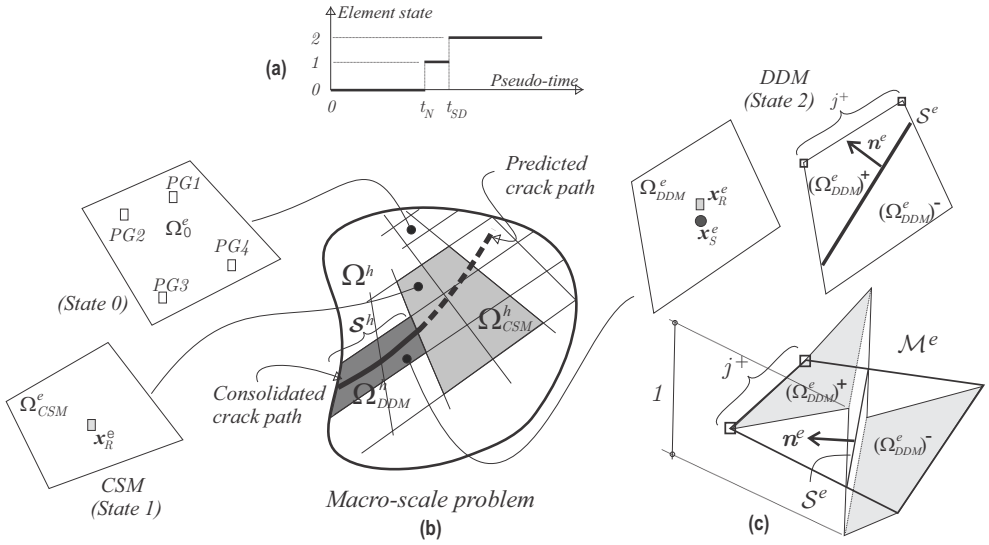

Figure 8: Macro-scale finite element technique. a) Relation between the pseudo-time vs. finite element state for a particular macro-scale finite element; b) finite element states according with subdomain definitions, Ω^h_{CSM} is the domain with finite elements based on CSM (state 1) shown in light gray, Ω^h_{DDM} is the domain with finite elements based on embedded strong discontinuities-DDM (state 2) shown in deep gray, $\Omega^h \backslash (\Omega^h_{CSM} \cup \Omega^h_{DDM})$ is the domain of elements based on an irreducible formulation (state 0) shown in white; c) enrichment function $\mathscr{M}^e$ in elements with DDM.

- Initially, all elements in Ω^h are defined in state 0 ($\Omega^h_0 = \Omega^h$). In this state, elements are modeled as standard quadrilaterals with continuous bilinear displacements. In the standard literature on the finite element method, this formulation is called *irreducible*. A quadrature rule using four Gauss points: $PG1, ..., PG4$, is implemented to evaluate the integrals arising from this irreducible formulation.

- Once the macro-scale bifurcation condition is detected at the pseudo-time: $t = t_N$, in Ω^e, the element originally in state 0 switches to state 1 and becomes part of the subdomain

Comput Mech (2016) 58:549–585
DOI 10.1007/s00466-016-1306-y

Ω^h_{CSM}. The bifurcation condition in element e is tested at the central point $\boldsymbol{x}^e_R$ verifying the singularity of the homogenized acoustic tensor $\boldsymbol{Q}^{hom}$. Then, the bifurcation criterion is satisfied, if:

$$\det(\boldsymbol{Q}^{hom}) = \det(\boldsymbol{n}^e_{bif}\boldsymbol{C}^{hom}\boldsymbol{n}^e_{bif}) = 0 \tag{41}$$

where $\boldsymbol{C}^{hom}$ is the homogenized constitutive tensor given by equation (60) below, and $\boldsymbol{n}^e_{bif}$ is one of the eigenvectors such that (41) is satisfied. The second non-trivial eigenvector is denoted $\boldsymbol{\gamma}$ and represents the initial velocity jump direction across the possible singularity surface whose normal vector is $\boldsymbol{n}^e_{bif}$.

Finite elements in state 1 are also quadrilaterals, but with mixed interpolation of displacements and strains: bilinear interpolation for the incremental displacements and constant interpolation for the incremental strains (Constant Strain Mode-CSM). So, a quadrature rule with only one integration point, the central one $\boldsymbol{x}^e_R$ in Figure 8-a, is enough to evaluate consistently the integrals resulting from the variational problem of this mixed formulation.

Elements in this state are localized in the vicinity of the propagating crack tip (the fracture process zone). The objective pursued by introducing a CSM for strains is to augment the flexibility of the finite elements, and thus, to get a better prediction of the crack path direction in that zone.

- After a subsequent, but small, increment of loading, at the pseudo-time t_{SD} (with $t_{SD} > t_N$), finite elements in state 1 switch to state 2 and become part of subdomain Ω^h_{DDM}. In state 2, a strong discontinuity mode (Discontinuous Displacement Mode-DDM according to Oliver et al. [46]) is embedded into the quadrilateral finite element.

  Previous to switching from states 1 to 2, the position of the surface $\mathcal{S}^e(\boldsymbol{x})$ with normal vector $\boldsymbol{n}^e$ must be determined according to the technique given in sub-Section 3.2 below. Placing the discontinuity surface $\mathcal{S}^e$ in the correct position avoids stress locking in elements where failure is taking place.

Due to the incremental format of the multi-scale model in Section 2, and because of the numerical RVE incremental implementation of sub-Section 3.2 below (more specifically sub-Section 3.2.4), the numerical integration is consistently performed even when the quadrature rule is modified during the element switching from state 0 to 1.

The finite element formulations for states 0 and 1 have been implemented following very standard procedures. Therefore, no further details are given, and the interested reader is referred to the above mentioned reference work. Alternatively, finite elements in state 2 deserve an additional description which is presented in the following.

Implementation of the finite element with DDM (element in state 2)

Let us consider the macro-scale finite element e, with subdomain: $\Omega^e_{DDM} \in \Omega^h_{DDM}$, where an embedded strong discontinuity $\mathcal{S}^e$ with unit normal vector $\boldsymbol{n}^e$ is considered, see Figure 8-c. The discontinuous displacement increment field $d\boldsymbol{u}^e(\boldsymbol{x})$ in the element is given as follows:

$$d\boldsymbol{u}^e(\boldsymbol{x}) = \sum_{p=1}^{4} N^e_p(\boldsymbol{x}) d\bar{\boldsymbol{u}}^{p,e} + \mathscr{M}^e(\boldsymbol{x}) d\boldsymbol{\beta}^e \ , \tag{42}$$

Comput Mech (2016) 58:549–585
DOI 10.1007/s00466-016-1306-y

where N_p^e is the standard shape function of the bilinear quadrilateral element related to the p-th node of element e. The vector of parameters for the continuous displacement increment interpolation and associated with the same p-th node is denoted $d\bar{\boldsymbol{u}}^{p,e}$, while $d\boldsymbol{\beta}^e$ is the vector of element parameters for the displacement jump increment interpolation. There is only one vector $d\boldsymbol{\beta}^e$ ($\boldsymbol{\beta}^e \in \mathbb{R}^2$) per element.

The unit jump function $\mathscr{M}^e(\boldsymbol{x})$ is depicted in Figure 8-c and is defined as follows:

$$\mathscr{M}^e(\boldsymbol{x}) = \mathscr{H}^e(\boldsymbol{x}) - \varphi^e(\boldsymbol{x}) \,, \tag{43}$$

where $\mathscr{H}^e$ is the Heaviside unit function shifted to $\mathcal{S}^e$, and:

$$\varphi^e(\boldsymbol{x}) = \sum_{j=1}^{j^+} N_j^e(\boldsymbol{x}) \,, \tag{44}$$

where the nodes $j = 1, ..., j^+$ belong to $(\Omega_{DDM}^e)^+$, as shown Figure 8-c.

A constant interpolation of regular strain increments per element is assumed. These strain increments are given in matrix notation as follows:

$$d\boldsymbol{\varepsilon}_R^e(\boldsymbol{x}) = \underbrace{\boldsymbol{B}^e(\boldsymbol{x}_R^e)[d\bar{\boldsymbol{u}}^e]}_{d\boldsymbol{\varepsilon}_{\bar{u}}^e} - \underbrace{[\nabla\varphi^e](\boldsymbol{x}_R^e)d\boldsymbol{\beta}^e}_{d\boldsymbol{\varepsilon}_{\beta}^e} \,, \qquad \forall\, \boldsymbol{x} \in \Omega_{DDM}^e \backslash \mathcal{S}^e \tag{45}$$

where, the element vector $[\bar{\boldsymbol{u}}^e]$ collects all the displacements components for the finite element, $\boldsymbol{B}^e$ and $[\nabla\varphi^e]$ are the conventional displacement-strain matrix and the matrix gradient of the function φ^e. Both terms in (45) are evaluated at the central integration point $\boldsymbol{x}_R^e$. Using Voigt notation and a cartesian basis, the strain components are arranged as $\boldsymbol{\varepsilon}_R^e = [\varepsilon_{x_1x_1} \,,\, \varepsilon_{x_2x_2} \,,\, 2\varepsilon_{x_1x_2}]^T$ (with subscripts x_1 and x_2 indicating the cartesian component in $\mathbb{R}^2$). The matrices in (45) are defined as follows:

$$\boldsymbol{B}^e = \begin{bmatrix} \frac{\partial N_1^e}{\partial x_1} & 0 & \dots & \frac{\partial N_4^e}{\partial x_1} & 0 \\ 0 & \frac{\partial N_1^e}{\partial x_2} & \dots & 0 & \frac{\partial N_4^e}{\partial x_2} \\ \frac{\partial N_1^e}{\partial x_2} & \frac{\partial N_1^e}{\partial x_1} & \dots & \frac{\partial N_4^e}{\partial x_2} & \frac{\partial N_4^e}{\partial x_1} \end{bmatrix} \,, \qquad [\nabla\varphi^e] = \begin{bmatrix} \frac{\partial \varphi^e}{\partial x_1} & 0 \\ 0 & \frac{\partial \varphi^e}{\partial x_2} \\ \frac{\partial \varphi^e}{\partial x_2} & \frac{\partial \varphi^e}{\partial x_1} \end{bmatrix} \,, \tag{46}$$

while the element vectors $[d\bar{\boldsymbol{u}}^e]$ and $d\boldsymbol{\beta}^e$ are ordered as:

$$[d\bar{\boldsymbol{u}}^e] = \left[(d\bar{u}_{x_1}^1)\ (d\bar{u}_{x_2}^1)\ \dots\ (d\bar{u}_{x_1}^4)\ (d\bar{u}_{x_2}^4)\right]^T \,, \qquad d\boldsymbol{\beta}^e = \left[d\beta_{x_1}^e\ d\beta_{x_2}^e\right]^T \,, \tag{47}$$

The generalized strain increment in the singular point $\boldsymbol{x}_S^e$, positioned in the center of the element Ω_{DDM}^e and coincident with $\boldsymbol{x}_R^e$, as shown in Figure 8, is characterized through the kinematical descriptors:

$$d\boldsymbol{\varepsilon}_S^e(\boldsymbol{x}_S^e) = \left(d\boldsymbol{\varepsilon}_{\bar{u}}^e, d\boldsymbol{\varepsilon}_{\beta}^e, d\boldsymbol{\beta}^e\right) \,, \tag{48}$$

where the first two descriptors are defined in (45).

In agreement with (42), the virtual actions in the domain of the e-th finite element, can be defined as:

Comput Mech (2016) 58:549–585
DOI 10.1007/s00466-016-1306-y

$$\hat{\boldsymbol{u}}^e = \sum_{p=1}^{4} N_p^e \hat{\boldsymbol{u}}^{p,e} + \mathscr{M}^e \hat{\boldsymbol{\beta}}^e \ , \tag{49}$$

where $\hat{\boldsymbol{u}}^{p,e}$ and $\hat{\boldsymbol{\beta}}^e$ are the vector of parameters for the interpolation of continuous displacement and displacement jump virtual actions, respectively. Also, in agreement with (45), the virtual regular strains are:

$$\hat{\boldsymbol{\varepsilon}}_R^e = \boldsymbol{B}^e(\boldsymbol{x}_R^e)[\hat{\boldsymbol{u}}^e] - [\nabla\varphi^e](\boldsymbol{x}_R^e)[\hat{\boldsymbol{\beta}}^e] \ . \tag{50}$$

Remark: only elements in state 2 ($\Omega_{DDM}^e \subset \Omega_{DDM}^h$) are intersected by cracks. By construction, as shown in Figure 8-c, the support of enrichment functions φ^e and $\mathscr{M}^e$ is Ω_{DDM}^e. Then, elements having states 0 or 1 ($\Omega_0^h \cup \Omega_{CSM}^h$) have the following particularities:

- they are outside the influence zone of any crack;
- in the insertion operator definition, equation (20), $d\boldsymbol{\varepsilon}_{\beta}^e$ is identically zero;
- the insertion operator $\mathcal{I}_R(d\boldsymbol{\varepsilon}_{\bar{u}}^e, \boldsymbol{0})$ distributes uniformly the macro-strain $d\boldsymbol{\varepsilon}_{\bar{u}}^e$ into the RVE domain;
- the MMRp procedure, which evaluates the constitutive relation $\boldsymbol{\sigma}^e$ at all integration points, results identical to the conventional semi-concurrent homogenization techniques reported in the literature (see for example Miehe and Koch [47]), in the sense that the increment of macro-strain $d\boldsymbol{\varepsilon}_{\bar{u}}^e$ is uniformly distributed into the RVE, and the overall stress $\boldsymbol{\sigma}^e$ is the volumetric average in Ω_μ of the micro-scale stresses $\boldsymbol{\sigma}_\mu$.

3.1.2 Discrete equilibrium equations

Introducing the strains and virtual action fields (expressions (45) and (50) for finite elements with DDM), into the variational problem (7) and performing variations of $\hat{\boldsymbol{u}}^e$, with $\hat{\boldsymbol{\beta}}^e$ fixed to zero, we obtain the discrete version of the equilibrium equation as follows:

$$\underbrace{\Lambda_{e=1}^{nelem} \int_{\Omega^e \setminus \mathcal{S}^e} (\boldsymbol{B}^e)^T \boldsymbol{\sigma}^e \, d\Omega^e}_{\boldsymbol{F}^{int}} - \boldsymbol{F}^{ext} = \boldsymbol{0} \ , \tag{51}$$

where $\boldsymbol{F}^{int}$ and $\boldsymbol{F}^{ext}$ are the global vectors of internal and external forces, respectively, Λ is the finite element assembling operator and $\boldsymbol{\sigma}^e$ is the macro-scale element stress arranged using Voigt notation. The vector $\boldsymbol{F}^{int}$ in equation (51) is evaluated with an adequate integration rule, according with the state of each finite element. Elements in state 0 require a standard integrations rule with four Gauss points, while elements in states 1 and 2 require only one integration point (the integration point is placed at the central position of the element and is represented by $\boldsymbol{x}_R^e$ in Figure 8).

Alternatively, the traction equilibrium equation across $\mathcal{S}^e$, with $\mathcal{S}^e \subset \Omega_{DDM}^e \subset \Omega_{DDM}^h$, is not consistently derived from (7). Instead, and following to Oliver et al. [48], a pointwise traction equilibrium equation (SKON formulation according with the denomination coined in the literature) is proposed as follows:

Comput Mech (2016) 58:549–585
DOI 10.1007/s00466-016-1306-y

$$\boldsymbol{T}^e(\boldsymbol{x}_S^e) = \boldsymbol{\sigma}^e(\boldsymbol{x}_R^e)\boldsymbol{n}^e, \qquad \forall e \in \Omega_{DDM}^h \ . \tag{52}$$

The traction vector $\boldsymbol{T}^e$ is evaluated at the integration point $\boldsymbol{x}_S^e$ attached to the cohesive surface, see Figure 9. This vector is obtained by using the MMSp homogenization procedure described in Box 2. On the other hand, the stress $\boldsymbol{\sigma}^e$ is evaluated at the regular point $\boldsymbol{x}_R^e$ using the MMRp homogenization procedure described in Box 1. There is only one equation (52) per each finite element Ω_{DDM}^e in state 2 ($\Omega_{DDM}^e \subset \Omega_{DDM}^h$).

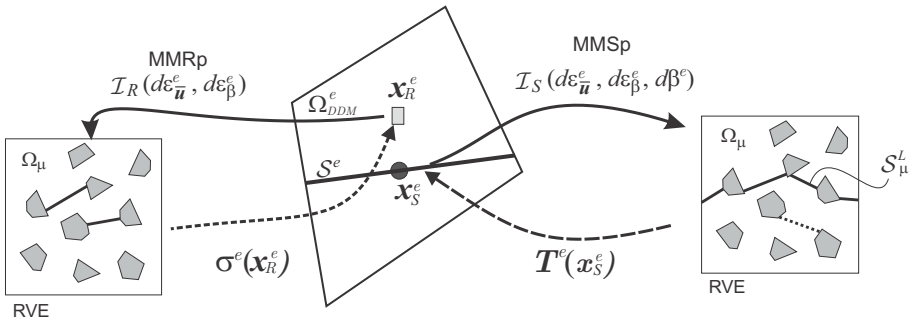

Figure 9: Integration points of a finite element in state 2 with DDM ($\Omega_{DDM}^e \in \Omega_{DDM}^h$). Regular ($\boldsymbol{x}_R^e$) and singular ($\boldsymbol{x}_S^e$) integration points.

Note that according with Figure 9 and the MMSP procedure, the strain localization domain $\mathcal{S}_\mu^L$ in the RVE associated with point $\boldsymbol{x}_S^e$, must be determined before nucleating the cohesive crack $\mathcal{S}^e$ at the macro-scale. In the numerical implementation, the evaluation of this domain is performed just before switching from state 1 to state 2, at pseudo-time: t_{SD}, with $t_{SD} > t_N$, see Figure 8-a. During the interval $[t_N, t_{SD}]$, the localization process at the RVE shows a fast development. So, the failure mechanism and the opening cohesive surfaces at the RVE are more clearly defined at t_{SD} than at t_N, and the domain $\mathcal{S}_\mu^L$ can be thus more accurately determined.

Stiffness matrix of finite elements with DDM

The stiffness matrix of elements with DDM, in state 2, is derived from the equilibrium equations (51) and (52), and can be written as follows:

$$\boldsymbol{K}^e = \begin{bmatrix} \boldsymbol{K}_{\bar{u}\bar{u}}^e & \boldsymbol{K}_{\bar{u}\beta}^e \\ \boldsymbol{K}_{\beta\bar{u}}^e & \boldsymbol{K}_{\beta\beta}^e \end{bmatrix} , \tag{53}$$

where each sub-matrix is:

$$\boldsymbol{K}_{\bar{u}\bar{u}}^e = [\boldsymbol{B}(\boldsymbol{x}_R^e)]^T \frac{\partial \boldsymbol{\sigma}^e(\boldsymbol{x}_R^e)}{\partial \bar{\boldsymbol{u}}^e} |\Omega^e| \ , \tag{54}$$

$$\boldsymbol{K}_{\bar{u}\beta}^e = -[\boldsymbol{B}(\boldsymbol{x}_R^e)]^T \frac{\partial \boldsymbol{\sigma}^e(\boldsymbol{x}_R^e)}{\partial \boldsymbol{\beta}^e} |\Omega^e| \ ; \tag{55}$$

$$\boldsymbol{K}_{\beta\bar{u}}^e = \frac{\partial \boldsymbol{T}^e(\boldsymbol{x}_S^e)}{\partial \bar{\boldsymbol{u}}^e} - \boldsymbol{n}^e \frac{\partial \boldsymbol{\sigma}^e(\boldsymbol{x}_R^e)}{\partial \bar{\boldsymbol{u}}^e} |\Omega^e| \ , \tag{56}$$

$$\boldsymbol{K}_{\beta\beta}^e = \frac{\partial \boldsymbol{T}^e(\boldsymbol{x}_S^e)}{\partial \boldsymbol{\beta}^e} - \boldsymbol{n}^e \frac{\partial \boldsymbol{\sigma}^e(\boldsymbol{x}_R^e)}{\partial \boldsymbol{\beta}^e} |\Omega^e| \ , \tag{57}$$

Comput Mech (2016) 58:549–585
DOI 10.1007/s00466-016-1306-y

where the symbol $|\Omega^e|$ denotes the area of the finite element. The stress derivatives in these expressions are found by considering the stress homogenization equation (27) and the macro-scale regular strain (see equation (45)):

$$\frac{\partial \boldsymbol{\sigma}^e(\boldsymbol{x}_R^e)}{\partial \bar{\boldsymbol{u}}^e} = \boldsymbol{C}^{hom}\boldsymbol{B}^e \,, \tag{58}$$

$$\frac{\partial \boldsymbol{\sigma}^e(\boldsymbol{x}_R^e)}{\partial \boldsymbol{\beta}^e} = -\theta \boldsymbol{C}^{hom}[\nabla \varphi^e] \,, \tag{59}$$

where the homogenized tangent tensor $\boldsymbol{C}^{hom}$ is given by:

$$\boldsymbol{C}^{hom} = \frac{1}{|\Omega_\mu|}\int_{\Omega_\mu}\Big(\boldsymbol{C}_\mu + \boldsymbol{C}_\mu \mathcal{A}(\boldsymbol{y})\Big)d\Omega_\mu; \qquad \mathcal{A}(\boldsymbol{y}) = \frac{\partial \tilde{\boldsymbol{\varepsilon}}_\mu}{\partial \boldsymbol{\varepsilon}_R^e} \,, \qquad \mathcal{A} \in \mathbb{R}^{3\times 3} \,. \tag{60}$$

The operator $\mathcal{A}$ is derived from the implicit functional dependence $\tilde{\boldsymbol{\varepsilon}}_\mu(\boldsymbol{\varepsilon}_R^e)$ established through the micro-scale equilibrium problems (28), see Box 1. Then, the linear operator $\mathcal{A}(\boldsymbol{y})$ can be determined by solving three linear micro-scale equilibrium problems (in $\mathbb{R}^2$). See additional details in [22] and [43].

Finally, the traction homogenization expression (39) in Box 2 related to the MMSp procedure can be derived, resulting in the following expressions:

$$\frac{\partial \boldsymbol{T}^e}{\partial \bar{\boldsymbol{u}}^e} = \frac{\theta}{|\mathcal{S}_\mu^L|}\sum_{j=1}^{n_{op}}\int_{\mathcal{S}_\mu^{L_j}} \boldsymbol{n}_\mu^{L_j}\boldsymbol{C}_\mu \mathcal{D}(\boldsymbol{y})d\mathcal{S}_\mu \,, \tag{61}$$

$$\frac{\partial \boldsymbol{T}^e}{\partial \boldsymbol{\beta}^e} = \frac{\theta}{|\mathcal{S}_\mu^L|}\sum_{j=1}^{n_{op}}\int_{\mathcal{S}_\mu^{L_j}} -\boldsymbol{n}_\mu^{L_j}(\boldsymbol{C}_\mu + \boldsymbol{C}_\mu \mathcal{C}(\boldsymbol{y}))d\mathcal{S}_\mu \,, \tag{62}$$

where we have defined:

$$\mathcal{D}(\boldsymbol{y}) = \frac{\partial \tilde{\boldsymbol{\beta}}_\mu}{\partial \bar{\boldsymbol{u}}^e} \,, \qquad \mathcal{C}(\boldsymbol{y}) = \frac{\partial \tilde{\boldsymbol{\beta}}_\mu}{\partial \boldsymbol{\beta}^e} \,, \tag{63}$$

which can be computed by considering the implicit functional dependence $d\tilde{\boldsymbol{\beta}}_\mu(d\boldsymbol{\varepsilon}_R^e, d\boldsymbol{\beta}^e)$ given by equation (40). Both operators can be found by solving two micro-scale equilibrium problem.

3.2 Micro-scale finite element model

The finite element model at the micro-scale is implemented using a conventional technique without appealing to the explicit inclusion of strong discontinuities. Let us consider the finite element domain of the RVE, denoted Ω_μ^h, with boundary Γ_μ^h and unit normal vector $\boldsymbol{\nu}_\mu^h$, as shown in Figure 10-a. The micro-scale displacement fluctuation increment field, $d\tilde{\boldsymbol{u}}_\mu$, is interpolated in Ω_μ^h as follows:

$$d\tilde{\boldsymbol{u}}_\mu(\boldsymbol{y}) = \sum_{k=1}^{n_{nod}} N_{\mu_k}(\boldsymbol{y})d\tilde{\boldsymbol{q}}_\mu^k \,, \tag{64}$$

Comput Mech (2016) 58:549–585
DOI 10.1007/s00466-016-1306-y

where n_{nod} is the number of nodes of the micro-scale finite element mesh, N_{μ_k} the shape function of the k-th node and $\tilde{\boldsymbol{q}}_\mu^k$ the vector of interpolation parameters, related to the same k-th node, for the displacement fluctuations.

The micro-scale strain increment in the finite element e_μ is:

$$d\boldsymbol{\varepsilon}_\mu^{e_\mu}(\boldsymbol{y}) = \mathcal{I}(d\boldsymbol{\varepsilon}) + \underbrace{\boldsymbol{B}_\mu^{e_\mu}(\boldsymbol{y})[d\tilde{\boldsymbol{q}}_\mu^{e_\mu}]}_{d\tilde{\boldsymbol{\varepsilon}}_\mu^{e_\mu}} , \tag{65}$$

where the insertion operator $\mathcal{I}(\cdot)$ is defined in (21), or (33), depending on the macro-scale point to which the RVE is associated with, and $\boldsymbol{B}_\mu^{e_\mu}$ is the conventional strain-displacement matrix for the micro-scale finite element e_μ. The last term in (65) is the micro-scale strain fluctuation increment $d\tilde{\boldsymbol{\varepsilon}}_\mu^{e_\mu}(\boldsymbol{y})$. The vector $[d\tilde{\boldsymbol{q}}_\mu^{e_\mu}]$ collects all the interpolation parameters of the finite element for the displacements fluctuation increments.

3.2.1 Use of two-dimensional thin band-like domains

Two-dimensional Constant Strain Triangles (CST) elements, displaying high aspect ratios and distributed forming thin band-like domains, are inserted between all the element edges of the original finite element mesh, such as shown in Figure 10.

Each so-formed thin band $\mathcal{B}_\mu^i$ (superscript i identifies the band number) has associated a thickness ℓ_μ^i, a normal vector $\boldsymbol{n}_\mu^i$ and a mean surface $\mathcal{S}_\mu^i$, as shown in Figure 10-b. A band area $|\mathcal{S}_\mu^i|$ (or length per unit of thickness) can be defined, such that $|\mathcal{B}_\mu^i| = |\mathcal{S}_\mu^i|\ell_\mu^i$, where $|\mathcal{B}_\mu^i|$ is the volume of the respective band. The geometrical distribution of CST elements forming the bands are shown in gray in the Figure 10, and their aspect ratio increases with $\ell_\mu^i \to 0$.

The displacement fluctuation and strain fields into the bands are described by equations (64) and (65), respectively.

The objective of introducing these micro-scale bands into the mesh is to capture the failure mechanisms induced by strain localization effects. This procedure can be considered as an alternative technique to more standard cohesive interface finite elements. A distinguishing feature in the present approach is that we can assign continuum constitutive models to the material constituting the thin micro-scale bands.

Strain localization is forced to happens exclusively into the bands $\mathcal{B}_\mu^i$ by defining there a regularized strain softening material response, while elastic, or non-elastic (but with strain hardening), material responses are adopted for all the constituents of the composite (and modeled with the finite elements of the original mesh). Strain localization into the bands initiates after the micro-scale bifurcation condition is reached.

An additional concept associated with the band $\mathcal{B}_\mu^i$ is introduced in the present finite element model. Let us define a local orthogonal coordinate system (η, ζ) aligned with the band, η is placed along the line resulting from the intersection of $\mathcal{S}_\mu^i$ with the plane of analysis, as shown in Figure 10-c. Let us also consider the displacement jump fluctuation increment across the band, $d\tilde{\boldsymbol{\beta}}_\mu^i$, defined along the coordinate η as follows:

$$d\tilde{\boldsymbol{\beta}}_\mu^i(\eta) = d\tilde{\boldsymbol{u}}_\mu(\zeta^+, \eta) - d\tilde{\boldsymbol{u}}_\mu(\zeta^-, \eta) = d\tilde{\boldsymbol{u}}_\mu^+(\eta) - d\tilde{\boldsymbol{u}}_\mu^-(\eta) , \tag{66}$$

Comput Mech (2016) 58:549–585
DOI 10.1007/s00466-016-1306-y

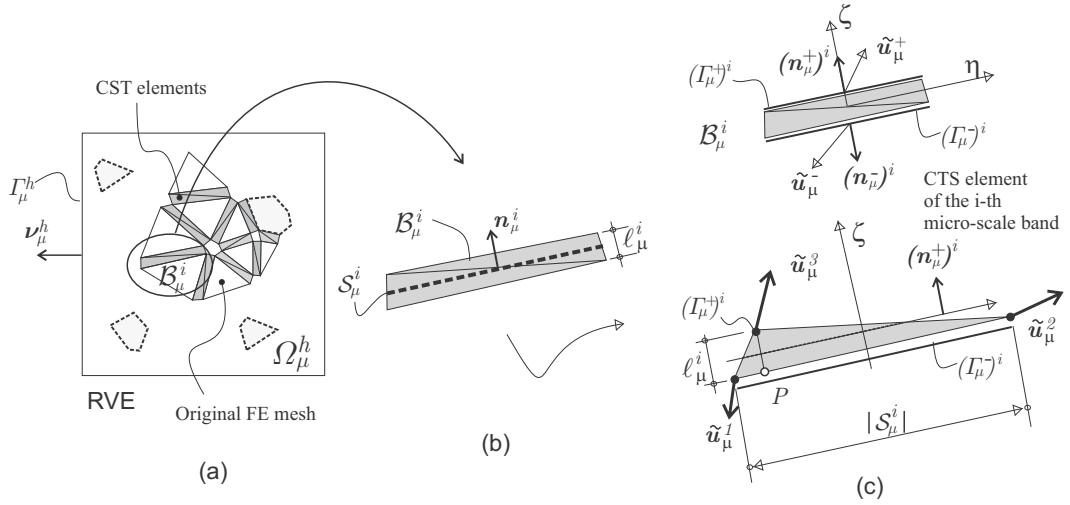

Figure 10: RVE finite element model. (a) CST finite elements arranged like thin bands are inserted at edges of original finite elements (the band-like domains are depicted in grey); (b) band $\mathcal{B}_\mu^i$ and its associated geometrical entities (thickness ℓ_μ^i, normal vector $\boldsymbol{n}_\mu^i$ and mean surface $\mathcal{S}_\mu^i$), (c) local coordinate system (η, ζ) of the i-th band and displacement fluctuation vectors in the CST element nodes.

where the coordinate ζ^+ indicates the position on the boundary $(\Gamma_\mu^+)^i$ and ζ^- the position on the boundary $(\Gamma_\mu^-)^i$. The surfaces $(\Gamma_\mu^+)^i$ and $(\Gamma_\mu^-)^i$ limit the band and are depicted in the same Figure. According with the notation in Figure 10-c, it is noted that the micro-scale strain fluctuation increment in the CST element belonging to $\mathcal{B}_\mu^i$, is given by (see additional details in the work of Manzoli et al. [49]):

$$d\tilde{\boldsymbol{\varepsilon}}_\mu^i = \frac{d\tilde{\boldsymbol{\beta}}_\mu^{i*} \otimes^s \boldsymbol{n}_\mu^{+i}}{\ell_\mu^i} + \mathcal{O}\Big(\frac{\|d\tilde{\boldsymbol{q}}_\mu^2 - d\tilde{\boldsymbol{q}}_\mu^1\|}{|\mathcal{S}_\mu^i|}\Big)\,, \tag{67}$$

where $d\tilde{\boldsymbol{\beta}}_\mu^{i*} = d\tilde{\boldsymbol{q}}_\mu^3 - d\tilde{\boldsymbol{u}}_\mu^P$, being $d\tilde{\boldsymbol{u}}_\mu^P$ the displacement fluctuation increment interpolated at point P. The point P is the orthogonal projection of node 3 onto $(\Gamma_\mu^-)^i$. The second term in (67) can be neglected when $\ell_\mu^i \ll |\mathcal{S}_\mu^i|$ and the band initiates the strain localization process. In this case, the micro-scale strain fluctuation increment $d\tilde{\boldsymbol{\varepsilon}}_\mu^{e_\mu}$ interpolated by (65) into the CST element, naturally approaches to:

$$d\tilde{\boldsymbol{\varepsilon}}_\mu^{e_\mu} \approx \frac{d\tilde{\boldsymbol{\beta}}_\mu^i(0) \otimes^s \boldsymbol{n}_\mu^{+i}}{\ell_\mu^i}. \tag{68}$$

Constitutive relation for the micro-scale bands

The continuum damage model presented in Box 3 describes the material response of the bands $\mathcal{B}_\mu^i$. This constitutive relation has been taken from Oliver [18].

According with equation (69), the internal variables of the model, q_μ and r_μ, as well as their evolution equations (72)–(73), determine the isotropic damage, d_μ, which defines the degradation of the original elastic response ruled by the elastic constitutive tensor $\boldsymbol{C}_\mu$. Initial values of q_μ and r_μ are $q_{\mu 0}$ and $r_{\mu 0}$, respectively. The variable r_μ can be seen as the maximum value of a strain norm reached during the loading history.

Comput Mech (2016) 58:549–585
DOI 10.1007/s00466-016-1306-y

The relation between $\dot{r}_\mu$ and $\dot{q}_\mu$ is given by the softening modulus $H_\mu < 0$, as shown in equation (72). This parameter is characterized from the fracture energy, G_μ^f, of the micro-scale material constituent. The remarkable aspect of the damage model in Box 3 is the regularization of the softening modulus H_μ, with the parameter ℓ_μ, as described by equation (73).

The positive counterpart of the effective micro-scale stress, $(\boldsymbol{\sigma}_\mu^{eff})^+$, is introduced in the damage criterion (70) with the objective of modeling damage evolution only under tensile stress condition.

By adopting this continuum damage model for the micro-scale bands $\mathcal{B}_\mu^i$, ℓ_μ^i small compared to the micro-cell size, and considering that:

a) the softening modulus of the damage constitutive relation is regularized with the length ℓ_μ^i, so that, the total dissipated energy does not depend of this length (this is the reason for introducing the length ℓ_μ^i into the definition of H_μ, as shown in equation (73), Box 3);

b) its elastic response is identical to that of the neighbor bulk material, so that, the overall RVE elastic response is independent of the size ℓ_μ^i;

then, it can be concluded that the complete response of the RVE is independent of the value adopted for ℓ_μ^i.

Identification of the strain localization domain at $t = t_{SD}$.

Once the singularity of the corresponding acoustic tensor has been verified in the CST element $\mathcal{B}_\mu^i$, at time $t_{\mu N}^i$ (with $t_{\mu N}^i < t_N$), the band is identified as a nucleated micro-scale band. Considering that there are n_c nucleated bands, then, the complete domain of nucleated bands is denoted $\mathcal{B}_\mu$, being $\mathcal{B}_\mu = \cup_{i=1}^{n_c} \mathcal{B}_\mu^i$.

An additional ingredient introduced in the RVE finite element model refers to the opening strain localization domain, denoted $\mathcal{B}_\mu^L$, see Figure 11. This domain is defined after the macro-scale bifurcation condition has been detected at $t = t_N$. Typically, $\mathcal{B}_\mu^L$ is evaluated at $t = t_{SD}$ (with $t_{SD} > t_N$ as shown in Figure 8-a). As mentioned in sub-Section 3.1.1, the solution of equation (41) provides two macro-scale eigenvectors, $\boldsymbol{n}_{bif}^e$ and $\boldsymbol{\gamma}$. It is assumed that a nucleated band $\mathcal{B}_\mu^i$ is opening at $t = t_{SD}$ if: $d\tilde{\boldsymbol{\varepsilon}}_\mu \cdot (\boldsymbol{n}_{bif}^e \otimes \boldsymbol{\gamma}) > 0$, where $d\tilde{\boldsymbol{\varepsilon}}_\mu$ is the micro-scale strain fluctuation increment evaluated in the CST element of the band. In this case, the band is identified with the notation $\mathcal{B}_\mu^{L_j}$. Contrarily, a nucleated micro-scale band is closing at $t = t_{SD}$ if that condition is not satisfied.

Then, $\mathcal{B}_\mu^L$ is defined by $\mathcal{B}_\mu^L = \cup_{j=1}^{n_{op}} \mathcal{B}_\mu^{L_j}$, where n_{op} is the number of opening micro-cracks at $t = t_{SD}$. The number of nucleated micro-scale bands which are closing at $t = t_{SD}$ is $n_{cl} = n_c - n_{op}$.

Note that every element in $\mathcal{B}_\mu$ is identified with the superscript "i" ($\mathcal{B}_\mu^i$), while, elements in $\mathcal{B}_\mu^L$ are identified with the superscript "L_j", where the index "j" denotes one specific band of the set. According with this notation, all the geometrical entities associated with the band $\mathcal{B}_\mu^{L_j}$ are denoted with superscript "L_j", e.g.: $\boldsymbol{n}_\mu^{L_j}$, $\mathcal{S}_\mu^{L_j}$, $\ell_\mu^{L_j}$.

Comput Mech (2016) 58:549–585
DOI 10.1007/s00466-016-1306-y

Box 3: Regularized tensile damage model at the micro-scale.

Elastic stress-strain relation

$$\boldsymbol{\sigma}_\mu = \frac{q_\mu}{r_\mu}\,\boldsymbol{C}_\mu\,\boldsymbol{\varepsilon}_\mu = [1-d_\mu(r_\mu)]\,\overbrace{\boldsymbol{C}_\mu\,\boldsymbol{\varepsilon}_\mu}^{\boldsymbol{\sigma}_\mu^{eff}} \quad , \quad d_\mu(r_\mu) = 1 - \frac{q_\mu(r_\mu)}{r_\mu}\ . \tag{69}$$

Damage criterion

$$\mathscr{G}(\boldsymbol{\varepsilon}_\mu, r_\mu) = \sqrt{(\boldsymbol{\sigma}_\mu^{eff})^+ \cdot \boldsymbol{\varepsilon}_\mu} - r_\mu \le 0 \quad , \quad (\boldsymbol{\sigma}_\mu^{eff})^+ = \sum_{i=1}^{3} \left\langle (\sigma_\mu^{eff})_i \right\rangle \boldsymbol{e}_i \otimes \boldsymbol{e}_i\ . \tag{70}$$

Loading/Unloading complementary conditions

$$\dot{r}_\mu \ge 0, \quad \mathscr{G} \le 0, \quad \dot{r}_\mu\,\mathscr{G} = 0 \quad , \quad r_\mu|_{t=0} = r_{\mu 0} = \frac{\sigma_\mu^u}{\sqrt{E_\mu}}\ . \tag{71}$$

Internal variable evolution laws with softening

$$\dot{q}_\mu = H_\mu(r_\mu)\,\dot{r}_\mu, \quad q_\mu \ge 0, \quad q_\mu|_{t=0} = q_{\mu 0} = r_{\mu 0}\ , \tag{72}$$

$$H_\mu(r_\mu) = -\frac{\ell_\mu\, r_{\mu 0}^2}{G_\mu^f}\ \exp\left[-\frac{\ell_\mu\, r_{\mu 0}}{G_\mu^f}(r_\mu - r_{\mu 0})\right]\ . \tag{73}$$

Tangent constitutive tensor

$$\text{if } \dot{r}_\mu = 0, \quad \boldsymbol{C}_\mu^{tan} = (1-d_\mu)\,\boldsymbol{C}_\mu \tag{74}$$

$$\text{if } \dot{r}_\mu > 0, \quad \boldsymbol{C}_\mu^{tan} = (1-d_\mu)\,\boldsymbol{C}_\mu - \left[\frac{q_\mu - H_\mu\, r_\mu}{r_\mu^3}\right] \boldsymbol{\sigma}_\mu^{eff} \otimes (\boldsymbol{\sigma}_\mu^{eff})^+\ . \tag{75}$$

Material parameters

σ_μ^u : Ultimate tensile stress, G_μ^f : Fracture energy.

E_μ, ν_μ : Young's modulus and Poisson ratio, defining the elastic constitutive tensor $\boldsymbol{C}_\mu$

Definitions of variables

r_μ : strain-like internal variable, q_μ : stress-like internal variable,

d_μ : scalar damage variable, H_μ : softening modulus (exponential degradation).

$\boldsymbol{\sigma}_\mu^{eff}$: effective stress, $(\sigma_\mu^{eff})_i$: i-th principal stress of $\boldsymbol{\sigma}_\mu^{eff}$,

$\boldsymbol{e}_i$: i-th eingenvector of $\boldsymbol{\sigma}_\mu^{eff}$, $(\boldsymbol{\sigma}_\mu^{eff})^+$: positive counterpart of effective stress,

$\langle\cdot\rangle$: Macaulay brackets, ℓ_μ : strain localization band thickness,

Comput Mech (2016) 58:549–585
DOI 10.1007/s00466-016-1306-y

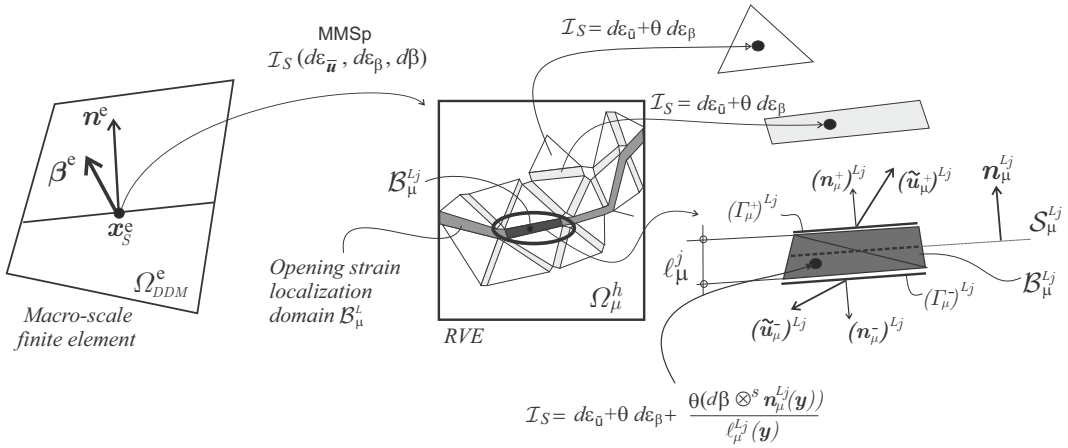

Figure 11: Operator $\mathcal{I}_S$ used in the MMSp homogenization procedure. Macro-scale strain insertion into the micro-scale finite element mesh, Ω_μ^h

Identification of the macro-scale normal vector $\boldsymbol{n}^e$ at $t = t_{SD}$.

The macro-scale normal vector $\boldsymbol{n}^e$ used in the implementation of the EFEM technique is also evaluated at $t = t_{SD}$ as follows:

$$\boldsymbol{n}^e = \frac{\sum_{j=1}^{n_{op}} \int_{\mathcal{S}_\mu^{L_j}} \boldsymbol{n}_\mu^{L_j}\, d\mathcal{S}_\mu}{\| \sum_{j=1}^{n_{op}} \int_{\mathcal{S}_\mu^{L_j}} \boldsymbol{n}_\mu^{L_j}\, d\mathcal{S}_\mu \|} \tag{76}$$

Considering the tortuosity parameter defined in equation (17), it is noted that $\boldsymbol{n}^e$ is the average vector obtained by integrating $\boldsymbol{n}_\mu^{L_j}$ along $\mathcal{S}_\mu^L$ and scaled by θ, such that $\|\boldsymbol{n}^e\| = 1$. The evaluation of $\boldsymbol{n}^e$ with equation (76) requires that all vectors $\boldsymbol{n}_\mu^{L_j}$ are defined following the rule:

$$\boldsymbol{n}_\mu^{L_j} \cdot \boldsymbol{n}_{bif}^e > 0 \quad , \qquad \forall\, j = 1, ..., n_{op}\ , \tag{77}$$

where $\boldsymbol{n}_{bif}^e$ is one of the eigenvector of the macro-scale bifurcation problem in equation (41).

According with our numerical experience, see the results presented in next sub-Section 4.2, the difference observed between the so-determined vector $\boldsymbol{n}^e$ and $\boldsymbol{n}_{bif}^e$ does not exceed a few degrees.

3.2.2 Implementation of the insertion operator

In the forthcoming developments, the superscript "e" indicating macro-scale finite element is removed from the inserted macro-scale kinematical objects.

In expression (65), the operator $\mathcal{I}(\cdot)$ inserts the macro-scale strain according with the procedure defined in Section 2.3. When the MMRp homogenization procedure is used, equation (21) indicates that the operator $\mathcal{I}_R(\cdot)$ inserts uniformly the macro-scale strain increment $d\boldsymbol{\varepsilon}_{\bar{u}} + \theta d\boldsymbol{\varepsilon}_{\boldsymbol{\beta}}$ in all elements of Ω_μ^h. This uniform distribution includes all the CST band elements (even those corresponding to not nucleated bands).

Comput Mech (2016) 58:549–585
DOI 10.1007/s00466-016-1306-y

Alternatively, when the MMSp procedure is used, the operator $\mathcal{I}_S(\cdot)$ also inserts uniformly the macro-scale strain increment, $d\boldsymbol{\varepsilon}_{\bar{u}} + \theta d\boldsymbol{\varepsilon}_{\beta}$, in all elements of Ω_μ^h (including all the CST elements of the n_c bands), but additionally it inserts the term $\theta d\boldsymbol{\beta}$ only in the strain localization domain $\mathcal{B}_\mu^L$. Therefore, the maro-scale strain increment inserted into a CST element in the band $\mathcal{B}_\mu^{L_j}$ is (see Figure 11):

$$\mathcal{I}_S(d\boldsymbol{\varepsilon}_{\bar{u}}, d\boldsymbol{\varepsilon}_{\boldsymbol{\beta}}, d\boldsymbol{\beta}) = d\boldsymbol{\varepsilon}_{\bar{u}} + \theta d\boldsymbol{\varepsilon}_{\boldsymbol{\beta}} + \left[\frac{\theta d\boldsymbol{\beta} \otimes^s \boldsymbol{n}_\mu^{L_j}}{\ell_\mu^{L_j}}\right]. \tag{78}$$

3.2.3 Displacement fluctuations and virtual action fields

According with equation (23) and the displacement field interpolation (64), we define the discrete space of displacement fluctuation increments for the MMRp homogenization procedure, $\tilde{\mathscr{U}}_\mu^{Rh}$ in Ω_μ^h as follows:

$$\tilde{\mathscr{U}}_\mu^{Rh} = \left\{ d\tilde{\boldsymbol{u}}_\mu(\boldsymbol{y}) = \sum_{k=1}^{n_{nod}} N_k(\boldsymbol{y}) d\tilde{\boldsymbol{q}}_\mu^k \ , \quad \text{such that} \int_{\Gamma_\mu^h} d\tilde{\boldsymbol{u}}_\mu \otimes^s \boldsymbol{\nu}_\mu^h d\Gamma_\mu = \boldsymbol{0} \right\}. \tag{79}$$

The kinematical constraint in (79) ensures a zero average value, in Ω_μ^h, of the micro-scale strain fluctuation increment field $d\tilde{\boldsymbol{\varepsilon}}_\mu$, which is defined in every finite element e_μ as:

$$d\tilde{\boldsymbol{\varepsilon}}_\mu^{e_\mu} = \boldsymbol{B}_\mu^{e_\mu}(\boldsymbol{y})[d\tilde{\boldsymbol{q}}_\mu^{e_\mu}] \ . \tag{80}$$

The discrete space of virtual displacement actions $\mathscr{V}_\mu^{Rh}$ is:

$$\mathscr{V}_\mu^{Rh} = \left\{ \hat{\boldsymbol{u}}_\mu(\boldsymbol{y}) = \sum_{k=1}^{n_{nod}} N_k(\boldsymbol{y}) \hat{\boldsymbol{q}}_\mu^k \ , \quad \text{such that} \int_{\Gamma_\mu^h} \hat{\boldsymbol{u}}_\mu \otimes^s \boldsymbol{\nu}_\mu^h d\Gamma_\mu = \boldsymbol{0} \right\}. \tag{81}$$

Alternatively, by considering the MMSp homogenization procedure, and according with (35) and (64), the discrete space of displacement fluctuation increments, $\tilde{\mathscr{U}}_\mu^{Sh}$ in Ω_μ^h, is defined as follows:

$$\tilde{\mathscr{U}}_\mu^{Sh} = \left\{ d\tilde{\boldsymbol{u}}_\mu(\boldsymbol{y}) = \sum_{k=1}^{n_{nod}} N_k(\boldsymbol{y}) d\tilde{\boldsymbol{q}}_\mu^k \ , \quad \text{such that} \int_{\Gamma_\mu^h} d\tilde{\boldsymbol{u}}_\mu \otimes^s \boldsymbol{\nu}_\mu^h d\Gamma_\mu = \boldsymbol{0}; \right.$$
$$\left. \text{and} \quad \sum_{j=1}^{n_{op}} \int_{\mathcal{S}_\mu^{L_j}} d\tilde{\boldsymbol{\beta}}_\mu^{L_j} \otimes^s \boldsymbol{n}_\mu^{L_j} d\mathcal{S}_\mu = \boldsymbol{0} \right\}, \tag{82}$$

where, using the notation previously introduced, it has been considered the displacement jump fluctuation increment $d\tilde{\boldsymbol{\beta}}_\mu^{L_j}$ across the band $\mathcal{B}_\mu^{L_j}$, defined as: $\tilde{\boldsymbol{\beta}}_\mu^{L_j} = (\tilde{\boldsymbol{u}}_\mu^+)^{L_j} - (\tilde{\boldsymbol{u}}_\mu^-)^{L_j}$, with $(\tilde{\boldsymbol{u}}_\mu^+)^{L_j}$ and $(\tilde{\boldsymbol{u}}_\mu^-)^{L_j}$ being the interpolated displacement fluctuations at each side of the band L_j along the coordinate η, such as shown in the insert of Figure 10.

Comput Mech (2016) 58:549–585
DOI 10.1007/s00466-016-1306-y

The discrete space of virtual displacement actions $\mathcal{V}_\mu^{Sh}$ is:

$$\mathcal{V}_\mu^{Sh} = \Big\{ \hat{\boldsymbol{u}}_\mu(\boldsymbol{y}) = \sum_{k=1}^{n_{nod}} N_k(\boldsymbol{y}) \hat{\boldsymbol{q}}_\mu^k \ , \qquad \text{such that} \ \int_{\Gamma_\mu^h} \hat{\boldsymbol{u}}_\mu \otimes^s \boldsymbol{\nu}_\mu^h d\Gamma_\mu = \boldsymbol{0}; \\ \text{and} \quad \sum_{j=1}^{n_{op}} \int_{\mathcal{S}_\mu^{L_j}} \hat{\boldsymbol{\beta}}_\mu^{L_j} \otimes^s \boldsymbol{n}_\mu^{L_j} d\mathcal{S}_\mu = \boldsymbol{0} \quad \Big\} \ , \tag{83}$$

where, in concordance with the comment of the paragraph above, virtual variations of displacement jump across the band $\mathcal{B}_\mu^{L_j}$ are defined as $\hat{\boldsymbol{\beta}}_\mu^i = \hat{\boldsymbol{u}}_\mu^+ - \hat{\boldsymbol{u}}_\mu^-$. The second kinematical constraint defining $\tilde{\mathscr{U}}_\mu^{Sh}$ and $\mathscr{V}_\mu^{Sh}$, extended along $\mathcal{S}_\mu^L$, ensures the satisfaction of identity (30) for the interpolated micro-scale strain fluctuations.

The kinematical constraints defined along Γ_μ^h in (79), and the first one in (82), can be seen as a specific kind of boundary condition defined on the RVE. Following the denomination introduced in our previous work (see [43]), we call it the *Standard Boundary Conditions* (SBC) and is the typical kinematical constraint defined in conventional semi-concurrent multi-scale models. The last constraint imposed along $\mathcal{S}_\mu^L$, in expression (82), is called the *Non-Standard Boundary Conditions* (NSBC). It can be seen as a boundary condition on the domain $\mathcal{B}_\mu^L$. Some remarks about these specific kinematics constraints are given:

Standard Boundary Conditions **(SBC):** The model which strictly satisfies the kinematical constraint in (79) is called *minimum kinematically constrained sub-model*. However, kinematically more constrained sub-models can be defined, such as: Taylor, Linear or Periodic (see Toro et al. [43]).

The kinematical constraints introduced by different sub-models play a very important role for adequately capturing the failure mechanism of the RVE leading to complete degradation of the material. The failure mechanism is defined when the macro-scale bifurcation time t_{SD} is detected. Thus, for $t < t_{SD}$, it should be carefully analyzed if the chosen sub-model inhibits the formation of an expected failure mechanism. The impediment to develop a failure mode due to spurious kinematical boundary conditions could produce a delay of bifurcation detection, and possibly, the identification of an alternative failure mechanism. This issue is strongly associated with the micro-cell size adopted for the analysis. Larger micro-cell sizes tend to decrease the effects introduced by boundary conditions, see the analysis presented in Toro et al. [43]. In general, smaller micro-cell sizes could be utilized for promoting correct failure mechanism if adequate boundary conditions are postulated.

Non-Standard Boundary Conditions **(NSBC):** once the macro-scale crack is activated and $d\boldsymbol{\beta} \neq 0$, the NSBC must be introduced in the model. The NSBC in the present finite element model are defined on the displacement fluctuation increment field $d\tilde{\boldsymbol{u}}_\mu(\boldsymbol{y})$ by constraining the vector $d\tilde{\boldsymbol{\beta}}_\mu^{L_j} = d(\tilde{\boldsymbol{u}}_\mu^+)^{L_j} - d(\tilde{\boldsymbol{u}}_\mu^-)^{L_j}$, along the localization band $\mathcal{B}_\mu^{L_j}$, to satisfy the second constraint in expression (82).

A particular sub-model which trivially satisfies the NSBC consists in defining $d(\tilde{\boldsymbol{u}}_\mu^+)^{L_j} = d(\tilde{\boldsymbol{u}}_\mu^-)^{L_j} \equiv \boldsymbol{0}$ (i.e. fixing to zero the increment of displacement fluctuations of all nodes

Comput Mech (2016) 58:549–585
DOI 10.1007/s00466-016-1306-y

on the boundary of $\mathcal{B}_\mu^L$) and giving $d\tilde{\boldsymbol{\beta}}_\mu^{L_j} \equiv \boldsymbol{0}$. This sub-model is a generalization of the Taylor sub-model extended to the MMSp approach, and is chosen for solving the problems presented in next Section 4. Note that, even fixing to zero the displacement fluctuations increments into the opening localization bands, a non-homogeneous deformation takes place within such bands. In fact, this kind of deformation is induced by the macro-scale strains inserted by the operator $\mathcal{I}_S$.

Numerical treatment of the kinematical constraints

The spaces $\tilde{\mathscr{U}}_\mu^{Rh}$ and $\tilde{\mathscr{U}}_\mu^{Sh}$ (or alternatively, $\tilde{\mathscr{V}}_\mu^{Rh}$ and $\tilde{\mathscr{V}}_\mu^{Sh}$) are implemented by introducing the kinematical constraints (SBC and NSBC) as additional homogeneous linear equations between the degrees of freedoms (d.o.f.'s) of the model.

Let us call $[d\tilde{\boldsymbol{q}}_\mu]$, with $[d\tilde{\boldsymbol{q}}_\mu] \in \mathbb{R}^{2\times n_{nod}}$, the vector collecting the complete set of interpolation parameters for the displacements fluctuation increment field ($[d\tilde{\boldsymbol{q}}_\mu]^T = \left[[d\tilde{\boldsymbol{q}}_\mu^1]^T, ..., [d\tilde{\boldsymbol{q}}_\mu^{n_{nod}}]^T\right]$) of the finite element model. So, $n_{dof} = 2 \times n_{nod}$ identifies the total number of d.o.f.'s of the model.

A direct mathematical treatment allows to write the SBC and NSBC as a system of n_d homogeneous linearly independent equations as follows (see additional details of this point in Toro et al. [43]):

$$\boldsymbol{H}[d\tilde{\boldsymbol{q}}_\mu] = \boldsymbol{0} \qquad ; \qquad \boldsymbol{H} \in \mathbb{R}^{(n_d, n_{dof})} \tag{84}$$

From the previous equation, the vector $[d\tilde{\boldsymbol{q}}_\mu]$ can be partitioned into two vectors of dimension n_d and $n_f = n_{dof} - n_d$:

$$[d\tilde{\boldsymbol{q}}_\mu] = \begin{bmatrix} [d\tilde{\boldsymbol{q}}_\mu]_f \\ [d\tilde{\boldsymbol{q}}_\mu]_d \end{bmatrix} , \qquad [d\tilde{\boldsymbol{q}}_\mu]_f \in \mathbb{R}^{n_f},\ [d\tilde{\boldsymbol{q}}_\mu]_d \in \mathbb{R}^{n_d}, \tag{85}$$

where

$$[d\tilde{\boldsymbol{q}}_\mu]_d = \boldsymbol{L}[d\tilde{\boldsymbol{q}}_\mu]_f \ , \tag{86}$$

being $\boldsymbol{L}$ a matrix of coefficients which are defined according with the kinematical constraints, or discrete space, to be modeled. So, $\boldsymbol{L} = \boldsymbol{L}^{Rh}$ identifies the coefficient matrix imposing the SBC constraint seen in (79), while $\boldsymbol{L} = \boldsymbol{L}^{Sh}$ the matrix imposing both, SBC and NSBC, constraints seen in (82).

The RVE discrete vectors $[d\tilde{\boldsymbol{q}}_\mu]_f$ and $[d\tilde{\boldsymbol{q}}_\mu]_d$ are interpreted as the free and dependent partitions of the total d.o.f.'s, respectively.

Next, we identify the finite dimensional vector spaces corresponding to the vector parameters of displacement fluctuation increments:

$$\tilde{\mathscr{U}}_\mu^{Rq} = \left\{ [d\tilde{\boldsymbol{q}}_\mu] \in \mathbb{R}^{n_{dof}}, \qquad \text{and:} \quad [d\tilde{\boldsymbol{q}}_\mu] = \begin{bmatrix} [d\tilde{\boldsymbol{q}}_\mu]_f \\ \boldsymbol{L}^{Rh}[d\tilde{\boldsymbol{q}}_\mu]_f \end{bmatrix} \right\} , \tag{87}$$

and

$$\tilde{\mathscr{U}}_\mu^{Sq} = \left\{ [d\tilde{\boldsymbol{q}}_\mu] \in \mathbb{R}^{n_{dof}}, \qquad \text{and:} \quad [d\tilde{\boldsymbol{q}}_\mu] = \begin{bmatrix} [d\tilde{\boldsymbol{q}}_\mu]_f \\ \boldsymbol{L}^{Sh}[d\tilde{\boldsymbol{q}}_\mu]_f \end{bmatrix} \right\} . \tag{88}$$

While the finite dimensional vector spaces corresponding to the vector parameters of virtual actions, are defined as $\tilde{\mathscr{V}}_\mu^{Rq} \equiv \tilde{\mathscr{U}}_\mu^{Rq}$ and $\tilde{\mathscr{V}}_\mu^{Sq} \equiv \tilde{\mathscr{U}}_\mu^{Sq}$.

Comput Mech (2016) 58:549–585
DOI 10.1007/s00466-016-1306-y

Note that, fields $d\tilde{\boldsymbol{u}}_\mu$ obtained from the interpolation (64) with vectors $[d\tilde{\boldsymbol{q}}_\mu] \in \tilde{\mathscr{U}}_\mu^{Rq}$, strictly satisfy that $d\tilde{\boldsymbol{u}}_\mu \in \tilde{\mathscr{U}}_\mu^{Rh}$ (or alternatively, fields $d\tilde{\boldsymbol{u}}_\mu$ obtained from the interpolation (64) with vectors $[d\tilde{\boldsymbol{q}}_\mu] \in \tilde{\mathscr{U}}_\mu^{Sq}$ strictly satisfy that $d\tilde{\boldsymbol{u}}_\mu \in \tilde{\mathscr{U}}_\mu^{Sh}$).

3.2.4 Micro-scale variational equilibrium problem.

The variational discrete equilibrium equation in Ω_μ^h for the MMRp homogenization procedure is implemented as follows: find $[\tilde{\boldsymbol{q}}_\mu] \in \tilde{\mathscr{U}}_\mu^{Rq}$, such that:

$$\int_{\Omega_\mu^h} \boldsymbol{\sigma}_\mu \cdot \hat{\boldsymbol{\varepsilon}}_\mu \, d\Omega = [\hat{\boldsymbol{q}}_\mu]^T \boldsymbol{F}_\mu^{int} = 0 \qquad , \qquad \forall\, [\hat{\boldsymbol{q}}_\mu] \in \mathscr{V}_\mu^{Rq} \, , \tag{89}$$

where the vector of internal forces $\boldsymbol{F}_\mu^{int}([\tilde{\boldsymbol{q}}_\mu])$ is:

$$\boldsymbol{F}_\mu^{int} = \Lambda_{e_\mu=1}^{nelem_\mu} \int_{\Omega_\mu^{e_\mu}} \boldsymbol{B}_\mu^{e_\mu T} \boldsymbol{\sigma}_\mu^{e_\mu}(\boldsymbol{\varepsilon}_\mu^{e_\mu}) \, d\Omega_\mu \, . \tag{90}$$

The stresses $\boldsymbol{\sigma}_\mu^{e_\mu}$ in (90) are evaluated with the corresponding constitutive relations associated with every micro-scale components. Also, the micro-strains $\boldsymbol{\varepsilon}_\mu^{e_\mu}$ are determined by (65) and (80). The assembling operation of the internal force vector (90), includes the total number of finite elements $(nelem_\mu)$ in Ω_μ^h, even the CST elements of the micro-scale bands.

Expression (89) is the proposed discrete implementation to approximate the micro-scale equilibrium (28). A numerical strategy for solving (89) has been presented in in Toro et al. [43].

Observe that, by considering in (89), the spaces $\tilde{\mathscr{U}}_\mu^{Sq}$ and $\mathscr{V}_\mu^{Sq}$ instead of $\tilde{\mathscr{U}}_\mu^{Rq}$ and $\mathscr{V}_\mu^{Rq}$, the variational equilibrium equation and the numerical treatment given to the MMSp is obtained.

The connection between the variational equilibrium equation (89), considering the spaces $\tilde{\mathscr{U}}_\mu^{Sq}$ and $\mathscr{V}_\mu^{Sq}$, and the equilibrium equation (40) for a micro-cell with cohesive surfaces is shown through the following identity, which holds for the present micro-scale finite element model using the CST bands:

$$\int_{\Omega_\mu^h} \boldsymbol{\sigma}_\mu \cdot \hat{\boldsymbol{\varepsilon}}_\mu \, d\Omega = \int_{\Omega_\mu^h \backslash \mathcal{B}_\mu} \boldsymbol{\sigma}_\mu \cdot \hat{\boldsymbol{\varepsilon}}_\mu \, d\Omega + \sum_{i=1}^{n_c} \int_{\mathcal{S}_\mu^i} \boldsymbol{T}_\mu^i \cdot \hat{\boldsymbol{\beta}}_\mu^i \, d\mathcal{S} = 0 \qquad , \qquad \forall [\hat{\boldsymbol{q}}_\mu] \in \mathscr{V}_\mu^{Sh} \, , \tag{91}$$

where, the intermediate identity is obtained by partitioning the integral into two disjoint sets $\Omega_\mu^h \backslash \mathcal{B}_\mu$ and $\mathcal{B}_\mu$, and applying the divergence theorem to the integral in $\mathcal{B}_\mu$. Here, it is recalled that we are assuming $\ell_\mu^i \to 0$.

Furthermore, in (91), we define: $\boldsymbol{T}_\mu^i = \boldsymbol{\sigma}_\mu(\boldsymbol{n}_\mu^i)^+$. Therefore, the second term in the middle expression of (91) can be interpreted as the virtual internal power due to cohesive tractions $\boldsymbol{T}_\mu^i$ acting on the band $\mathcal{B}_\mu^i$.

Note that the variational equilibrium equation (91), arising from the present finite element model at the micro-scale, resembles the expression (40) which has been defined for a model with a strong discontinuity kinematics.

If strain localization is not observed in the i-th band (CST elements), the vectors $\boldsymbol{\beta}_\mu^i$, as well as $\tilde{\boldsymbol{\beta}}_\mu^i$, can be assumed very small. Then:

$$\lim_{\ell_\mu^i \to 0} \frac{\boldsymbol{\beta}_\mu^i}{\ell_\mu^i} \approx \mathcal{O}(\boldsymbol{\varepsilon}_{\mu\, \Omega_\mu \backslash \mathcal{B}_\mu}) \, , \tag{92}$$

Comput Mech (2016) 58:549–585
DOI 10.1007/s00466-016-1306-y

where $\boldsymbol{\varepsilon}_{\mu\,\Omega_\mu \setminus \mathcal{B}\mu}$ is the strain in the zone adjacent to the band $\mathcal{B}^i_\mu$. And the internal power in $\mathcal{B}^i_\mu$ is:

$$\int_{\mathcal{B}^i_\mu} \boldsymbol{T}^i_\mu \cdot \boldsymbol{\beta}^i_\mu \, d\mathcal{S} \approx 0 \, . \tag{93}$$

But, once the strain localization process starts in the i-th band, the relative displacement between nodes across the bands can no longer be assumed negligible. The relative displacements across the band take the role of displacement jumps. Then:

$$\lim_{\ell^i_\mu \to 0} \frac{\boldsymbol{\beta}^i_\mu}{\ell^i_\mu} \to \infty \tag{94}$$

and the internal power in $\mathcal{B}^i_\mu$ is no longer necessarily small. So, the kinematics of this finite element behaves like a strong discontinuity kinematics, and the band elements introduce a similar response to conventional cohesive interface elements.

This finite element technique for computational simulation of material failure can be seen as a regularization procedure, using continuum displacement interpolations, of problems displaying strong discontinuities. A similar technique for mono-scale analysis has been reported in Manzoli et al. [49] and Oliver et al. [31].

3.2.5 Degenerated CST elements with strain localization for simulating the RVE failure: pros and cons

The computational technique developed for the micro-scale analysis has two remarkable features:

a) Contrarily to the observed response when classical interface cohesive models are used, CST band elements described with continuous damage model and identical elastic behavior to that of the bulk material do not feature spurious stress oscillations.

b) This approach, coupled with an Impl-Ex constitutive integration scheme (c.f. Oliver et al. [48]), is very robust. The only non-standard step in the numerical implementation of the RVE finite element model is related to the mesh generation, in the sense that, arbitrary meshes ought to receive a pre-treatment to introduce CST band elements between finite element edges of the original mesh.

In turn, it can be noted two serious limitation for modeling micro-structural failure mechanisms with this technique: i) arbitrary crack paths cannot be captured, the crack path must necessarily follow the element edges of the predefined finite element mesh, and ii) severe numerical locking arises for capturing shear bands when non–aligned CST elements are taken. The last deficiency can be alleviated, in part, by using damage-type models to characterize the CST elements.

3.3 A tracking algorithm for determining the macro-scale crack path

The problem of finding the geometrical position of $\mathcal{S}^h \subset \Omega^h$ at the macro-scale, is an important issue of the finite element implementation. As mentioned above, the crack path must be precisely determined before inserting the enriching DDM mode for elements in state 2.

Comput Mech (2016) 58:549–585
DOI 10.1007/s00466-016-1306-y

To achieve this objective, first, it is defined a new field $\varrho(\boldsymbol{x})$ at the macro-scale Ω^h as follows:

$$\varrho(\boldsymbol{x}) = \frac{1}{|\Omega_\mu|} \sum_{i=1}^{n_c} \int_{\mathcal{B}_\mu^i} r_\mu d\mathcal{B}_\mu \ , \tag{95}$$

So, ϱ is the average value in the cell of the micro-scale strain-like internal variable r_μ defined in Box 3. Since r_μ represents a maximum strain measure during the loading history, r_μ becomes very large, proportional to $1/\ell_\mu^i$, in those bands displaying strain localization. However, the integral in (95) is not necessarily zero when $\ell_\mu^i \to 0$ and the area of the band $|\mathcal{B}_\mu^i|$ goes to zero.

At the instant of macro-scale bifurcation, at $t = t_N$, $\varrho(\boldsymbol{x})$ quickly increases, because a sufficient large number of micro-scale bands are subjected to a loading processes. Therefore, the macro-scale regions where the material is reaching the instability condition are characterized by large values of ϱ. Contrarily, ϱ is zero in regions where the inelastic regime has not yet been achieved. We use this property of the field ϱ to predict the geometrical position of the evolving discontinuity surface $\mathcal{S}^h$.

Let us take, at the macro-scale finite element domain Ω^h, the space of functions $\mathscr{L}$ coinciding with the standard bilinear interpolation field $H^1(\Omega^h)$ of the quadrilateral finite element, and the space of piece-wise constant functions, $\mathscr{C}(\Omega^h)$:

$$\mathscr{C}(\Omega^h) := \{\psi(\boldsymbol{x}) \mid \psi(\boldsymbol{x}) = \text{constant} \quad \text{in} \ \ \Omega^e\}. \tag{96}$$

The geometrical position of $\mathcal{S}^h$ intersecting the finite element mesh can be detected by solving two successive problems, described in the following items as steps 1 and 2. Every step involves the projection of discontinuous fields onto $\mathscr{L}$.

Step 1: Find the field $\chi(\boldsymbol{x}) \in \mathscr{L}$, such that:

$$\int_{\Omega^h} \hat{\chi} \ (\chi - \varrho(\boldsymbol{x})) \ d\Omega^h = 0 \qquad ; \qquad \forall \, \hat{\chi} \ \in \ \mathscr{L}. \tag{97}$$

Then, $\chi(\boldsymbol{x})$ can be seen as a smoothing of ϱ. The quadrature rule to integrate (97) follows the similar scheme defined in sub-Section 3.1.

Step 2: Find the directional derivative of χ, $\xi_c^h \in \mathscr{C}$, along the direction given by the vector $\boldsymbol{\omega}$:

$$\xi_c^h(\Omega^e) = \nabla_x \chi(\boldsymbol{x}_S^e) \cdot \boldsymbol{\omega}(\boldsymbol{x}_S^e); \tag{98}$$

where the vector field $\boldsymbol{\omega}$ is a sufficiently smooth extension to Ω^h of the normal vector to $\mathcal{S}^h$ whose location has to be found.

Finally, the so-called crack-path field $\kappa \in \mathscr{L}$ is determined as the smoothing of ξ_c^h. It is evaluated according to the projection:

$$\int_{\Omega} \hat{\kappa} \ (\kappa - \xi_c^h) \ d\Omega^h = 0 \qquad ; \qquad \forall \, \hat{\kappa} \ \in \ \mathscr{L} \tag{99}$$

The manifold $\mathit{\Pi}(\boldsymbol{x})$ is defined as the zero level set of the crack-path field κ:

Comput Mech (2016) 58:549–585
DOI 10.1007/s00466-016-1306-y

$$\boldsymbol{x} \in \mathit{\Pi} \qquad \text{iff} \qquad \kappa(\boldsymbol{x}) = 0. \tag{100}$$

It can be shown (see Oliver et al. [46]) that the discontinuity surface satisfies $\mathcal{S}^h \subset \mathit{\Pi}$. Therefore, the problem of determining $\mathcal{S}^h$ is reduced to finding the set $\mathit{\Pi}$ given by the algebraic procedure defined in equations (97)–(100).

4 Numerical assessment

In a recent contribution by the authors (Toro et al. [44]), some important issues of the present multi-scale model, such as the sensitivity of macro-scale solutions to tortuosity parameter changes, have been analyzed. Here, additional studies are conducted to further validate the implementation of the multi-scale methodology.

With this goal in mind, concrete fracture problems are solved by considering the heterogeneities observed at the meso-scale. Hence, the numerical simulations take into account two-scales of analysis: a) the structural scale and b) the meso-structural scale at lengths of the order of the aggregate sizes. The interaction effects between aggregates and cement-based matrix, mainly those related to fracture, are included in the analysis.

First, in sub-Section 4.1, we describe the meso-structure model developed for concrete. We define the constituents considered at the meso-scale and their possible interactions. In sub-Section 4.2, through a simple uniaxial macroscopic stretching test, we assess the sensitivity of structural results to changes of the mesoscopic cell sizes and finite element sizes modeling the cell. Finally, in sub-Section 4.3 we simulate a double notch beam bending concrete test. Results are computed with several multi-scale models and are validated by comparing with Direct Numerical Simulation (DNS) solutions.

4.1 Concrete failure modeling at the meso-scale

At the meso-scale, three main constituents can be recognized in concrete: cementitious matrix, aggregates and the Interface Transition Zone matrix/aggregate (ITZ). The ITZ constituent plays an important role in the degradation mechanism of this composite. Failure generally initiates at the ITZ, which can be considered as the weakest link for concrete of low to moderate strengths, with the posterior propagation of cracks across the matrix. In this kind of concrete, trans-aggregate fracture is almost never observed. Then, in the present model, the aggregates are assumed to behave like an elastic material with no degradation at all.

The meso-scale model for concrete failure developed in this Section follows very closely the approximations reported in Carol et al. [50] and Unger and Eckardt [51].

Meso-structure model

Representation of an idealized two-dimensional composite model at the meso-scale is performed by selecting, in the plane of analysis, different shape and size particles. The particles represent the aggregates, and they are randomly distributed into a mesoscopic square cell of different sizes, depending on the tests shown in the following. These aggregates are assumed to

Comput Mech (2016) 58:549–585
DOI 10.1007/s00466-016-1306-y

have shapes similar to irregular convex polygons and sizes which are determined from a predefined grading curve (83% of particles with sizes between $3[mm]$ to $4[mm]$, and 17% of particles with sizes between $4[mm]$ to $5[mm]$). The total volume fraction of aggregates results 20.7%. Aggregates distribution is such that they do not intersect the RVE boundaries.

According with the finite element procedure described in Section 3.2, the meso-scale model is designed as shown in Figure 12. CST elements like-bands are inserted along the ITZ, as well as along all the edges of the finite elements, in the original mesh, covering the matrix domain. All these CST elements are characterized with the damage model described in Box 3.

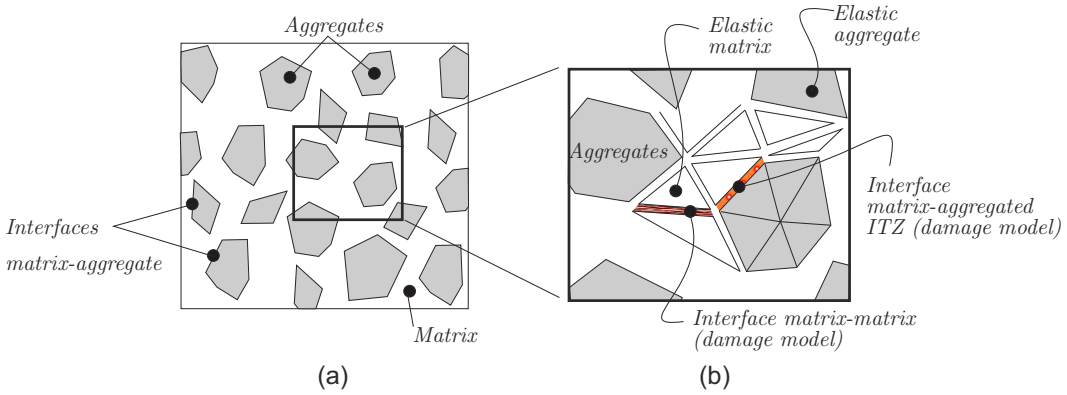

Figure 12: Mesoscopic concrete model.

Material parameters of the meso-scale model

Material parameters of the mesoscopic model are shown in Table 1. These data have been taken from Unger and Eckardt [51] with all the elastic moduli increased 10%. The parameters defined in [51], such as peak stresses and fracture energies of constituents, are considered a very rough estimation for simulating the concrete beam test in sub-Section 4.3 Note that the experimental work (Bocca et al. [52]) taken for validating the numerical results in sub-Section 4.3, reports an overall Young's modulus: $E = 27.[GPa]$ and an overall fracture energy $G^f = 100.[N/m]$.

	$E_\mu\,[GPa]$	ν_μ	$\sigma^u_\mu\,[MPa]$	$G^f_\mu\,[N/m]$
Elastic Matrix	20.4	0.18	—	—
Elastic Aggregate	40.8	0.18	–	–
Interface Matrix-Matrix	20.4	0.18	2.6	140.
ITZ Matrix-Aggregate	20.4	0.18	1.3	70.

Table 1: Material properties for the meso-structure depicted in Figure 12. Parameters defined are: Young's modulus, E_μ, Poisson ratio ν_μ, peak stress σ^u_μ and fracture energy G^f_μ.

Comput Mech (2016) 58:549–585
DOI 10.1007/s00466-016-1306-y

4.2 Multi-scale model sensitivity analysis

By using a simple macro-structural test, linked to complex mesoscopic cell models such as defined in the previous sub-Section, we analyze the sensitivity of the multi-scale model response to changes of cell size and finite element size of the meso-scale model. The analysis is addressed to evaluate the sensitivity of:

i) the crack pattern obtained at the meso-scale level;

ii) the macro-scale crack orientation obtained with equation (76);

iii) the homogenized traction-separation law at the macro-scale.

We study a strip of size $125mm \times 125mm$ and thickness $100mm$ undergoing uniaxial stretching, such as depicted in Figure 13. Two analyses are performed with this strip:

- **Case a)** three specimens stretched in the directions: $\alpha = 0.deg$, $\alpha = 30.deg$ and $\alpha = 45.deg$, respectively, are solved with three mesoscopic cell sizes of $25mm \times 25mm$, $50mm \times 50mm$ and $75mm \times 75mm$. In this case, the size of the finite elements are similar in the three cells;

- **Case b)** the specimen stretched in the directions $\alpha = 0.deg$ of the case a) is solved with the cell size $50mm \times 50mm$, using three meshes which finite element sizes are: coarse (Mesh I), medium (Mesh II) and fine (Mesh III).

In all cases, the kinematical constraints imposed on the micro-cells are: a) minimal kinematical constraints and displacement fluctuation increments of the four cell vertices fixed to zero for the SBC; b) a Taylor sub-model for the NSBC.

Note that, in all specimens, the micro-cells are modeled with their edges parallel to the horizontal and vertical directions. So, the expected failure pattern developed in the three specimens intersects the micro-cell edges at different angles, depending on the stretching direction at the macro-scale. Therefore, from this analysis, it is also possible to assess the effect (if any) induced by the SBC and NSBC for capturing different meso-scale failure patterns.

Case a): sensitivity analysis to changes of cell sizes

The failure modes captured at the meso-scale in the three specimens, using different cell sizes, are analyzed in Figure 13. The Figure displays the deformed configurations of the mesoscopic cells at the end of analysis. In deep red are shown the CST finite elements which are opening at the end of analysis, defining the strain localization domain $\mathcal{B}_{\mu}^{L}$. In light blue are depicted the CST finite elements which have been opening during the pre-critical regime, but are closing at the post-critical regime.

Table 2 presents additional sensitivity results. The angles forming the macro-scale normal vector $\boldsymbol{n}^e$ with the horizontal direction are shown there. These vectors are determined with equation (76). The tortuosity parameters, evaluated with equation (17), are also presented in the last column of the Table. Note the small dispersion of θ obtained in different instances, as well as the close coincidence between the resulting direction of $\boldsymbol{n}^e$ and the stretching direction.

Comput Mech (2016) 58:549–585
DOI 10.1007/s00466-016-1306-y

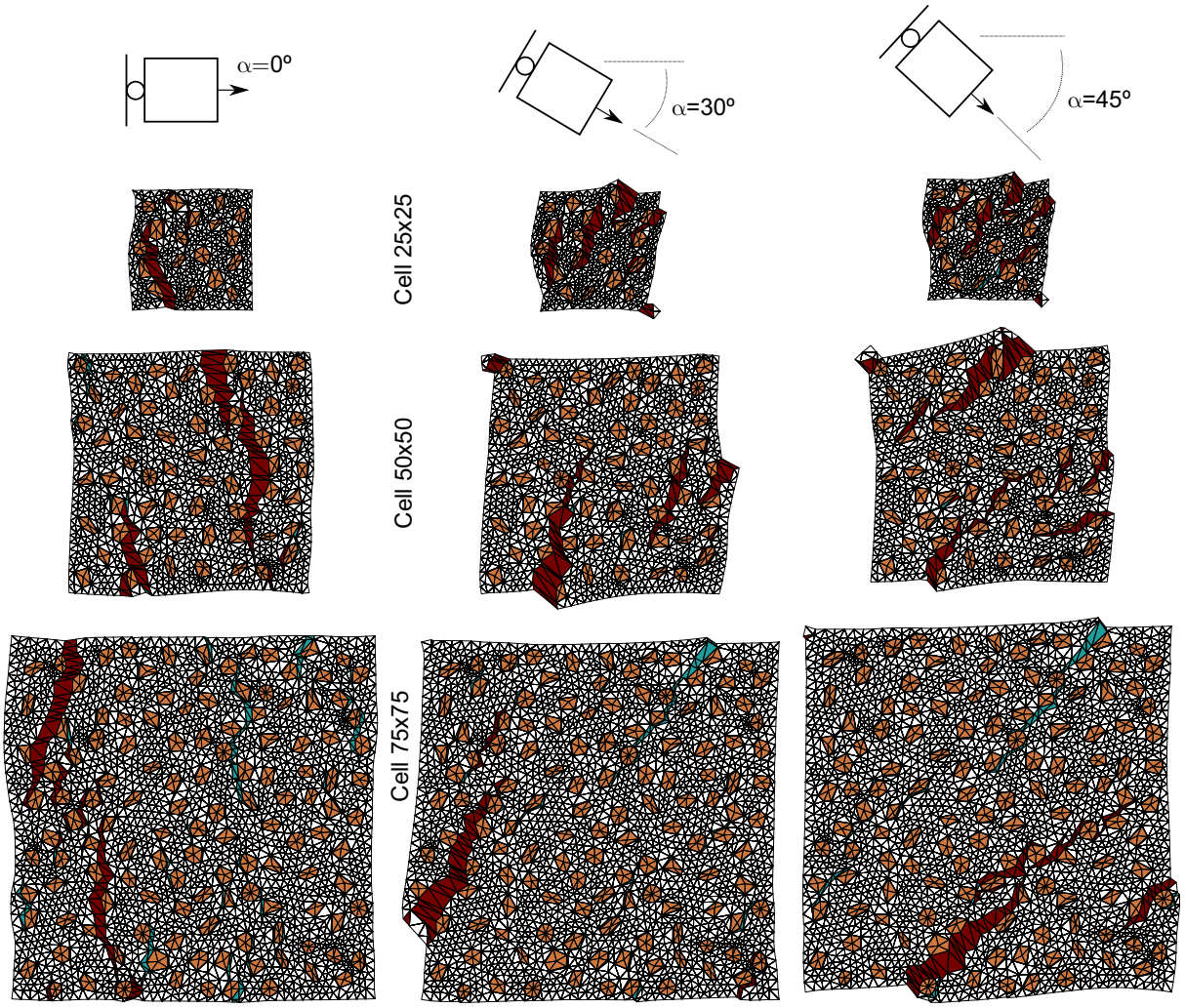

Figure 13: Sensitivity analysis to changes of the cell size. Mesoscopic cell deformed configurations at the end of analysis, depicting the failure modes for different specimens and cell sizes.

Comput Mech (2016) 58:549–585
DOI 10.1007/s00466-016-1306-y

Mesoscopic cell size $[mm]$	Principal stretching angle α $[deg]$	Angle of the macro-scale normal $\boldsymbol{n}^e$ $[deg]$	Tortuosisty parameter θ
25x25	0.	5.	0.89
25x25	30.	26.	0.87
25x25	45.	50.	0.86
50x50	0.	4.	0.88
50x50	30.	33.	0.82
50x50	45.	43.	0.84
75x75	0.	0.	0.86
75x75	30.	26.	0.85
75x75	45.	43.	0.86

Table 2: Macro-scale normal angle ($\boldsymbol{n}^e$) and tortuosity parameter obtained with different mesoscopic cell sizes for the three specimens stretched at angles α.

Figure 14-a displays the structural force (F) vs. macro-scale displacement (δ) curves for all instances. Again, a close coincidence can be observed in all these cases. As expected, a convergence is observed as the cell size is increased. In turn, Figure 14-b presents, for the mesoscopic cell $50mm \times 50mm$ and stretching direction $30.deg$, the normal components of macro-scale stress (σ_{nn}) vs. macro-scale strain (ε_{nn}) during the pre-bifurcation regime ($t \leq t_{SD}$). In the same Figure, it is also plotted the normal components of the macro-scale traction (T_n) vs. the normal components of the macro-scale displacement jump (β_n) during the post-bifurcation regime ($t \geq t_{SD}$). Because both responses, see the two plots in Figure 14-b, are obtained with different homogenization procedures (MMRp and MMSp), it is important to analyze the continuity at $t = t_{SD}$ provided by them. This a very important issue, the continuity of responses with both procedures of the present multi-scale model is a result of introducing the tortuosity parameter θ into the insertion operators $\mathcal{I}$, as well as, in the traction homogenization formula (39), see additional discussion about this aspect of the model in [44].

From this analysis, it can be concluded that the cell with $25mm \times 25mm$ provides results which are considered as objective for the present concrete mesoscopic model. Furthermore, the macro-scale response, including the traction-separation law, the evaluation of the normal vector $\boldsymbol{n}^e$ and the tortuosity parameter θ, are not significantly sensitive to the mesoscopic cell size for cells larger than $25mm \times 25mm$.

Case b): sensitivity analysis to changes of finite element mesh sizes

Using the same structural problem of case a) and a micro-cell of $50mm \times 50mm$ stretched in the horizontal direction, we analyze the results obtained with three different finite element meshes: mesh (I) with 4190 finite elements; mesh (II) with 7964 finite elements and mesh (III) with 17970 finite elements, respectively. Figure 15 displays the crack pattern observed on each mesoscopic cell at the end of analysis, as well as the tortuosity parameters and angle forming the normal vector $\boldsymbol{n}^e$ with the horizontal direction, obtained in each case.

From this analysis, it can be concluded that the evaluations of the tortuosity parameter and the macro-scale normal vector $\boldsymbol{n}^e$ are not sensitive to the finite element mesh size.

Comput Mech (2016) 58:549–585
DOI 10.1007/s00466-016-1306-y

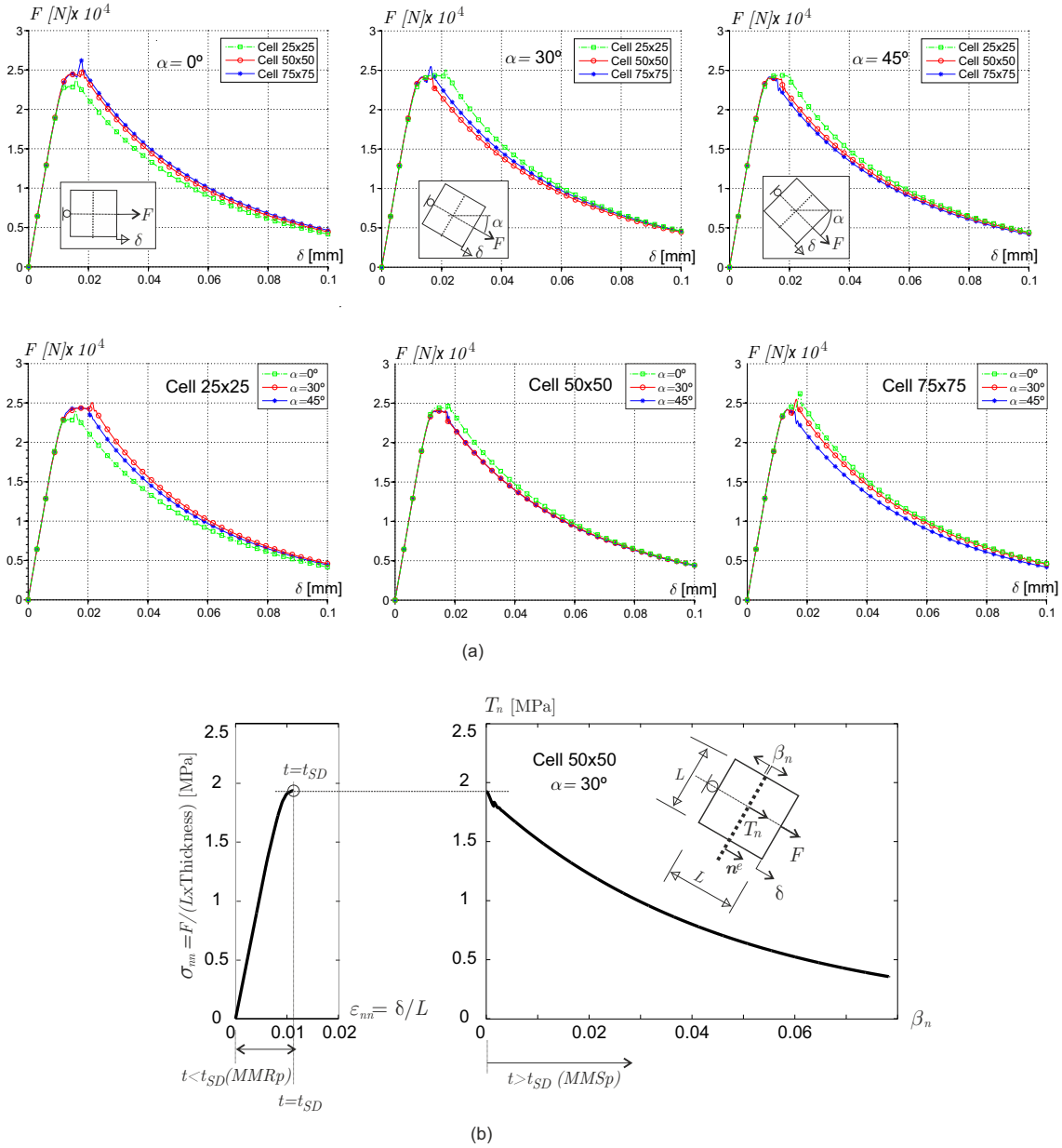

Figure 14: Sensitivity analysis to changes of cell sizes. a) Load vs. displacement plots for the three specimens using three cell sizes of $25mm \times 25mm$, $50mm \times 50mm$ and $75mm \times 75mm$; b) Macro-scale stress- strain curve (σ_{nn} vs. ε_{nn}, subscript indicates components in the direction of $\boldsymbol{n}^e$) during the pre-bifurcation regime and macro-scale traction-separation law (T_n vs. β_n) during the post-bifurcation regime captured with the micro-cell of $50mm \times 50mm$ and stretching direction: $30.deg$.

Comput Mech (2016) 58:549–585
DOI 10.1007/s00466-016-1306-y

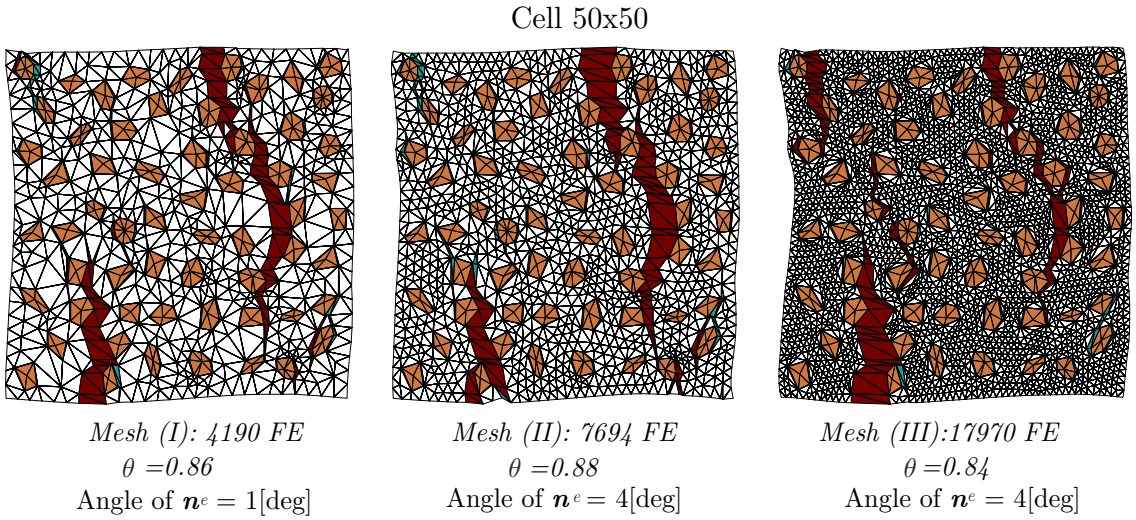

Figure 15: Sensitivity analysis to changes of the finite element mesh size. Solutions obtained with meshes (I), (II) and (III), respectively. (a) Failure mechanism observed at the end of analysis, tortuosity parameters and angle forming the normal vector direction ($\boldsymbol{n}^e$) with the horizontal axis; (b) Structural force (F) vs. macro-scale displacement (δ) curves.

Comput Mech (2016) 58:549–585
DOI 10.1007/s00466-016-1306-y

4.3 Four point shear concrete specimen

The beam with the loading system displayed in Figure 16-a is numerically simulated assuming plane stress condition. In the Figure, units of length are given in millimeters.

This beam corresponds to one of the 27 concrete specimens reported by Bocca et al. [52] ($b = 200.mm$ and $c/b = 0.8$), which, according with these authors, have been conceived to assess the shear effects on the process of cracking.

The beam is here modeled and simulated using the multi-scale formulation developed in this work MS model) and results are compared and validated with solutions obtained using three different Direct Numerical Simulation (DNS) models where the meso-structure is particularly regarded. The reason of solving three DNS problems is to assess the high sensitivity and dispersion of the numerical results that we have detected in this specific problem due to changes of aggregate distribution in the zones close to the notches.

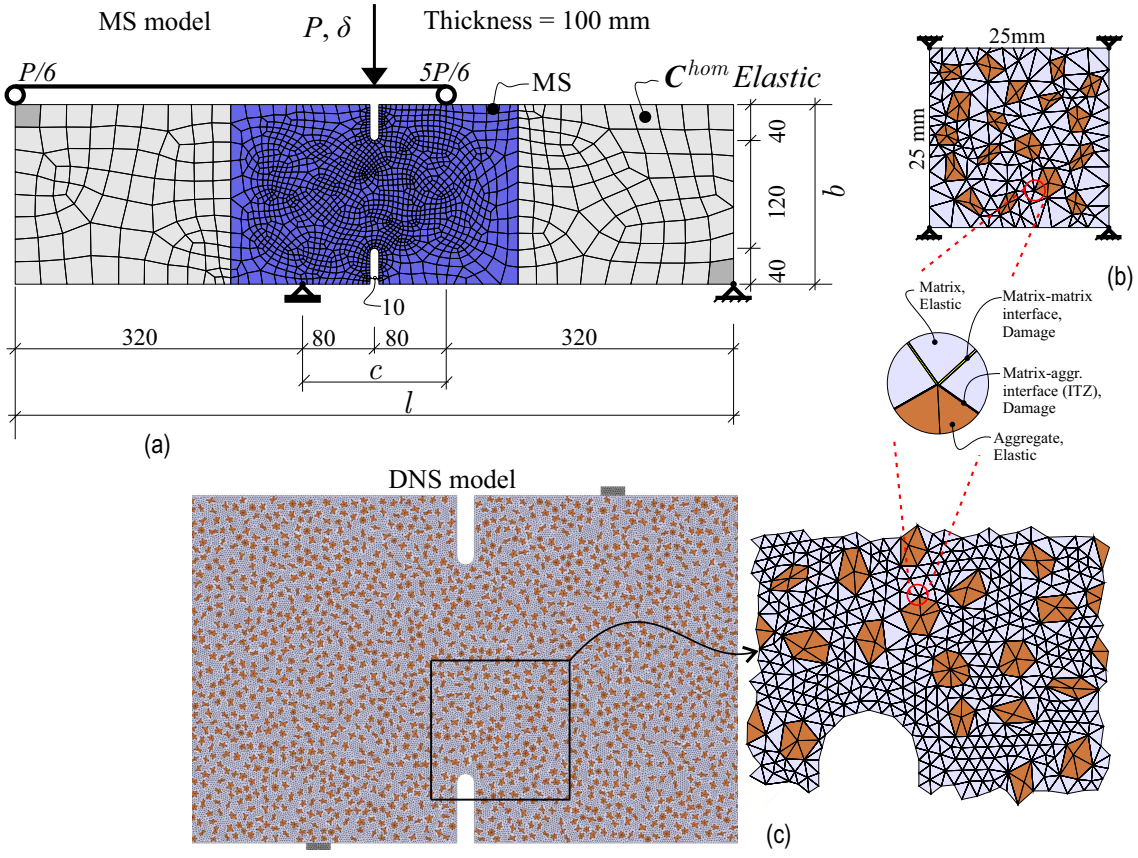

Figure 16: Four point shear concrete specimen. (a) Geometry and multi-scale (MS) finite element model (dimension in millimeters), (b) mesoscopic cell, and (c) one (of the three) DNS model.

MS finite element model

The finite element mesh adopted for the MS model at the macro-scale is shown in Figure

Comput Mech (2016) 58:549–585
DOI 10.1007/s00466-016-1306-y

16-a. A multi-scale approach is only used in the central zone of the beam, depicted in blue. In the remaining part of the specimen, depicted in gray, an elastic mono-scale region is assumed. The homogenized elastic tensor $\boldsymbol{C}^{hom}$ of the multi-scale model is taken for simulating the elastic response of the mono-scale model. The meso-scale is modeled with the cell depicted in Figure 16-b.

First, we compare and discuss the DNS and MS numerical solutions by using, in the last case, a micro-cell subjected to the following type of boundary conditions (BC):

BC's type I:

a) SBC: minimum kinematical constraints with zero displacement fluctuations at the four vertices of the cell;

b) NSBC: Taylor sub-model.

Additionally, in the final part of this Section, we compare the numerical solutions obtained with two MS models, one uses micro-cells subjected to the above described boundary conditions of type I, and the other uses the following boundary conditions:

BC's type II:

a) SBC: periodic;

b) NSBC: Taylor sub-model.

DNS finite element models

Figure 16-c shows one of the three DNS models. The three DNS finite element models are built using an identical approach to that adopted for modeling the meso-scale cell described in sub-Section 4.1. So, a random distribution of aggregates is inserted into the central part of the beam preserving the same volume fraction of aggregates. Finite element meshes with CST elements forming thin bands, which are placed between the edges of elements in the original mesh, are considered. The three meshes of the DNS models use similar size of finite elements.

Discussion of results

a) Morphology of the crack patterns

Figure 17 displays the evolution of the fracture process obtained with one of the three DNS model. In deep red are shown the bands formed by the CST finite elements which are opening at the end of analysis. They define the crack paths leading to the structural collapse. In light red are depicted the bands which have been opening during part of the loading process but finally close. The complete fracture process can be described through two different stages. First, a large number of parallel small cracks (lengths of the order of aggregate sizes) are dispersed. They are approximately orthogonal to the principal stress directions (depicted with a cross). These meso-scale cracks are nucleated in almost the complete central region between both notches of the beam (see Figures 17-a and b). Notably, in a second stage, some of these cracks, close to the

Comput Mech (2016) 58:549–585
DOI 10.1007/s00466-016-1306-y

notches, coalesce in a different direction, forming two competing macro-scale principal cracks. The propagation of one of these macro-scale cracks finally leads to the structural collapse.

As it is observed in the following, the present multi-scale model captures with acceptable accuracy this rather complex fracture process.

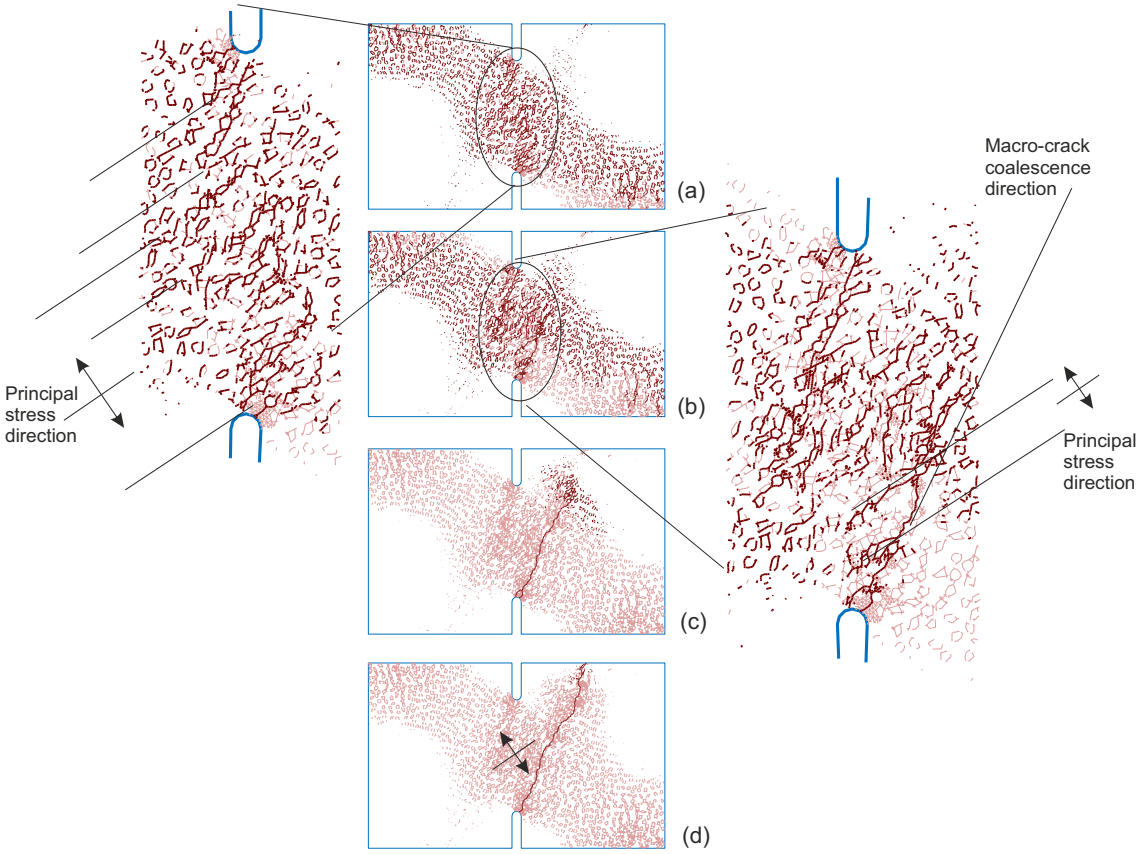

Figure 17: Four point shear concrete specimen. a-d) Sequence of pictures displaying the crack pattern evolution obtained with a DNS model (bands formed by CST finite elements opening at the end of analysis are depicted in dark red, bands which have been opening during part of the loading process but finally close are depicted in light red).

Figure 18-a compares several numerical structural responses in terms of the load P versus vertical displacement δ. The plot of experimental results has been taken from Bocca et al. [52], where it has been very roughly presented. The plot denoted MS corresponds to the numerical multi-scale solution (BC's case I). As can be observed, the structural peak load and the slope after the peak load are well estimated by the model in comparison with the experimental results. However, the structural energy dissipation is larger than that observed in the experimental result. Three DNS solutions provide an additional estimation of the MS result accuracy. The plots of the DNS solutions are rather dispersed, meaning that the numerical structural response is very sensitive with respect to the meso-scale design (aggregate distribution) close to the notches. This numerical behavior could be due to the notch geometry adopted in the present model.

Figure 18-b depicts a sequence of picture (A-K) corresponding to the evolution of the cohesive

Comput Mech (2016) 58:549–585
DOI 10.1007/s00466-016-1306-y

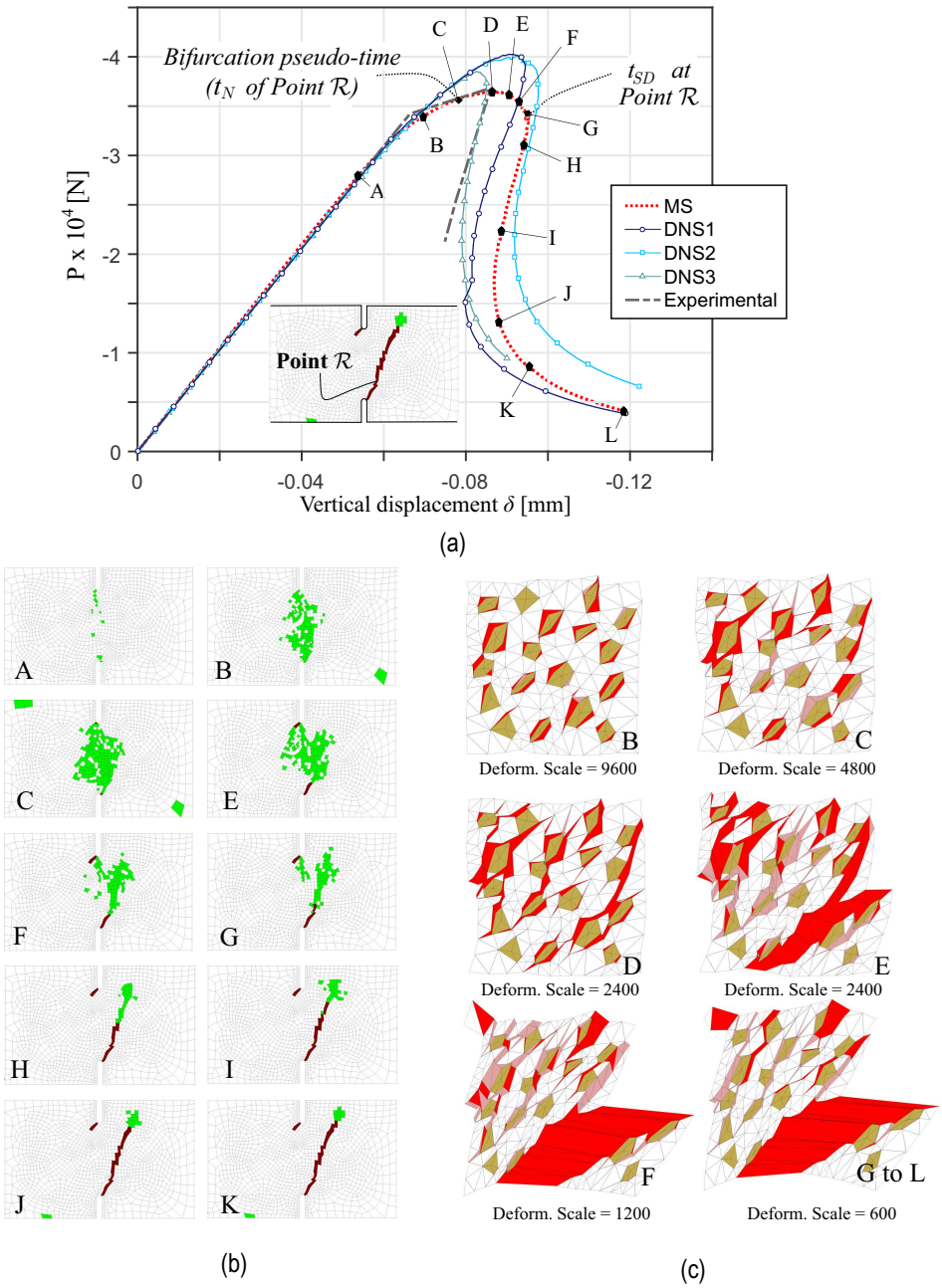

Figure 18: Four point shear concrete specimen. (a) Experimental, MS and DNS structural loads P vs. vertical displacements δ, (b) sequence of pictures showing the evolution of two cracks at the macro-structural scale (finite elements in red belongs to Ω^h_{DDM} (state 2), and elements in green belongs to the domain Ω^h_{CSM} (state 1)), (c) sequence of pictures displaying the deformed configuration of the cells, in terms of displacement fluctuations, of the point $\mathcal{R}$ shown in the inset of Figure 18-a (Elements in dark red correspond to bands which are in loading states, elements in light red correspond to bands which are unloading).

Comput Mech (2016) 58:549–585
DOI 10.1007/s00466-016-1306-y

cracks at the macro-scale. Finite elements in red belongs to Ω^h_{DDM} (state 2), and elements in green belongs to the domain Ω^h_{CSM} (state 1). Every picture A to K is related to the pseudo-time instant shown in the (MS) structural response plot of Figure 18-a. Initially, two cracks start to propagate at both notch roots (picture E). However, the crack initiated in the superior notch stops, while the other continues propagating.

The experimental report ([52]) shows one of the broken specimen, with the ratio: $c/b = 0.4$. From there, it can be observed a curved crack developing from the notch root to the load application point. In the present simulation with $c/b = 0.8$, the crack inducing the structural degradation is almost straight.

Figure 18-c shows a sequence of pictures displaying the failure evolution, in terms of displacement fluctuations, of the mesoscopic cell associated with the macro-scale point $\mathcal{R}$. The macro-scale position of point $\mathcal{R}$ is marked in the inset of Figure 18-a. Every picture in Figure 18-c is associated with the points marked B-L in Figure 18-a, and display the cell fracture process during the loading history. Elements in dark red correspond to bands which are in loading (opening) states, and elements in light red correspond to bands which are unloading (or closing). Observe the picture C corresponding to the instant t_N when the finite element at the macro-scale (in $\mathcal{R}$) switches from state 0 to 1. Also, it is shown the picture G, at the instant when the strong discontinuity (SD) is embedded into the same macro-scale element (switch from state 1 to 2). As it is expected, the sequence of pictures shows that material degradation at point $\mathcal{R}$ starts in the ITZ elements (picture B). A complex pattern of cracks is developed (inset D-F), and at the moment of embedding the strong discontinuity at the macro-scale (point G), the crack pattern at the mesoscopic cell is well defined. After that (G to L), the crack pattern remains fixed until the end of analysis.

Figure 19 shows the macro-scale crack path at the end of the analysis and the normal vectors $\boldsymbol{n}^e$ along the crack. Several deformed configurations of the mesoscopic cells, depicted in terms of the displacement fluctuation field, corresponding to different points along the macro-crack, are also shown.

b) Stress distribution

The color maps in Figure 20-a compares the smoothed fields of principal stresses ($\boldsymbol{\sigma}_I$ and $\boldsymbol{\sigma}_{III}$) obtained with the MS model and one of the DNS models. The load level P at which these stress fields have been evaluated are depicted in the plot P vs. δ in Figure 20-b. At that instant, the main cracks in both models have reached the positions also depicted in the inserts of the same Figure.

In Figure 20-a, the homogenized stresses of the MS model have been taken from the quadrature points placed on the regular domain of the beam. Then, they have been smoothed and finally the principal stresses have been evaluated.

The DNS model stresses have been evaluated as a spatial averaging of the stress tensor into circular domains of radius 12.5 mm centered in points coinciding with the nodal positions of the MS mesh. The principal stresses of these averaged stress tensors are depicted in Figure 20-a.

From the results depicted in that Figure, it can be observed that even when the MS stress distribution is a bit more noisy, it is notably good the close agreement between the stress results provided by both models.

Comput Mech (2016) 58:549–585
DOI 10.1007/s00466-016-1306-y

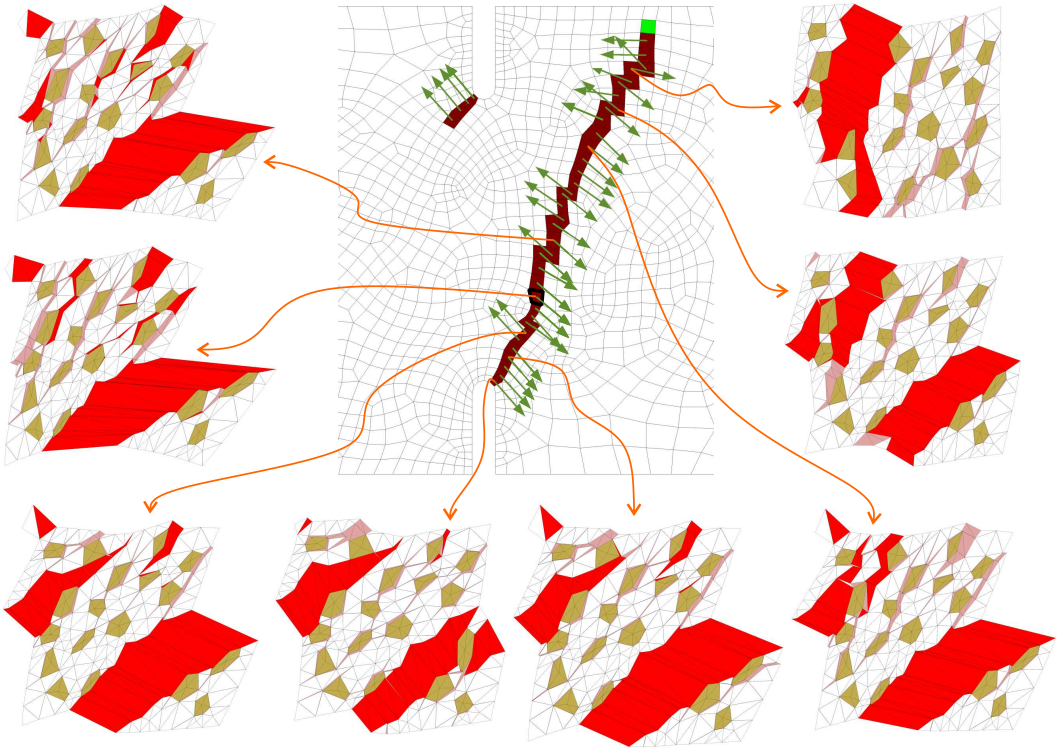

Figure 19: Four point shear concrete specimen:. Crack geometry at the macro-scale and failure mechanisms in several mesoscopic cells associated with different points along the crack. Deformed configurations of the cells are depicted using displacement fluctuations and a scale factor of 600. Distribution of normal vector $\boldsymbol{n}^e$ along the crack path at the macro-scale is shown in green arrows.

Comput Mech (2016) 58:549–585
DOI 10.1007/s00466-016-1306-y

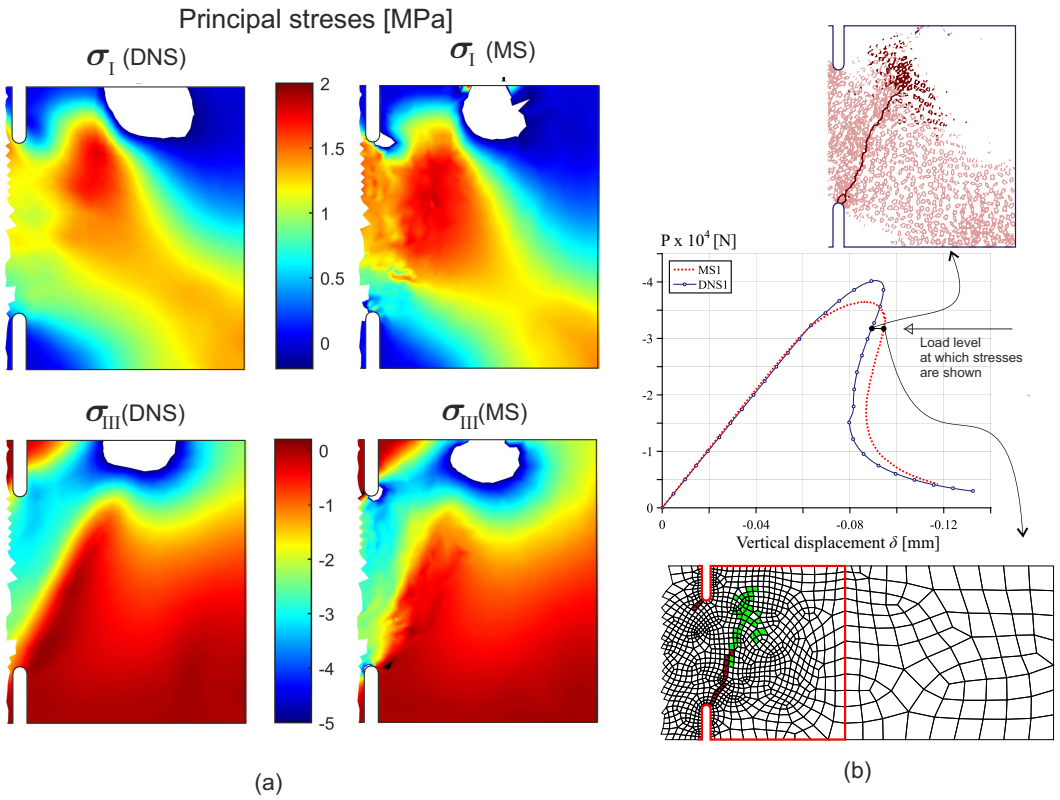

Figure 20: Four point shear concrete specimen. Stress distribution at a given load level. a) Principal stress ($\boldsymbol{\sigma}_I, \boldsymbol{\sigma}_{III}$) fields obtained with DNS and MS models, b) position of the main crack of the DNS and MS solutions at the instant of stress capturing in Figure 20-a. Colored domains in the MS and DNS pictures have the same meaning as in Figures 17 and 18, respectively.

Comput Mech (2016) 58:549–585
DOI 10.1007/s00466-016-1306-y

c) Comparison of results obtained with MS models using different micro-cell boundary conditions

In Figure 21, the solutions obtained with two MS models are depicted. We have compared the solutions provided by the MS model with two different types of SBC constraining the micro-cell kinematics. The type I BC's correspond to SBC with minimal kinematical constrains and the type II BC's correspond to SBC with periodic kinematical constraints.

Figure 21-a plots the structural response of both simulations, while Figure 21-b display the fracture at the end of analysis causing the structural collapse each case.

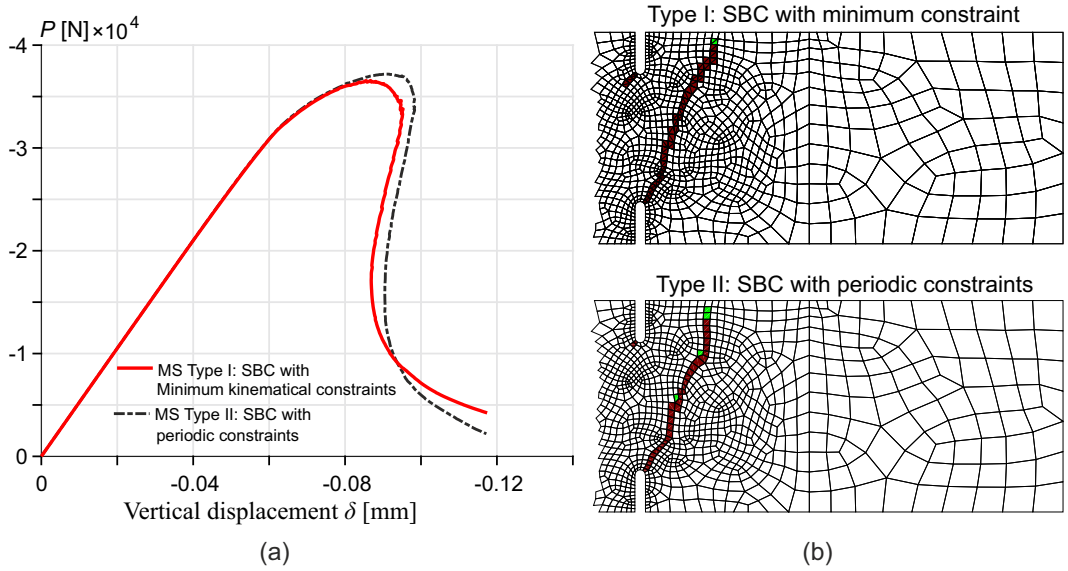

Figure 21: Four point shear concrete specimen: Comparison of results obtained with the MS model using micro-cells with two types of SBC: type I (SBC with minimum kinematical constraints) and type II (SBC with periodic kinematical constraints). a) structural responses, b) cracks at the end of analysis (colored domains have the same meaning as in Figures 18).

5 Conclusion

The main contribution of the paper focuses on describing the numerical implementation of a two-scale semi-concurrent model for fracture analysis. Cohesive surfaces are assumed at both scales of analysis.

The distinctive characteristic of this model is that it assumes two different homogenization procedures to describe the overall material response during the material degradation process:

i) Initially, during the stable response of a point in the macro-scale, a homogenization procedure, denoted MMRp, is adopted. For a macro-scale point which is outside the influence zone of a cohesive crack, the MMRp is identical to conventional homogenization techniques previously reported in the literature. In the context of finite element implementations, the technique has been called FE^2 (Feyel and Chaboche [53]). Contrarily, if the material response is stable but the macro-scale point is inside the influence zone of a cohesive surface,

Comput Mech (2016) 58:549–585
DOI 10.1007/s00466-016-1306-y

the macro-scale strain insertion into the RVE does not follow this kind of approach due to the influence of the tortuosity parameter θ. Thus, in this case, the MMRp can be considered as a novel and non-standard homogenization procedure.

The bifurcation criteria of the macro-scale response, defined in equation (41), is detected using the MMRp homogenization procedure. In that instant, a macro-scale CSM is introduced. The cohesive forces, acting between both interfaces, decrease according with the degradation process of the overall material behavior. Therefore, the traction at the initial instant of the crack insertion is the peak stress of the resulting cohesive interface model introduced at the macro-scale.

Due to the semi-concurrent characteristic of the model, the information is transferred between scales in both directions. As can be noted, the homogenized overall stress is determined with a micro-scale analysis performed in one RVE, whose driving force is the inserted macro-scale strain.

From this observation, we conclude that the peak stress of the resulting cohesive model, which is the overall stress at the bifurcation time projected onto the surface normal vector, is strongly influenced by the macro-scale strains at that instant. This conclusion is of paramount importance when modeling ductile failure.

ii) After detecting the singularity of the acoustic tensor at the macro-scale, a CSM is introduced. The cohesive forces are determined with a homogenization procedure denoted MMSp. In this case, the displacement jump across the interfaces, $\boldsymbol{\beta}$, as well as the strains of the neighbor points, $\boldsymbol{\varepsilon}_R$, are properly inserted into the micro-scale in order to perform the analysis and finally to homogenize the overall traction vector. Again, the evolution of the cohesive force clearly depends on $\boldsymbol{\varepsilon}_R$, and therefore, an identical conclusion to that presented in item (i) is obtained for evaluating the post-critical stage of the material degradation process.

In previous works of the authors, it has been proven that the resulting cohesive constitutive relation, traction vs. displacement jump, is objective with respect to the micro-cell size, with the condition that the micro-cell satisfies the criteria of being a RVE during the stable process of the analysis. This model property has been preserved in the new technique proposed in this paper.

A final but not less important outcome of this work is that according with the sensitivity analysis performed in this study, we conclude that:

1) the definition of the standard boundary conditions (SBC) has not affected the capturing of complex failure patterns intersecting the micro-cell at different angles, such as shown in the strips stretched at different angles (case a of Section 4.2);

2) results, in terms of the homogenized traction-separation law at the macro-scale, have not been sensitive to the finite element size (case b of Section 4.2).

Even when the numerical assessment of the model has been performed by simulating a quasi-brittle fracture problem, it is considered that this methodology can be adapted, with minor changes,

Comput Mech (2016) 58:549–585
DOI 10.1007/s00466-016-1306-y

for modeling ductile failure problems in the context of a large deformation setting. This is matter of current research.

Acknowledgments

S.Toro, P.J. Sánchez and A.E. Huespe acknowledge the financial support from CONICET (grant PIP 2013-2015 631) and from the European Research Council under the European Unions Seventh Framework Programme (FP/2007-2013) / ERC Grant Agreement N. 320815 (ERC Advanced Grant Project Advanced tools for computational design of engineering materials COMP-DES-MAT). P.J. Blanco and R.A. Feijóo acknowledge the financial support provided by the Brazilian agencies CNPq and FAPERJ.

References

[1] D. Dugdale. Yielding of steel sheets containing slits. *J. Mech. Phys. Solids*, 8:100–108, 1960.

[2] G. Barenblatt. The mathematical theory of equilibrium of cracks in brittle fracture. *Adv. Appl. Mech.*, 7:55–129, 1962.

[3] A. Needleman. A continuum model for void nucleation by inclusion debonding. *J. of Appl. Mech.*, 54(3):525–531, 1987.

[4] X.P. Xu and A. Needleman. Numerical simulations of fast crack growth in brittle solids. *J. of the Mech. Phys. Solids*, 42:13971434, 1994.

[5] A. Needleman. Some issues in cohesive surface modeling. *Procedia IUTAM*, 10:221–246, 2014.

[6] M.L. Falk, A. Needlemann, and J.R. Rice. A critical evaluation of dynamic fracture simulation using cohesive surfaces. *J. de Physique IV*, pages Pr–5–43 to Pr–5–50, 2001.

[7] X.P. Xu and A. Needleman. Numerical simulations of dynamic crack growth along an interface. *Int. J. Fracture*, 74(4):289–324, 1995.

[8] A. Pandolfi, P. Krysl, and M. Ortiz. Finite element simulation of ring expansion and fragmentation: the capturing of length and time scales through cohesive models of fracture. *Int. J. Fracture*, 95(1-4):279–297, 1999.

[9] J.W. Hutchinson and A.G. Evans. Mechanics of materials: top-down approaches to fracture. *Acta Materialia*, 48 (1):125–135, 2000.

[10] V. Tvergaard. Crack growth predictions by cohesive zone model for ductile fracture. *J. of the Mech. Phys. Solids*, 49(9):2191–2207, 2001.

[11] T. Siegmund and W. Brocks. A numerical study on the correlation between the work of separation and the dissipation rate in ductile fracture. *Engrg. Fracture Mech.*, 67(2):139–154, 2000.

[12] A.E. Huespe, A. Needleman, J. Oliver, and P.J. Sánchez. A finite thickness band method for ductile fracture analysis. *International Journal of Plasticity*, 25(12):2349–2365, 2009.

[13] A.E. Huespe, A. Needleman, J. Oliver, and P.J. Sánchez. A finite strain, finite band method for modeling ductile fracture. *International Journal of Plasticity*, 28(1):53–69, 2012.

[14] A. Hillerborg, M. Modéer, and P.E. Petersson. Analysis of crack formation and crack growth in concrete by means of fracture mechanics and finite elements. *Cement and concrete research*, 6(6):773–781, 1976.

Comput Mech (2016) 58:549–585
DOI 10.1007/s00466-016-1306-y

[15] Z.P. Bažant. Concrete fracture models: testing and practice. *Engrg. Fracture Mech.*, 69(2):165–205, 2002.

[16] M. Elices, G.V. Guinea, J. Gomez, and J. Planas. The cohesive zone model: advantages, limitations and challenges. *Engrg. Fracture Mech.*, 69(2):137–163, 2002.

[17] J. Oliver, A. E. Huespe, M. D. G. Pulido, and E. Chaves. From continuum mechanics to fracture mechanics: the strong discontinuity approach. *Engineering Fracture Mechanics*, 69:113–136, 2002.

[18] J. Oliver. On the discrete constitutive models induced by strong discontinuity kinematics and continuum constitutive equations. *Int. J. Solids Struct.*, 37:7207–7229, 2000.

[19] V. Tvergaard and J.W. Hutchinson. The relation between crack growth resistance and fracture process parameters in elasto-plastic solids. *J. of the Mech. Phys. Solids*, 40:1377–1397, 1992.

[20] L. Xia and C.F Shih. Ductile crack growth I. A numerical study using computational cells with micrstructurally based length scales. *J. Mech. Phys. Solids*, 43:233–259, 1995.

[21] Franck J Vernerey, Wing Kam Liu, Brian Moran, and Gregory Olson. A micromorphic model for the multiple scale failure of heterogeneous materials. *Journal of the Mechanics and Physics of Solids*, 56(4):1320–1347, 2008.

[22] P.J. Sánchez, P.J. Blanco, A.E. Huespe, and R.A. Feijóo. Failure-oriented multi-scale variational formulation: micro-structures with nucleation and evolution of softening bands. *Comput. Meth. App. Mech. Eng.*, 257:221–247, 2013.

[23] I.M. Gitman, H. Askes, and L.J. Sluys. Representative volume: Existence and size determination. *Engineering Fracture Mechanics*, 74:2518–2534, 2007.

[24] V.P. Nguyen, O. Lloberas-Valls, M. Stroeven, and L.J. Sluys. On the existence of representative volumes for softening quasi-brittle materials - a failure zone averaging scheme. *Comput. Meth. App. Mech. Eng.*, 199:3028–3038, 2010.

[25] T. Belytschko, S. Loehnert, and J.H. Song. Multiscale aggregating discontinuities: A method for circumventing loss of material stability. *Int. J. Numer. Meth. Engng.*, 73:869–894, 2008.

[26] T. Belytschko and J.H. Song. Coarse-graining of multiscale crack propagation. *Int. J. Num. Meth. Eng.*, 81(5): 537–563, 2010.

[27] M.G.D. Geers, V.G. Kouznetsova, and W.A.M. Brekelmans. Multi-scale computational homogenization: Trends and challenges. *Journal of Computational and Applied Mathematics*, 234:2175–2182, 2010.

[28] E Bosco, VG Kouznetsova, and MGD Geers. Multi-scale computational homogenization–localization for propagating discontinuities using x-fem. *ijnme*, 102(3-4):496–527, 2015.

[29] V.P. Nguyen, O.Lloberas-Valls, and L.J. Sluys M. Stroeven. Homogenization-based multiscale crack modelling: from micro diffusive damage to macro cracks. *Comput. Meth. App. Mech. Eng.*, 200:1220–1236, 2010.

[30] C.V. Verhoosel, J.J.C. Remmers, M.A. Gutiérrez, and R. de Borst. Computational homogenization for adhesive and cohesive failure in quasi-brittle solids. *Int. J. Numer. Meth. Engng.*, 83:1155–1179, 2010.

[31] J. Oliver, M. Caicedo, E. Roubin, A.E. Huespe, and J.A. Hernández. Continuum approach to computational multiscale modeling of propagating fracture. *Computer Methods in Applied Mechanics and Engineering*, 294: 384–427, 2015.

[32] M.G. Kulkarni, P.H. Geubelle, and K. Matous. Multi-scale modeling of heterogeneous adhesives: Effect of particle decohesion. *Mechanics of Materials*, 41:573–583, 2009.

[33] P.J. Blanco, P.J. Sánchez, E.A. de Souza Neto, and R.A. Feijóo. Variational foundations and generalized unified theory of RVE-based multiscale models. *Arch. Comput. Methods Eng.*, 2014. DOI 10.1007/s11831-014-9137-5.

Comput Mech (2016) 58:549–585
DOI 10.1007/s00466-016-1306-y

[34] R. Hill. On constitutive macro-variables for heterogeneous solids at finite strain. *Proc. R. Soc. London*, 326, 1972.

[35] J. Mandel. *Plasticit Classique at Viscoplasticit. CISIM Lecture Notes*. Springer-Verlag, 1971.

[36] E.A. de Souza Neto and R.A. Feijóo. Variational foundation on multi-scale constitutive models of solids: small and large strain kinematical formulation. *LNCC Research & Development Report No 16*, 2006.

[37] E.A. de Souza Neto and R.A. Feijóo. On the equivalence between spatial and material volume averaging of stress in large strain multi-scale solid constitutive models. *Mechanics of Materials*, 40:803–811, 2008.

[38] D. Perić, E.A. de Souza Neto, R.A. Feijóo, M. Partovi, and A.J. Carneiro Molina. On micro-to-macro transitions for multi-scale analysis of non-linear heterogeneous materials: unified variational basis and finite element implementation. *Int. J. Num. Meth. Eng.*, 87:149–170, 2011.

[39] E.A. de Souza Neto and R.A. Feijóo. Variational foundations of large strain multiscale solid constitutive models: Kinematical formualtion. In M. Vaz, E.A. de Souza Neto, and P.A. Muoz-Rojas, editors, *Advanced Computational Materials Modeling. From Classical to Multi-Scale Techniques*, pages 341–378, Weinheim, 2011.

[40] P.J. Blanco, P.J. Sánchez, E.A. de Souza Neto, and R.A. Feijóo. The method of multiscale virtual power for the derivation of a second-order mechanical model. *Mechanics of Materials*, 2015, submitted.

[41] P.J. Blanco and S.M. Giusti. Thermomechanical multiscale constitutive modeling: accounting for microstructural thermal effects. *Journal of Elasticity*, 115:27–46, 2014.

[42] E.A. de Souza Neto, P.J. Blanco, P.J. Sánchez, and R.A. Feijóo. An rve-based multiscale theory of solids with micro-scale inertia and body force effects. *Mechanics of Materials*, 80:136–144, 2015.

[43] S. Toro, P.J. Sánchez, A.E. Huespe, S.M. Giusti, P.J. Blanco, and R.A. Feijóo. A two-scale failure model for heterogeneous materials: numerical implementation based on the finite element method. *Int. J. Num. Meth. Eng.*, 97(5):313–351, 2014.

[44] S. Toro, P.J. Sánchez, P.J. Blanco, E.A. de Souza Neto, A.E. Huespe, and R.A. Feijóo. Multiscale formulation for material failure accounting for cohesive cracks at the macro and micro scales. *Int. J. of Plasticity*, 76:75–110, 2016.

[45] J. Simo, J. Oliver, and F. Armero. An analysis of strong discontinuities induced by strain-softening in rate-independent inelastic solids. *Comput. Mech.*, 12:277–296, 1993.

[46] J. Oliver, I.F. Dias, and A.E. Huespe. Crack-path field and strain-injection techniques in computational modeling of propagating material failure. *Comput. Meth. App. Mech. Eng.*, 274:289–348, 2014.

[47] C. Miehe and A. Koch. Computational micro-to-macro transition of discretized microstructures undergoing small strain. *Arch. Appl. Mech.*, 72:300–317, 2002.

[48] J. Oliver, A.E. Huespe, S. Blanco, and D.L. Linero. Stability and robustness issues in numerical modeling of material failure with the strong discontinuity approach. *Comput. Meth. App. Mech. Eng.*, 195(52):7093–7114, 2005.

[49] O.L. Manzoli, A.L. Gamino, E.A. Rodrigues, and G.K.S. Claro. Modeling of interfaces in two-dimensional problems using solid finite elements with high aspect ratio. *Computers & Structures*, 94:70–82, 2012.

[50] I. Carol, C.M. López, and O. Roa. Micromechanical analysis of quasi-brittle materials using fracture-based interface elements. *Int. J. Num. Meth. Eng.*, 52(1-2):193–215, 2001.

[51] J. F Unger and S. Eckardt. Multiscale modeling of concrete. *Archives of Computational Methods in Engineering*, 18(3):341–393, 2011.

Comput Mech (2016) 58:549–585
DOI 10.1007/s00466-016-1306-y

[52] P. Bocca, A. Carpinteri, and S. Valente. Size effects in the mixed mode crack propagation: softening and snap-back analysis. *Engineering Fracture Mechanics*, 35(1):159–170, 1990.

[53] F. Feyel and J.L. Chaboche. FE^2 multiscale approach for modelling the elastoviscoplastic behaviour of long fibre SiC/Ti composite materials. *Comput. Meth. App. Mech. Eng.*, 183:309–330, 2000.